From Single Drop to Spray Cooling: Influence of Lubricant Addition on Heat Transfer

Vom Fachbereich Maschinenbau
der Technischen Universität Darmstadt
zur
Erlangung des Grades eines Doktor-Ingenieurs (Dr.-Ing.)
genehmigte

Dissertation

vorgelegt von

Marija Gajević Joksimović, M.Sc.

aus Belgrad, Serbien

Berichterstatter:	Apl. Prof. Dr. Ilia Roisman
1. Mitberichterstatterin:	Prof. Dr.- Ing. Jeanette Hussong
2. Mitberichterstatter:	Prof. Dr. Marco Marengo
Tag der Einreichung:	20.10.2023
Tag der mündlichen Prüfung:	13.12.2023

Darmstadt 2023

D 17

Gajević Joksimović, Marija:
From Single Drop to Spray Cooling: Influence of Lubricant Addition on Heat Transfer

Darmstadt, Technische Universität Darmstadt
Jahr der Veröffentlichung der Dissertation auf TUprints: 2024
Tag der mündlichen Prüfung: 13.12.2023

Bitte zitieren Sie dieses Dokument als:
URN: urn:nbn:de:tuda-tuprints-266478
URL: http://tuprints.ulb.tu-darmstadt.de/id/eprint/26647

Dieses Dokument wird bereitgestellt von TUprints, E-Publishing-Service der Technischen Universität Darmstadt
http://tuprints.ulb.tu-darmstadt.de
tuprints@ulb.tu-darmstadt.de

Erklärung

Hiermit erkläre ich, dass ich die vorliegende Arbeit, abgesehen von den in ihr ausdrücklich genannten Hilfen, selbständig verfasst habe.

Darmstadt, den 20.10.2023

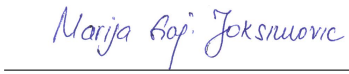

M. Gajević Joksimović

Posvećeno tati i deda Žiki

Abstract

Spray cooling of solid substrates is one of the techniques used in various industrial processes such as forging, quenching or other metallurgical applications, electronics, pharmaceutical industry, medicine or for cooling of high power electrical devices. It is governed by various hydrodynamic and thermodynamic processes such as drop impact, heat conduction in the substrate and convection in the spreading drops, and different boiling regimes. Cooling performance is influenced by a wide range of parameters, including spray characteristics such as drop diameter, drop velocity, and mass flux, followed by surface temperature, surface material, and surface conditions. The problem of modeling spray cooling becomes even more challenging if the liquid is multicomponent. The presence of additives with various physicochemical properties (surfactants, binders, dispersed particles, dissolved phase etc.) can significantly affect the entire spray impact process and impact outcomes, and could lead to the formation of a thin deposited layer on the substrate. The present study attempts to understand the physics behind the process of spraying a multicomponent liquid onto a hot substrate.

A better understanding of the single drop impact is required for a more reliable modeling of spray cooling. In the present work, the single drop impact on a heated substrate is first experimentally investigated for different liquids under various thermodynamic and hydrodynamic conditions. The influence of two different industrial lubricants mixed with water in different ratios (suspensions and solutions) on drop impact and regimes is studied. The effect of additives on the outcome of drop impact, in particular solid graphite particles for the suspensions and organic salts for the solutions, is investigated for different impact conditions. High-speed visualizations of drop impact outcomes are classified according to known heat transfer regimes: nucleate boiling, thermal atomization, and film boiling. The influence of particles is taken into account in a theoretical model for heat transfer in the nucleate boiling regime and particle deposition.

Next, transient spray cooling of a hot thick target by a lubricant solution is experimentally investigated. The temporal evolution of the heat flux and surface temperature of an initially homogeneously heated substrate to temperatures significantly above the liquid saturation point is measured during continuous spray impact. The spray impact is additionally visualized using a high-speed video system, and the instantaneous local heat flux and surface temperature are temporally matched to the visualizations. Observations from the present work show that the presence of even very low concentrations of lubricant dramatically increases the heat flux, especially at high wall temperatures where film boiling is typically observed for spray cooling using distilled water. A significant increase in the drop rebound temperature, often associated with the Leidenfrost point, occurs. Mechanisms leading to the increase in heat flux and the shift of the Leidenfrost point are identified and discussed.

The findings presented in this thesis serve to a more comprehensive understanding of the underlying physics required for the modeling and prediction of spray cooling processes with industrially relevant liquids. The results of this study will provide a basis for modeling the formation of the lubricating layer by cooling sprays, which is necessary for predicting the evolution of its thickness and uniformity.

Kurzfassung

Die Sprühkühlung fester Substrate ist eine der Methoden, die in verschiedenen industriellen Prozessen wie Schmieden, Abschrecken oder anderen metallurgischen Anwendungen, Elektronik, Pharmaindustrie, Medizin oder zur Kühlung von Hochleistungselektronik verwendet werden. Die Sprühkühlung unterliegt verschiedenen hydrodynamischen und thermodynamischen Prozessen wie Tropfenaufprall, Wärmeleitung im Substrat, Konvektion in den sich ausbreitenden Tropfen und unterschiedlichen Siederegimen. Die Kühlleistung wird von einer Vielzahl von Parametern beeinflusst, darunter Sprühcharakteristika wie Tropfendurchmesser, Tropfengeschwindigkeit und Massenstrom, gefolgt von der Oberflächentemperatur, dem Oberflächenmaterial und den -bedingungen. Das Modellierungsproblem der Sprühkühlung wird noch anspruchsvoller, wenn die Flüssigkeit aus mehreren Komponenten besteht. Die Anwesenheit von Additiven mit verschiedenen physikochemischen Eigenschaften (Tensiden, Bindemitteln, dispergierten Partikeln, gelöster Phasen usw.) kann den gesamten Sprühwirkungsprozess und dessen Ergebnisse signifikant beeinflussen und zur Bildung einer dünnen abgelagerten Schicht auf dem Substrat führen. Die vorliegende Studie zielt darauf ab, die physikalischen Zusammenhänge beim Sprühen von industriell verwendeten mehrkomponentigen Flüssigkeiten auf heiße Substrate zu verstehen.

Ein besseres Verständnis des Einzeltropfen-Aufpralls ist erforderlich, um eine zuverlässigere Modellierung der Sprühkühlung zu ermöglichen. In der vorliegenden Arbeit wird der Einzeltropfen-Aufprall auf ein beheiztes Substrat zunächst experimentell für verschiedene Flüssigkeiten unter verschiedenen thermodynamischen und hydrodynamischen Bedingungen untersucht. Der Einfluss von zwei verschiedenen industriellen Schmierstoffen, die mit Wasser in unterschiedlichen Verhältnissen (als Suspensionen und Lösungen) gemischt werden, auf den Tropfenaufprall und die Siederegime wird untersucht. Die Wirkung von Aditiven auf das Ergebnis des Tropfenaufpralls, insbesondere fester Graphitpartikel für die Suspensionen und organische Salze für die Lösungen,

wird für verschiedene Aufprallbedingungen untersucht. Hochgeschwindigkeitsvisualisierungen der Ergebnisse des Tropfenaufpralls werden entsprechend bekannten Wärmeübertragungsregimen klassifiziert: Blasensieden, thermische Atomisierung und Filmsieden. Der Einfluss von Partikeln wird in einem theoretischen Modell für die Wärmeübertragung im Blasensiederegime und bei der Partikelablagerung berücksichtigt.

Als Nächstes wird die transiente Sprühkühlung eines heißen dicken Substrats mit einer Schmierstofflösung experimentell untersucht. Die zeitliche Entwicklung des Wärmestroms und der Oberflächentemperatur eines ursprünglich homogen beheizten Substrats auf Temperaturen, die signifikant über dem Sättigungspunkt der Flüssigkeit liegen, wird während des kontinuierlichen Sprühaufpralls gemessen. Der Sprühaufprall wird zusätzlich mithilfe eines Hochgeschwindigkeits-Videosystems visualisiert, und der momentane lokale Wärmestrom und die Oberflächentemperatur werden zeitlich mit den Visualisierungen abgeglichen. Beobachtungen aus der vorliegenden Arbeit zeigen, dass bereits sehr geringe Konzentrationen von Schmierstoff den Wärmestrom dramatisch erhöhen, insbesondere bei hohen Wandtemperaturen, wo normalerweise beim Sprühkühlen mit destilliertem Wasser typischerweise Filmsieden beobachtet wird. Es tritt eine signifikante Erhöhung der Tropfenrückpralltemperatur auf, die oft mit dem Leidenfrostpunkt in Verbindung gebracht wird. Die Mechanismen, die zu der Erhöhung des Wärmestroms und der Verschiebung des Leidenfrostpunktes führen, werden identifiziert und diskutiert.

Die in dieser Arbeit vorgestellten Ergebnisse tragen zu einem umfassenderen Verständnis der zugrunde liegenden Physik bei, die für die Modellierung und Vorhersage von Sprühkühlprozessen mit industriell relevanten Flüssigkeiten erforderlich ist. Die Ergebnisse dieser Studie werden eine Grundlage für die Modellierung der Bildung der Schmierschicht durch Kühlungssprays bieten, was notwendig ist, um die Entwicklung ihrer Dicke und Gleichmäßigkeit vorherzusagen.

Acknowledgments

At the very beginning I would like to thank my supervisor Apl. Prof. Dr. Ilia V. Roisman. His advice, extraordinary support and guidance throughout the years have been essential for the success of this work.
Many thanks also go to Prof. Dr.-Ing. Jeanette Hussong and Prof. i.R. Dr.-Ing. Cameron Tropea for their co-supervision and countless helpful discussions and ideas. I would like to thank all three of them for giving me the opportunity to conduct my research at the Institute of Fluid Mechanics and Aerodynamics at the Technische Universität Darmstadt. Furthermore, I would like to thank Prof. Dr. Marco Marengo for refereeing this thesis and for taking the time to visit us in Darmstadt.

The financial support of the German Research Foundation (DFG) under grant SFB-TRR-75 (Transfer Project T02) is also gratefully acknowledged.

Working at the Griesheim campus was a real pleasure. I always thought we made a great team. I am very grateful to Jan Breitenbach and Benedikt Schmidt for the very warm and friendly welcome, for the introduction to the subject, and for all the help I needed to get started. I have really enjoyed my time on the campus, especially the short coffee breaks and long discussions with Maximilian Lausch, who quickly became my coffee buddy and main motivator. I also enjoyed sharing an office in Minimax with Kilian Köbschall, my gossip buddy, who was a great support whenever I needed him. Many funny conversations with Philipp Brockmann also contributed to the success of this thesis. I am very grateful to my lab buddy Niklas Apell, who was always a great buddy and tried to bring order and wise words into my daily work life. Many thanks also to the guys from Lichtwiese: Louis Reitter, Louis Krüger and Bastian Stumpf. I will miss you all, my fellow penglings! Thank you for the wonderful time at the Griesheim and Lichtwiese locations.
A big thank you goes out to Bastian, Philipp, Niklas and Max for proofreading of this thesis.

Special thanks go to Birgit Neuthe and Corinna Neumann from the administrative team and Ilona Kaufhold and her workshop team. My work over the past few years could not have been successfully completed without their support.

Last but certainly not least, I would like to express my deepest gratitude to my family, especially my parents Slobodan and Radica Gajević, who have always been the wind in my back and supported me through all my wanderings. I would also like to thank my friends, both at home in Serbia and over here in Germany, for their constant support and faith in me. Thank you, Darko, Jovana and Milka. A big thank you goes to my best friend Darko, who has been by my side throughout my entire education, always cheering me up and telling me how proud he is.

A very special thank you goes to Ivan for accompanying me on this journey, for his constant support, love and understanding.

Thank you.

Maja

Contents

1 Introduction

Section 1.1 of the current chapter provides the main motivation of the study and a brief overview of the background. It summarizes the essential findings to contextualize the results presented in Chapters 5, 6, and 8. The chapter terminates with Section 1.2. This section outlines the objectives for the present thesis, which are motivated by the current limitations in the understanding of the governing phenomena in spray cooling by multicomponent liquids. Parts of the following sections have been published in Gajevic Joksimovic et al. (2023a,c).

1.1 Motivation

Spray cooling provides a high and nearly uniform heat flux, resulting in outstanding cooling performance surpassing other cooling technologies. This is also demonstrated in Fig. 1.1 where ranges of typical heat transfer coefficients of common cooling technologies are shown.

Therefore, given its ease of application, spray cooling of a heated surface is found in a broad range of industrial processes. A few examples include wall impact of a fuel spray in engines (Meingast et al., 2000; Lahane & Subramanian, 2014) or gas turbines, in selective catalytic reduction (SCR) systems of diesel driven vehicles (Schmidt et al., 2021a), as well as in a multitude of other systems. Spray-induced cooling is also used during die forging, hot mill rolling (Chen & Tseng, 1992) and cooling of power electronics (Chen et al., 2022a). These diverse applications demonstrate the complex nature and versatility of spray cooling.

An extensive overview of spray cooling technology, with water or other one-component liquids being used as a working fluid, can be found in Kim (2007); Panão & Moreira (2009); Cheng et al. (2016); Liang & Mudawar (2017a,b); Breitenbach et al. (2018). For moderate temperatures that do not exceed the saturation temperature, the cooling is realized mainly through the

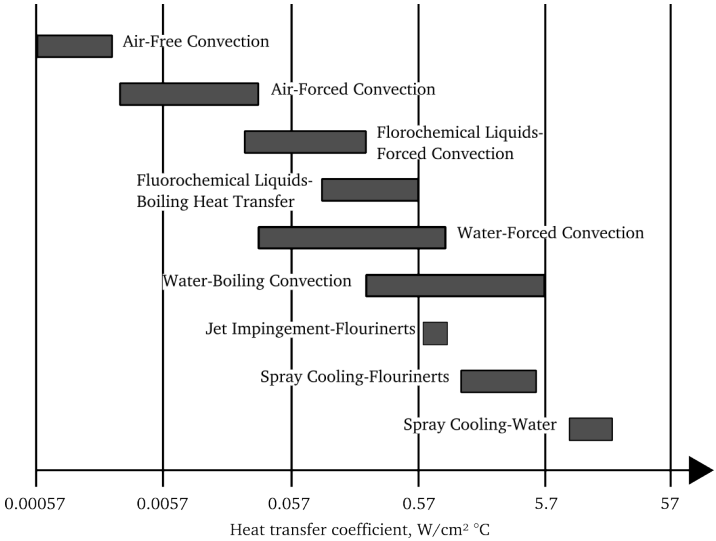

Figure 1.1: Heat transfer coefficient of different cooling technologies. (Adapted from Sienski et al. (1996), with permission of IEEE. © 1996 IEEE.)

impact of single drops (Yarin et al., 2017), heat convection in a thin liquid wall film and through the evaporation at the free surfaces of the liquid layer. The cooling is enhanced significantly on structured substrates due to the local cooling in the neighborhood of the three phase contact lines (Sodtke & Stephan, 2007; Zhang et al., 2013; Xu et al., 2022).

At higher wall temperatures, the process is accompanied by boiling and is significantly affected by the corresponding thermodynamic phenomena. Different regimes have been observed during spray cooling at various wall temperatures and spray impact parameters. These include the nucleate boiling regime (Liang & Mudawar, 2017a; Breitenbach et al., 2017a), characterized by the heterogeneous nucleation of multiple bubbles on the wetted part of the solid surface; the transition regime, when the substrate surface is not uniformly wetted due to the percolation of the vapor in channels formed by the coalescence of the bubbles (Schmidt et al., 2021b); the film boiling regime (Liang & Mudawar, 2017b; Breitenbach et al., 2017b; Castanet et al., 2018), characterized by the complete rebound of the impacting drops; and the

thermal atomization regime, distinguished by the generation of an intensive flow of fine secondary drops (Roisman et al., 2018) in the case of high impact velocities of the primary drops. In order to simplify physical modeling of the associated thermal-hydraulic phenomena, a spray can be approximated as an aggregate of individual dispersed droplets, meaning that mechanisms governing the impact of individual drops onto a heated surface need to be well understood as well in order to understand the overall process (Breitenbach et al., 2017b).

Most of the present work available in the literature is predominantly focused on pure, one-component liquids, with distilled water being the most commonly used liquid. However, quite recently, application of complex, multicomponent liquids for the enhancement of spray cooling started to attract increased attention. As a result, spraying liquids often represent a multicomponent mixture of water and lubricants and perform not only a role in cooling, but also in lubrication, for example, in cooling of tools and mechanical parts in the forging industry. Such industry level liquids, suspensions, emulsions and solutions, are designed not only to cool, but also to reduce wear and friction.

Accordingly, the attention of various researchers has been directed first and foremost towards the study of drop impact of a variety of compound drops (Blanken et al., 2021) as well as impact on lubricated and coated surfaces (Pack et al., 2017; Esmaili et al., 2021). Binary drop splashing, such as particle dispersion (Thoraval et al., 2021), as well as numerous effects occurring during heat transfer between the heated substrate and the impacting drop, were intensively studied for different experimental system configurations (Weickgenannt et al., 2011; Piskunov et al., 2021).

The behavior and properties of the multicomponent liquid during spray cooling of hot substrates can change significantly due to partial liquid evaporation. Intensive local evaporation leads to the rapid increase in the concentration of the less volatile components close to the wall. Depending on the boundary conditions, this phenomenon leads to the deposition/accretion of the dissolved/dispersed phase of the used liquid on the wall surface, and may influence the local heat transfer, as shown in Section 5.1.2. In some applications, this process is used to apply surface coatings or lubricants. On the other hand, in other applications, such as engine fuel sprays, fuel deposition is not a desirable process (Arters & Macduff, 2000).

The main factors influencing the behavior of multicomponent liquids in

a single drop/spray impacting a hot substrate have yet to be identified and analyzed. It is not entirely clear how the additional components in industrial lubricants affect the drop impact regimes, Leidenfrost point, and heat flux values. Indeed, it is challenging to try to fully understand and analyze the physical processes that occur from the single drop impact, which is the central element of the spray-wall interaction, to the spray impact on a hot substrate.

The motivation for the Transfer project, which led to the idea for this thesis, focuses on cooling and lubrication during hot forging. In the hot forging industry, metal billets are heated to temperatures above 1000 °C and pressed between dies to achieve the desired geometry of the final product. Examples include crankshafts, gears, and other parts used in industrial machinery and consumer products. Power dies must be cooled after each work cycle to prevent thermo-mechanical fatigue. In addition, to reduce friction between the dies and the metal workpiece, the dies must be coated with the lubricating liquid. This coating is achieved by adding lubricants to the cooling liquid, and cooling and lubrication are often carried out in parallel by a single spraying process. The forging industry is particularly interested in the evolution of the die temperature during spray cooling for both pure water and lubricants as a working fluid. This allows the minimum allowable cycle time to be determined and the optimum amount of lubricant to be selected depending on the specific operating conditions. By shortening the necessary cooling time, the total process time for the production of each part can be reduced, resulting in increased productivity and efficiency.

To this day, the physics of spray cooling of heated surfaces and simultaneous lubrication are not fully understood. Predictive tools in the industry currently rely mostly on empirical correlations and lack universality. Therefore, a laboratory investigation of the thermodynamic and hydrodynamic phenomena of a single drop/spray impact on a heated smooth or contaminated substrate at different lubricant concentrations is strongly needed, including the description of the heat transfer and the residual shape of the lubricant layer.

1.2 Objectives and outline of this thesis

The main objective of this experimental study is to investigate the influence of two types of industrial lubricants on spray cooling and deposition of additives. For this purpose the present work comprises two subjects: the study of a single drop impact and the study of spray cooling.

In the first part, a setup is designed and constructed to perform a single drop experimental study and investigate the influence of graphite-based and organic salt-based industrial lubricants. The influence of the mentioned additives on the drop residence time and the drop impact regimes during the interaction of the drops with a heated substrate is captured by high-speed imaging, which allows the identification of the main hydrodynamic and thermodynamic regimes. Due to the nature of the applied liquids, characterization of the remaining solid layer on the substrate is required and leads to the development of a theoretical model capable of predicting the layer thickness, as shown in Section 5.1.2.

The single drop study is followed by a spray study in the second part, where temperature and heat flux measurements are performed on a adapted experimental setup. The continuous cooling of a thick metal target from 445 °C to 100 °C enabled the observation of a transient phenomena during spray cooling. These measurements are accompanied by high-speed visualizations of an impacting spray at different times during the cooling process, allowing the identification of the different hydrodynamic and thermodynamic regimes of spray cooling, as well as the influence of lubricant concentrations on the latter. During the experiments, mechanisms for enhancing heat transfer are identified through the newly captured foaming effect.

It should be noted that both the graphite-based industrial lubricant mixed with water in various proportions (suspensions) and the organic salt-based industrial lubricant mixed with water in various proportions (solutions) were used for the single drop campaign, while the spray campaign was conducted with the latter only, due to time constraints.

The outline of the thesis is therefore mainly organized into two parts, with Part I related to the single drop campaign and Part II related to the spray campaign.

Chapter 2 describes the theoretical background and state of the art, related to the single drop as well as spray impact onto a hot substrate. The chapter

is organized by means of elevation from different regimes of isothermal drop and spray impact to the regimes of drop and spray impact on a hot substrate, followed by spray cooling. The chapter concludes with an introduction to complex liquids, some of which were used in the campaign, and their expected influence on the drop and spray dynamics.

Chapter 3 provides a brief overview of the experimental methods used throughout the whole experimental campaign, introducing different configurations of experimental setups as well as the properties of the lubricant suspensions/solutions used in this study and their manner of preparation.

Chapter 4 shows an in-depth description of the different configurations of the single drop experimental setups and the measurement techniques employed for characterization and analyzing of drop impact phenomena.

In **Chapter 5** different observed regimes of the impact of a suspension drop onto a hot substrate are presented. A description of the thermodynamic and hydrodynamic phenomena is given, along with high-speed visualizations. The model for heat transfer and particle deposition in the nucleate boiling regime is developed in Section 5.1, followed by thickness determination and analysis of the solid residue that remains on the substrate after liquid evaporation. The chapter concludes with Section 5.2, in which the effect of solid particles as an integral part of a lubricant suspension on the Leidenfrost point is investigated.

Next, in **Chapter 6**, the phenomenological observations of solution drop impact onto a heated substrate are described, and the potential influence of organic salt-based lubricant addition on the hydrodynamics of drop impact and heat transfer regimes is discussed. These observations are compared with those of suspension drop impact, presented in Chapter 5. The observations in this chapter serve only as a basis for the investigation of spray cooling with the same liquid, lubricant solution, in the following chapters.

Chapter 7 provides a detailed description of the spray setup configuration and the measurement technique, which is used to calculate the heat flux and surface temperature at the substrate surface during transient spray cooling.

In **Chapter 8** the investigation of the heat flux during spray cooling by lubricant solutions is presented, followed by visual observations of the spray impact. This is complemented by remarks on the influence of lubricant solutions on the Leidenfrost point and the film boiling regime with a detailed analysis. In order to predict the conditions that determine the Leidenfrost point and to differentiate the exact influence of salts and other lubricant

components, additional experiments with salt solutions (only salt dissolved in water) were carried out. The experimental data are analyzed and compared (lubricant solutions, salt solutions and pure water) and the main influencing parameters are identified.

Finally, **Chapter 9** concludes this thesis and offers an outlook for topics to be addressed in future studies.

2 Theoretical background and state of the art

This chapter addresses the current theoretical background relevant to the different drop and spray impact phenomena investigated in this thesis. For this reason, chapter is divided into three sections. Section 2.1 of this chapter gives a brief overview of the hydrodynamics of isothermal drop impact. Then, in Section 2.2, a detailed critical review of a relevant case of non-isothermal drop-wall and spray-wall interaction is given. The chapter concludes with the introduction of complex liquids in Section 2.3, and their expected influence on the hydrodynamics and thermodynamics of the drop/spray impact. Parts of the following sections, including text and figures, have been published in Gajevic Joksimovic et al. (2023c).

2.1 Hydrodynamics of isothermal drop and spray impact

The hydrodynamics of isothermal drop impact is already well understood and described. Most of the phenomena were already observed in the comprehensive work of Worthington & Clifton (1877), which considered the different patterns left by drops of various liquids impacting with different impact parameters on a hydrophobic glass plate. Following this early work, Worthington & Cole (1897) observed the splashing phenomenon of a liquid impacting on a solid or a liquid. These groundbreaking studies laid the foundation for numerous researchers to investigate various aspects of isothermal drop impact on solid or liquid surfaces. Subsequent work focused on diving deeper into the subject, fostering a comprehensive understanding, systematic classification of observed phenomena, and the development of reliable models (Roisman et al., 2002; Yarin, 2005; Marengo et al., 2011; Roisman et al., 2015).

Drop impact on a dry substrate is an important phenomenon related to

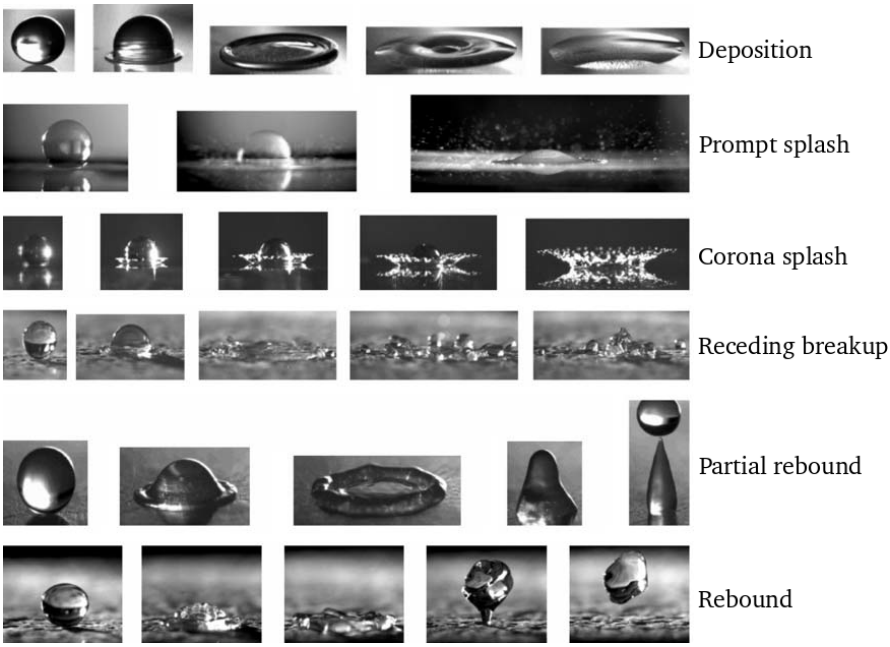

Figure 2.1: Different isothermal drop impact outcomes on solid substrates with different roughness and wettability. (Reprint of Rioboo et al. (2001) with permission of Begel House Inc. © 2001 Begel House Inc.)

spray cooling in the very initial phase of spray impact, when no liquid film has accumulated on the surface. When a drop impacts a solid substrate in the isothermal case, it forms a radially spreading thin liquid film, *i.e.*, a lamella. The lamella is bounded by a rim created by capillary forces and the stresses associated with the viscosity of the liquid (Taylor, 1959; Roisman et al., 2002). Various impact outcomes for an isothermal drop impacting a solid surface can be classified as follows: deposition, prompt and corona splash, receding breakup, partial rebound and rebound (Rioboo et al., 2001). The observed drop impact phenomena are briefly summarized and explained below (Rioboo et al., 2001; Josserand & Thoroddsen, 2016; Palacios et al., 2013), and additionally depicted in Fig. 2.1.

- **Drop deposition** is only achieved if the drop deforms and remains on the substrate throughout the impact process without any drop breakup.
- **The prompt splash** is characterized by the generation of the fine droplets at the very beginning of the drop spreading phase, positioned directly at the contact line. The prompt splash is influenced by the surface structure.
- **Corona splash** occurs when droplets are formed around the edge of a crown, far from the solid surface.
- **Receding breakup** is mainly observed on a hydrophobic substrate, when the drop liquid recedes from the maximum spreading diameter.
- **Rebound and partial rebound** occur only after drop impact onto a hydrophobic surface with a relatively small Weber number, when a receding phase is observed.

The main impact parameters that determine the outcome of an isothermal single drop impact, are the drop impact velocity U_0 and the initial drop diameter d_0. The flow generated by the drop impact and the hydrodynamic phenomena are determined by the Reynolds and Weber numbers

$$\mathrm{Re} = \frac{d_0 U_0}{\nu}, \quad \mathrm{We} = \frac{\rho d_0 U_0^2}{\sigma}, \tag{2.1}$$

where ρ, σ and ν are the density, kinematic viscosity and surface tension of the drop liquid, respectively. In some cases, it is more convenient to use some combinations of the Reynolds and Weber numbers. These combinations include the capillary number and the Ohnesorge number

$$\mathrm{Ca} = \mathrm{We}/\mathrm{Re}, \quad \mathrm{Oh} = \mathrm{We}^{1/2}/\mathrm{Re}, \tag{2.2}$$

respectively.

During drop spreading, when the thickness of the lamella is much larger than the thickness of the viscous boundary layer that expands near the substrate, the effect of viscosity is negligible. Remote asymptotic solution for the flow in the lamella, developed from the mass and momentum balance (Yarin & Weiss, 1995; Roisman et al., 2009) yields the expression for the evolution of

the lamella thickness in the form $h_{\text{lamella}} \sim d_0^3 U_0^{-2} t^{-2}$, where d_0 and U_0 are the drop diameter and impact velocity, respectively.

The thickness of the viscous boundary layer in the spreading drop is scaled as $h_{\text{viscous}} \sim \sqrt{\nu t}$ (Roisman, 2009). At some instant, denoted t_ν, the thickness of the lamella becomes comparable with the thickness of the viscous boundary layer, such that viscous effects affect the dynamics. This time and the corresponding lamella thickness h_ν at this instant can be estimated in the form

$$t_\nu \sim \frac{d_0}{U_0}\mathrm{Re}^{1/5}, \quad h_\nu \sim d_0 \mathrm{Re}^{-2/5}. \tag{2.3}$$

At times $t > t_\nu$ the flow in the lamella is governed by the viscous stresses, which lead to a fast decay of the spreading. The final, residual lamella thickness resulting from the normal impact of a drop on a smooth, flat substrate, is scaled well by the expression for h_ν (Roisman, 2009):

$$h_{\text{res}} \sim 0.79 d_0 \mathrm{Re}^{-2/5}. \tag{2.4}$$

In addition to lamella thickness, the maximum spreading diameter of a drop is an important parameter that plays a decisive role in various industrial applications, as it directly affects the contact area between the impacting drop and the substrate. For example, the maximum spreading diameter is one of the significant criteria affecting the quality of inkjet printing and is essential for different spray coating applications.

The maximum spreading diameter and the spreading dynamics during drop impact have been studied experimentally at different size scales, with a primary focus on the milimeter-sized drops (Lagubeau et al., 2012; Cheng, 1977). Some approaches to define a maximum spreading diameter are discussed below.

When defining a maximum drop spreading diameter, it is more convenient to define it in terms of the spreading factor, $\overline{D}_{\max} \equiv D_{\max}/d_0$. Clanet et al. (2004) measured the maximum spreading diameter for pure water and mercury drops hitting a superhydrophobic substrate. This led to the scaling of the dimensionless maximum spreading diameter as $\overline{D}_{\max}\mathrm{Re}^{-1/5}$. The scaling is determined as a function of a dimensionless parameter $P = \mathrm{We}\,\mathrm{Re}^{-4/5}$ that accounts for inertial, viscous and surface tension related effects. For the low viscosity liquid, which is considered to be an almost inviscid case ($P < 1$), the maximum drop diameter is determined solely by the capillary number and can

be scaled as $\overline{D}_{\max} \sim \mathrm{We}^{1/4}$. This case is likely to be observed at low velocities, low viscosities and high surface tension, also called the capillary regime. It is found to be almost independent of drop size (Clanet et al., 2004). On the other hand, in the viscous regime ($P > 1$), the spreading of the drop is expected to be limited by the effect of viscosity and the maximum drop diameter is mainly determined by the impact Reynolds number, $\overline{D}_{\max} \sim \mathrm{Re}^{1/5}$.

Scheller & Bousfield (1995) and Marmanis & Thoroddsen (1996) found that the dimensionless parameter $K = \mathrm{Re}^{1/2}\mathrm{We}^{1/4}$ correlates well with the spreading factor $\overline{D}_{\max}$ which is the ratio of a maximum spreading diameter to the initial drop diameter. For example, the proposed empirical scaling relation by Scheller & Bousfield (1995) shows strong agreement with experimental data

$$\overline{D}_{\max} = 0.61K^{0.332}. \tag{2.5}$$

In addition, an energy balance approach is often used to evaluate the geometry of the spreading drop: its average height and maximum diameter. Such estimates were obtained in the early works of Chandra & Avedisian (1991); Collings et al. (1990) and later in Wildeman et al. (2016). All of the aforementioned works used an approach that compares the initial kinetic and surface energy of the impacting drop with the surface energy of the spreading lamella, taking into account the energy loss due to the viscous dissipation.

Finally, the model for the maximum spreading diameter from Roisman (2009) uses the residual lamella thickness h_{res}, defined in Eq. (2.4), as a characteristic length scale, and accounts for the motion of the rim under the action of surface tension, resulting in the semi-empirical relation

$$\overline{D}_{\max} = 0.87\mathrm{Re}^{1/5} - 0.40\mathrm{Re}^{2/5}\mathrm{We}^{-1/2}. \tag{2.6}$$

However, the effect of the viscous stresses on the rim velocity is neglected in the scaling analysis above (Roisman, 2009) since the ratio of the viscous force to the surface tension is negligibly small for the experiments considered, but at the same time, the expression agrees well with the existing experimental data for a wide range of the impact parameters. For very viscous liquids, liquids with low surface tension, or very small drops, this term may become significant and the proposed simple scaling relation from Eq. (2.6) will no longer be valid.

Therefore, the following expression (Butt et al., 2014) is recommended in this case

$$\overline{D}_{\max} = 0.87\mathrm{Re}^{1/5} - 0.48\mathrm{Re}^{2/5}\mathrm{We}^{-1/2}, (\theta_c \to \pi), \tag{2.7}$$

for superhydrophobic substrates, where θ_c is the contact angle of the substrate.

2.1.1 Drop impact onto a dry and wetted substrate

Isothermal drop impact outcomes are highly dependent on the drop impact parameters (described by the Reynolds and Weber numbers), the type of liquid, and the surface conditions (Marengo et al., 2011; Aboud & Kietzig, 2015; Mandre & Brenner, 2012). A variety of different surface conditions in combination with different drop impact parameters have been extensively studied and modeled, leading to a comprehensive understanding of the phenomena that occur. For example, for simple surfaces, *i.e.*, smooth surfaces, the outcome of a drop impact can already be well predicted over a wide range of impact parameters, including quantitative values of drop spreading dynamics and splashing behavior. It is also known that the splashing threshold for corona splash of a drop impacting a dry smooth substrate is influenced by the mechanical properties of the ambient gas, which can be varied by changing the ambient pressure (Xu et al., 2005). Many attempts have been made to correlate the splashing threshold with the well known dimensionless parameter $K \equiv \mathrm{We}^{1/2}\mathrm{Re}^{1/4}$, mentioned in the previous subsection. However, more recent experiments (Palacios et al., 2013) have shown that this parameter is only applicable for a limited range of drop impact parameters. The correlation for the boundary between drop deposition and corona splash is given in Roisman et al. (2015) as:

$$\mathrm{Ca}_{\mathrm{corona}} = 0.067 + 0.6\mathrm{Oh}^{0.35} \text{ for } \mathrm{Re} < 450 \ , \tag{2.8}$$

$$\mathrm{Oh}_{\mathrm{corona}} = 0.044 \text{ for } \mathrm{Re} > 450 \ . \tag{2.9}$$

Impacts on more complex surfaces, either morphologically or chemically, involving textured or porous surfaces, or surfaces with non-uniform wettability characteristics, are widely found in many industrial applications. Marengo et al. (2011) show the influence of different materials such as rough glass, rough ceramic, porous stainless steel, porous bronze and porous PTFE, thus covering a wide range of different surface materials and conditions. Finally, they show that the effect of surface wettability becomes more pronounced when the wettability of the substrate is not uniform.

On the other hand, when a drop hits a dry surface at high velocity, it will atomize into secondary droplets. These small droplets are generated by one of two types of splashes: either a prompt splash from the spreading rim at the surface or a thin corona splash, that levitates from the surface. A criterion for determining the critical velocity at which a drop impacting a smooth, dry surface either spreads over the substrate or disintegrates into smaller droplets was derived in Riboux & Gordillo (2014). Later on, Riboux & Gordillo (2015) also proposed a model for predicting the sizes and velocities of ejected fragments. Burzynski et al. (2020) observed typical breakup regimes at relatively high impact velocities for water, ethanol and acetone drops. Prompt splash, characterized by the emergence of multiple jets without corona formation, has typically been attributed to the impact of drops on rough or structured surfaces (Marengo et al., 2011; Roisman et al., 2015). In these cases, the surface morphology affects the flow of the spreading lamella and contributes to the ejection of jets (Yarin et al., 2017). Roughness promotes the phenomenon of prompt splash and porosity leads to the partial liquid penetration and subsequent target imbibition (Rioboo et al., 2008; Moita & Moreira, 2011). However, the attribution of prompt splash cannot be exclusively related to the surface morphology itself, as this splashing regime was also observed by Burzynski et al. (2020) on smooth surfaces at higher Reynolds numbers and thus higher impact velocities.

For example, the corona splash formed on dry surfaces differs significantly from the corona observed after a drop impact on a liquid film. These differences can be clearly seen by comparing the corona splash images for a single drop impact on a dry surface (see Fig. 2.1) and a surface wetted by a liquid film, shown in Fig. 2.2. Typical outcomes and splash regimes for a drop impact on a liquid film have been summarized in detail in the works of Kittel et al. (2018) and Stumpf et al. (2022).

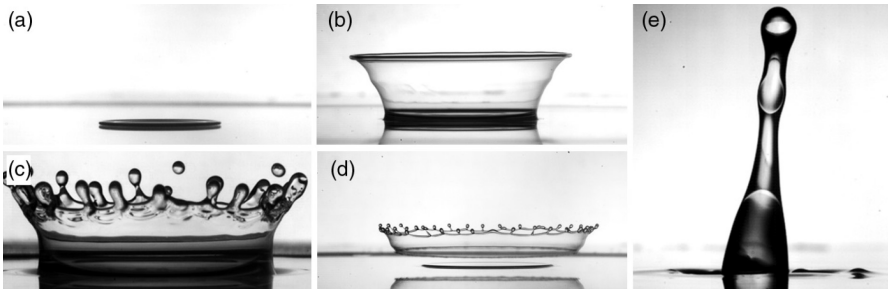

Figure 2.2: Typical outcomes and splash regimes for drop impact on a liquid film: (a) deposition, (b) corona formation without splash, (c) corona splash, (d) corona splash after detachment and (e) drop breakup. (Reprinted from Kittel et al. (2018), with permission of the American Physical Society. © 2018 American Physical Society.)

The outcomes of an isothermal drop impact onto a wetted substrate, depending on the impact parameters, can be grouped into: deposition, corona formation without splash, corona splash, corona splash after detachment, and drop breakup of a central jet formed after collapse of a crater, all of which are shown in Fig. 2.2. The main difference is the composition of the corona: for single drop impact on a wetted surface, the corona is formed by the liquid from the surface film and the drop, while the corona of a single drop impact on a dry surface contains only liquid from the drop. Splashing of drops on wetted surfaces is the result of rim instability, which leads to fingering (Yarin et al., 2017).

Drop impact on a wetted substrate can also lead to phenomena such as jetting or local dewetting (Roisman et al., 2006). Here, the impacting drop first penetrates the wall liquid film, creating a crater. This crater expands and then retracts due to capillary forces and gravity. If the impact velocity of the drop is relatively low, the impact creates a series of circular waves that expand on the wall film. At higher impact velocities and higher surface tensions, the retraction of the crater can lead to the formation of a central jet. In some cases, this jet will break up, resulting in partial rebound of the drop.

2.1.2 Atomization and sprays

There have been various attempts to model the spray impact phenomenon in terms of predicting wall flow and secondary spray. In the following, two selected modeling strategies, the superposition of single drops and the statistical approach, are briefly explained. The first strategy is based on representing the spray impact as a superposition of single drop impact events. In other words, spray is considered as an aggregate of single drops.

Cossali et al. (2005) presented and compared six different single drop empirical models for spray impact on solid substrates. These simplified impact models are widely used in the numerical simulations of spray impact onto solid walls, since the direct simulation of multiple drop impact is computationally demanding. These models are typically semi-empirical, based on single drop impact experimental data and some reasonable constraints to allow extrapolation to different impact conditions. However, Tropea & Roisman (2000) showed that the result of the spray impact cannot be fully predicted with the above mentioned superposition approach, due to the interactions between drops and the fluctuations of the liquid wall film. An empirical model of spray impact on solid surfaces, taking into account the interaction of adjacent impacts, has therefore been proposed by Tropea & Roisman (2000). More recent research in this area has been focused on industrially relevant spray-wall interactions, which have a significant impact on the fuel-air mixing process in engines, by proposing a model that accounts for the mass flux and dynamic pressure generated by an impacting spray (Zhang et al., 2016). The proposed liquid film model can adequately reproduce the film dynamics, the film/wall heat flux, and the film evaporation rate under a wide operating range.

The second approach is statistical, based on a large number of spray impact measurements and data analysis to model the phenomenon under predefined parameters. Panão et al. (2020) give an insight into the statistical characterization of sprays. However, the statistical distributions of droplet diameter and velocity, local variation of spray flux, and droplet interactions make the study of the entire spray impact process highly complex. Furthermore, even in simple cases, it is still difficult to obtain detailed information of spray impact from experiments. Therefore, this approach is not further assessed.

The present work of this thesis focuses on the hydrodynamic and thermodynamic phenomena that occur during spray cooling of a hot substrate, which will be the main subject of subsequent analysis.

2.2 Fundamentals of spray cooling

The heat transfer response of a particular surface exposed to spray cooling can be quantified in terms of the heat flux dependence of the surface temperature throughout the process. This way of representing the relevant quantities during spray cooling (or any other cooling technology) is known in the literature as boiling curve (Liang & Mudawar, 2017a,b; Cheng et al., 2016). Such an exemplary boiling curve is shown in Fig. 2.3. The surface temperature is often shown as the surface overheat, which is defined as the difference between an instantaneous wall temperature and the saturation temperature of the spray liquid. The boiling curve in Fig. 2.3 shows the different heat transfer regimes encountered at different surface temperatures during the spray cooling process. Boiling regimes were first observed in the pioneering work of Nukiyama (1966) from pool boiling experiments.

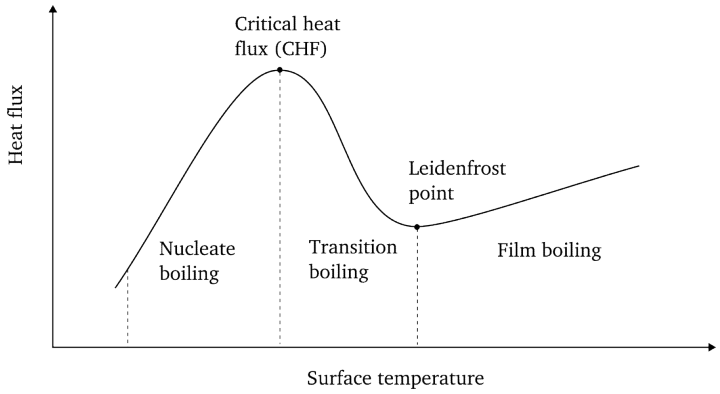

Figure 2.3: Exemplary evolution of the heat flux as a function of the surface temperature during spray cooling.

The resulting regimes will be briefly described below in terms of cooling a substrate that is already at a fairly high temperature, so that the plot in

Fig. 2.3 can be observed from right to left, starting with the highest surface temperature at the start of cooling. Presenting the data in this way highlights known boiling regimes as well as important points on the curve.

- At rather high surface temperatures, drops on the surface have no contact with it, and a vapor layer between the drops and the substrate wall acts as an insulating layer, preventing direct contact of the liquid with the hot substrate. This regime is referred to as the **film boiling regime**. Accordingly, the heat flux in this regime is relatively low (Leidenfrost, 1966).
- As the cooling continues, the surface temperature will decrease further while the heat flux will eventually reach a minimum at some point. This point is called the **Leidenfrost point**. Accordingly, the corresponding surface temperature is called the Leidenfrost temperature.
- Subsequently, the heat flux increases rapidly due to the formation of liquid patches on the substrate identifying a **transition boiling regime** that is very short in duration.
- At a certain point, the highest heat flux is reached, *i.e.* the **critical heat flux (CHF)**, which is the local maximum of the curve. The heat flux in this regime, associated with **nucleate boiling regime**, is relatively high because the liquid is in contact with the hot substrate and the wall temperature is slightly above the saturation temperature.

The enumeration above does not include the single-phase cooling regime, which is defined as a heat transfer regime that is not accompanied by boiling. This is due to the fact that in this case the heat transfer rates between the spray and the wall are relatively low compared to the regimes accompanied by boiling. For this reason, spray cooling without boiling is not the main focus of the heat transfer literature compared to spray cooling in different boiling regimes. Still, it is a significant research topic (for example, for cooling microelectronic chips), and in the past valuable research has been done to study the non-boiling regime (Hsieh et al., 2014; Rybicki & Mudawar, 2006) for surface temperatures below the onset of boiling, known as the liquid saturation point. Heat transfer in this regime is mainly governed by heat conduction in the wall and heat convection in the wall film flow.

In the next sections, a comprehensive review of the phenomena associated with the different boiling regimes during spray cooling of a hot substrate and their modeling approaches will be discussed. First, the impact of a single drop on a hot substrate is considered for different boiling regimes as a key element of the spray cooling process.

2.2.1 Drop impact onto a hot wall

As discussed earlier in Section 2.1, when a drop impacts a solid substrate in the isothermal case, it forms a radially spreading thin liquid film, *i.e.* a lamella. The lamella is bounded by a rim formed by surface tension and viscous forces. If the substrate is partially non-wettable, capillary forces acting on the rim initiate its receding motion (Roisman et al., 2002). The impact of a drop on a hot substrate with a temperature below some critical value slightly above the saturation temperature is not accompanied by boiling and can still be modeled using the correlations obtained for isothermal cases (Moreira et al., 2010).

At higher temperatures, the flow can be significantly affected by phenomena related to fluid boiling near the wall - the dynamics of drop spreading and receding is significantly affected by various thermodynamic effects associated with different boiling regimes, schematically shown in Fig. 2.5. These regimes depend on the initial substrate temperature and its thermal properties (Bernardin et al., 1997; Breitenbach et al., 2018). Thermodynamic effects observed at different boiling regimes will be listed below.

- Vigorous bubble formation due to heterogeneous nucleation on the substrate within **the nucleate boiling regime**, as shown in Fig. 2.4(a) and illustrated in Fig. 2.5 (second image in the column). These bubbles are characterized by a growth rate and a residence time (also referred to as the "contact time" in certain literature) before they collapse. This regime is observed at temperatures slightly above the saturation temperature. Some superheating occurs during spreading, which is explained by the delay time before bubble generation starts at the substrate surface (Breitenbach et al., 2018).

- At higher temperatures, the relative area covered by the bubbles increases and, under certain conditions, leads to the percolation of vapor

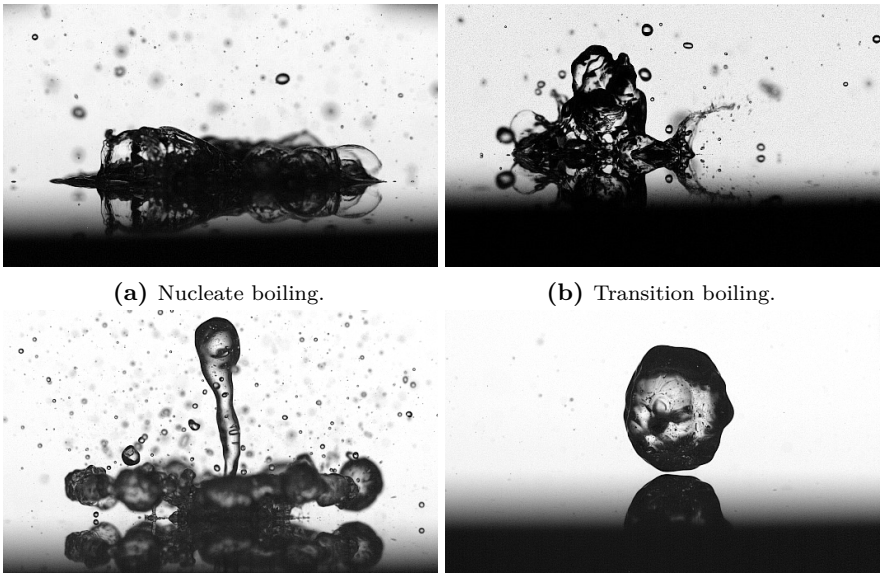

(a) Nucleate boiling.

(b) Transition boiling.

(c) Thermal atomisation.

(d) Film boiling.

Figure 2.4: Typical regimes observed for an impact of a distilled water drop onto a hot substrate. The impact parameters are drop diameter $d_0 = 2.3$ mm, impact velocity $U_0 = 1$ m/s at various initial wall temperatures, respectively, 170 °C, 240 °C, 340 °C, 420 °C.

channels (Schmidt et al., 2021b; Chantelot & Lohse, 2021) in **the transition boiling regime** (Fig. 2.4b). This is an intermediate regime between nucleate and film boiling, which is illustrated in Fig. 2.5.

- At even higher temperatures boiling occurs at the interface of a thin vapor layer within **the film boiling regime**, leading to drop rebound, as shown in Fig. 2.4(d) (Liang & Mudawar, 2017b; Tran et al., 2012; Breitenbach et al., 2017b; Piskunov et al., 2021; Castanet et al., 2018). This regime is observed at temperatures above the Leidenfrost point.

- At high impact velocities, severe liquid overheating leads to liquid film breakup by vapor flow in **the thermal atomization regime**, as exemplarily shown in Fig. 2.4(c) (Roisman et al., 2018; Emerson et al., 2021; Chen et al., 2022b). During the thermal atomization regime (see illustration in Fig. 2.5), a central part of the drop lamella is in contact with the substrate. However, the peripheral part of the lamella levitates in a fast vapor stream ejected near the contact line. The contact time of the drop before rebound and complete disintegration is determined by the time of thermal dewetting (Roisman et al., 2018).

Subsequent sections (2.2.2 and 2.2.3) cover the drop and spray impact in which boiling occurs. Nucleate boiling is discussed first, and then film boiling, due to the availability of modeling approaches in the literature. Since the time spent in transition boiling is very short, the transition between film boiling and nucleate boiling is often simplified and replaced by a heat flux jump (Tenzer et al., 2019). Models that account for transition boiling have yet to be developed. Recent observations have also discovered the thermal atomization regime (Roisman et al., 2018), although modeling approaches are still not fully elaborated and can be expected in the coming years as the following topic attracts the attention of various researchers.

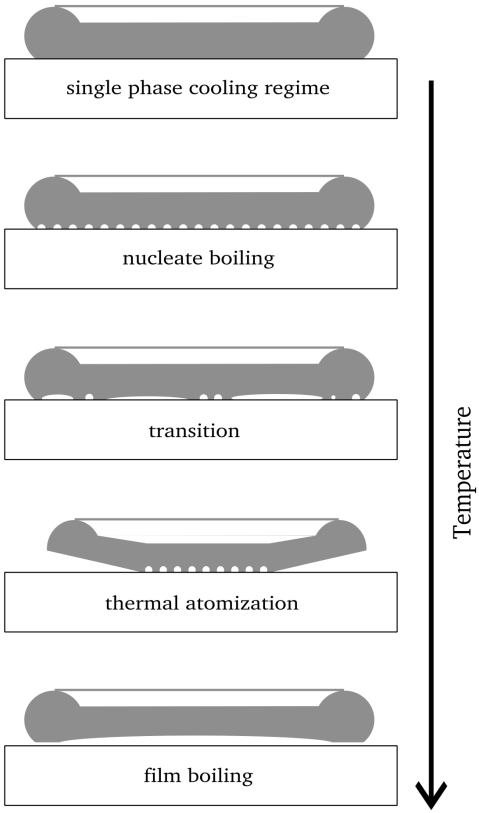

Figure 2.5: Main heat transfer regimes during drop impact onto a hot surface. (Reprinted (adapted) from Breitenbach et al. (2018) with permission from Springer Nature. © 2018 Springer Nature.)

2.2.2 Analysis of heat transfer during single drop impact onto a hot substrate

The physics of drop impact with boiling is fairly complex, hence most of the research in the past has been experimental, resulting in different boiling curves and empirical correlations for heat transfer. Therefore, the following is a brief overview of some of the available heat transfer modeling approaches for known heat transfer regimes from the literature.

The drop impingement on the hot substrate initiates the onset of heat transfer in the solid and liquid regions. In the solid wall, heat is transferred by conduction. In the liquid region, heat transfer is determined by the rather complex flow in the drop as it spreads, influenced by the formation of small vapor bubbles that commonly rise through the drop and coalesce with other bubbles. The heat transfer in the solid substrate under the sessile drop is theoretically analyzed by Breitenbach et al. (2017a). The total energy balance of the heat transfer from the evaporating sessile drop and the heat flux from the substrate is given by

$$\int_0^{t_c} A_c(t)\dot{q}(t)dt \approx \rho_l L^* \frac{\pi d_0^3}{6}, \tag{2.10}$$

where A_c is the contact area, t_c is the drop contact time, $\dot{q}$ is the heat flux density at the solid/liquid interface, d_0 is the initial drop diameter, ρ_l is the density of the liquid, and $L^* = L + \Delta H_0$ is the sum of the latent heat of evaporation L and the enthalpy difference ΔH_0 between the initial drop state and saturated liquid state. Eq. (2.10) is based on the assumption that the energy goes entirely into drop evaporation. This assumption is indeed valid for the cases of nucleate boiling, for which the relative mass of fine secondary droplets, generated during drop boiling, is small. Breitenbach et al. (2017a) estimated the ejected mass ratio in the nucleate boiling regime, with the absence of drop rebound to be less than 10% for the experimental conditions in their parameter range.

At the first instant of drop contact a thermal boundary layer develops in the substrate. The thickness of the thermal boundary layer is $\delta_\mathrm{w} \sim \sqrt{\alpha_\mathrm{w} t}$ where α_w is the thermal diffusivity of the wall material. Since the thickness of the boundary layer is much smaller than the drop diameter, which is estimated to be on millimeter scale, the heat conduction in the substrate

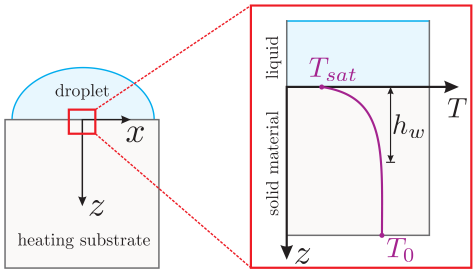

Figure 2.6: Sketch of the assumed temperature distribution within the solid material due to contact of a sessile droplet with the hot substrate. The solid/liquid interface is located at $z = 0$. (Reprinted from Breitenbach et al. (2017a), with permission of the American Physical Society. © 2017 American Physical Society.)

can be approximated by a one-dimensional model. The temperature at the solid/liquid interface is not uniform due to the formation of vapor bubbles during boiling. The temperature of the wall beneath the bubble and at the substrate in the relaxation layer outside the bubble is close to the saturation temperature T_{sat}, since it is determined by the liquid evaporation in the thin evaporation microlayer, as shown in Breitenbach et al. (2017a). Therefore, as a rough approximation, a nearly uniform interface temperature T_{sat} of the substrate can be assumed. The geometry and the definition of the coordinate system are shown schematically in Fig. 2.6. At $t = 0$ the liquid is placed in contact with a semi-infinite wall $z > 0$ at the initial temperature T_{w0}. The heat conduction equation in the wall

$$\frac{\partial T_{\mathrm{w}}}{\partial t} - \alpha_{\mathrm{w}} \frac{\partial^2 T_{\mathrm{w}}}{\partial z^2} = 0 \tag{2.11}$$

needs to be solved considering the boundary conditions

$$T_{\mathrm{w}} = T_{\mathrm{sat}} \quad \text{at } z = 0; \quad T_{\mathrm{w}} \to T_{\mathrm{w0}} \quad \text{at } z \to \infty; \tag{2.12}$$

where $T_{\mathrm{w}}(z,t)$ is the temperature in the wall region. Solving of Eqs. (2.11) and (2.12) leads to the the similarity solution (Roisman, 2010a):

$$T_{\mathrm{w}}(z,t) = T_{\mathrm{sat}} + (T_{\mathrm{w0}} - T_{\mathrm{sat}}) \mathrm{erf}\left(\frac{z}{2\sqrt{\alpha_{\mathrm{w}} t}} \right), \tag{2.13}$$

where erf is the error function. The heat flux density at the solid/liquid interface can be expressed with the help of Eq. (2.13) as

$$\dot{q}(t) \equiv \lambda_{\mathrm{w}} \left.\frac{\partial T_{\mathrm{w}}}{\partial z}\right|_{z=0} = \frac{e_{\mathrm{w}} \Delta T_{\mathrm{w}}}{\sqrt{\pi t}}, \tag{2.14}$$

where λ_{w} is the thermal conductivity of the wall material, e_{w} is the thermal effusivity, and $\Delta T_{\mathrm{w}} = T_{\mathrm{w0}} - T_{\mathrm{sat}}$ is the overall temperature difference in the wall (see Fig. 2.6). Taking into account the estimation of contact area $A_c \approx k_{\mathrm{w}} \pi d_0^2$ and substituting expressions (2.11), (2.12), (2.13) into initial expression (2.10), drop contact time can be estimated as:

$$t_c = \pi \left(\frac{\rho_l L^* d_0}{12 k_{\mathrm{w}} e_{\mathrm{w}} \Delta T_{\mathrm{w}}} \right)^2. \tag{2.15}$$

Coefficient k_{w} is determined primarily by the surface structure and wettability. It accounts also for the effective drop growth due to bubble expansion, for the mass loss during atomization and for some small deviation of the interface temperature from the saturation temperature. This coefficient is of order unity and can be estimated from different experiments, depending on experimental conditions (Breitenbach et al., 2017a).

Breitenbach et al. (2017a) validated the model by comparing the theoretical prediction for the contact time (Eq. 2.15) and demonstrated that the agreement between the contact times of their present work and those in the available literature (Tartarini et al., 1999; Abu-Zaid, 2004) is good, while the estimated value of the coefficient k_{w} is very close to the value obtained from the experiments.

Finally, with help of expressions (2.14) and (2.15), the time averaged heat flux of the drop evaporation can be expressed as:

$$\langle \dot{q} \rangle_c = \frac{24 k_{\mathrm{w}} e_{\mathrm{w}}^2 \Delta T_{\mathrm{w}}^2}{\rho_l \pi L^* d_0}. \tag{2.16}$$

If one now considers the impact of a single drop on a flat solid substrate in the **developed film boiling regime**, it is known that a drop of liquid in this regime is separated from the solid region by a vapor layer, as schematically shown in Fig. 2.7.

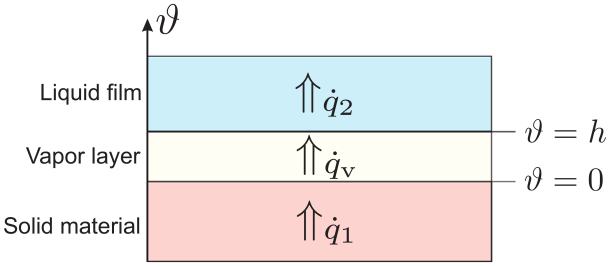

Figure 2.7: Sketch of the heat flow through the different regions: solid material, vapor layer, and liquid film. The solid/liquid interface is located at $\vartheta = 0$ and the liquid/liquid interface is located at $\vartheta = h$. (Reprinted from Breitenbach et al. (2017b), with permission from Elsevier. © 2017 Elsevier.)

Two thermal boundary layers arise in the liquid and the solid material, denoted $\delta_l \sim \sqrt{\alpha_l t}$ for the liquid film and $\delta_\mathrm{w} \sim \sqrt{\alpha_\mathrm{w} t}$ for the wall region, using the thermal diffusivities of the liquid film α_l and the solid wall α_w. Since both boundary layers are much smaller than the drop diameter, the heat transfer in the three separate regions (solid material, vapor layer and liquid film) can be approximated by a one-dimensional model. The contact temperature T_c at the solid-fluid interface $\vartheta = 0$ is unknown (see Figure 2.7 for the coordinate system illustration), while the temperature at the liquid interface can be approximated by the saturation temperature T_sat (Breitenbach et al., 2017a). Thermal radiation from the wall is not considered because it is much lower than the convective heat transfer (Rein, 2002). Therefore, the total energy balance equation, which includes the energy of liquid evaporation, can be expressed as

$$\dot{q}_1 = \dot{q}_\mathrm{v} = \dot{q}_2 + \rho_l L \frac{dh}{dt}, \tag{2.17}$$

where dh/dt is the change of vapor layer thickness, ρ_l and L are the density and the latent heat of evaporation of the liquid, respectively. The heat flow

through the different regions: solid material, vapor layer, and liquid film is denoted by $\dot{q}_1$, $\dot{q}_\mathrm{v}$ and $\dot{q}_2$, accordingly.

First, the transient heat flow in the liquid film must be considered. The flow in the drop can be approximated as an inviscid flow. The expression for the velocity field v, known from Yarin & Weiss (1995); Roisman (2010a), is substituted into the Eq. (2.17), which is then solved with the known initial and boundary conditions (Breitenbach et al., 2017b). The similarity solution is given by the following expression

$$T_l(z,t) = T_\mathrm{sat} + (T_\mathrm{d0} - T_\mathrm{sat})\mathrm{erf}\left[\frac{\sqrt{5z}}{2\sqrt{\alpha_l t}}\right], \tag{2.18}$$

where T_d0 stands for initial drop temperature. The associated heat flux at the liquid/liquid interface can be expressed in the form

$$\dot{q}_2(t) \equiv \lambda_l \frac{\partial T_l}{\partial z}\bigg|_{z=0} = \frac{\sqrt{5}e_l(T_\mathrm{sat} - T_\mathrm{d0})}{\sqrt{\pi}\sqrt{t}}, \tag{2.19}$$

where λ_l is the thermal conductivity and e_l is the thermal effusivity of the liquid film. Next, instationary heat flow in the solid wall has to be considered. The geometry and the definition of the coordinate system are shown schematically in Fig. 2.7. At $t = 0$ the vapor layer is in contact with a semi-infinite wall $\vartheta < 0$ at the initial surface temperature T_w0. Using the known heat conduction equation in the wall with the help of boundary conditions

$$T_\mathrm{w} = T_c \text{ at } \vartheta = 0;\ T_\mathrm{w} \to T_\mathrm{w0} \text{ at } \vartheta \to \infty, \tag{2.20}$$

where $T_\mathrm{w}(z,t)$ is the temperature in the wall region and the contact temperature T_c on the solid-fluid interface. After solving the similarity solution, the heat flux density at the solid/vapor interface can be expressed as

$$\dot{q}_1(t) \equiv \lambda_\mathrm{w} \frac{\partial T_\mathrm{w}}{\partial \vartheta}\bigg|_{\vartheta=0} = \frac{e_\mathrm{w}(T_\mathrm{w0} - T_c)}{\sqrt{\pi}\sqrt{t}}, \tag{2.21}$$

where λ_w is the thermal conductivity and e_w is the thermal effusivity of the solid wall material. The contact temperature T_c has to be determined from the overall energy balance of the spreading drop.

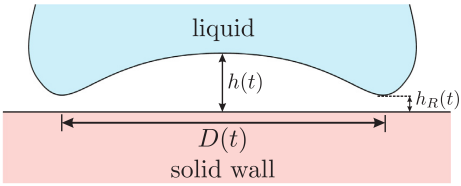

Figure 2.8: Sketch of the geometry of a vapour film during drop impact in the film boiling regime. (Reprinted from Breitenbach et al. (2017b), with permission from Elsevier. © 2017 Elsevier.)

Finally, the dynamics of vapor generation must be considered for the different stages of drop impact. In the initial stage of drop spreading, the vapor growth is mainly controlled by the heat transfer in the liquid and solid regions. The vapor film in the initial stage of drop spreading is shown shematically in Fig. 2.8.

The thickness of the vapor layer near the rim is much smaller than that in the drop center (see Fig. 2.8). Dawi et al. (2013) computed the vapor velocity in this region. The pressure in the central vapor region is governed by the pressure loss in the this thin gap near the drop rim, while the pressure in the vapor layer is determined by the inertia in the impacting liquid drop. The latter is estimated in Roisman et al. (2009) as $p \approx 1.7\rho_l U_0^2 \exp[-3.1tU_0/d_0]$. This pressure is significant only during the initial phase of drop impact and deformation $t_i \sim d_0/U_0$. At larger times the pressure influence is minor and the internal stresses in the vapor layer become significant. These stresses govern the drop floating at large time after drop impact and eventual rebound.

The heat transfer between the wall and the drop is inverse proportional to the vapor layer thickness. Therefore, the main part of the heat is transferred during the first stage of drop collision, when the gap thickness is smallest. In the following analysis only the heat transfer during the first heat transfer controlled growth stage is considered. The one-dimensional heat flux in the thin vapor layer can be roughly estimated as

$$\dot{q}_v(t) = \frac{\lambda_v}{h(t)}(T_c - T_{\mathrm{sat}}), \tag{2.22}$$

determined by the thermal conductivity λ_v of the vapor, the vapor layer

thickness $h(t)$, the saturation temperature T_{sat}, and the contact temperature T_c on the solid-liquid interface.

With help of expressions (2.17), (2.19) and (2.22), the contact temperature is obtained in the form

$$T_c = \frac{\sqrt{\pi}\lambda_{\mathrm{v}}\sqrt{t}T_{\mathrm{sat}} + e_{\mathrm{w}}h(t)T_{\mathrm{w0}}}{\sqrt{\pi}\lambda_{\mathrm{v}}\sqrt{t}T_{\mathrm{sat}} + e_{\mathrm{w}}h(t)}, \tag{2.23}$$

as a function of time t and vapor layer thickness $h(t)$. However, further substitution, derivation and transformation of the expressions (Breitenbach et al., 2017b) leads to the vapor layer thickness:

$$h(t) = K\frac{e_{\mathrm{w}}(T_{\mathrm{w0}} - T_{\mathrm{sat}})}{\rho_l L}\sqrt{t}. \tag{2.24}$$

It is important to note that the vapor layer thickness increases with the square root of time and is not influenced by the impact velocity of the drop. On the other side, the heat flux decreases inversely proportional. In the expression (2.24) K represents a dimensionless coefficient, determined as

$$K = \sqrt{(B-G)^2 + \frac{4G}{\sqrt{\pi}}} - B - G, \tag{2.25}$$

where

$$G = \frac{\sqrt{\pi}\lambda_{\mathrm{v}}\rho_l L}{2(T_{\mathrm{w}} - T_{\mathrm{sat}})e_{\mathrm{w}}^2};\ B = \frac{\sqrt{5}(T_{\mathrm{sat}} - T_{d0})e_l}{\sqrt{\pi}(T_{\mathrm{w0}} - T_{\mathrm{sat}})e_{\mathrm{w}}}. \tag{2.26}$$

With help of last three equations (2.24), (2.25) and (2.26), the contact temperature is explicitly expressed as

$$T_c = \frac{2GT_{\mathrm{sat}} + KT_{\mathrm{w0}}}{2G + K}. \tag{2.27}$$

From the above shown expression, Breitenbach et al. (2017b) show that the contact temperature is not a function of time and remains constant during drop impact as long as the boundary layer δ_{w} is much smaller than the solid substrate.

Furthermore, a comparison of the presented model (Breitenbach et al., 2017b) for the vapor layer thickness obtained a good agreement with experimental data (Tran et al., 2012). Breitenbach et al. (2017b) also estimated the total heat removed by a single impacting drop in the film boiling regime:

$$Q_{\text{single}} = \frac{4.63 d_0^{5/2} G e_{\text{w}} (T_{\text{w0}} - T_{\text{sat}})}{U_0^{1/2} (K + 2G)}. \tag{2.28}$$

Eq. (2.28) captures the influence of drop size and drop impact velocity on the total heat removed from a single drop in the same order as known correlations from the literature (Bernardin et al., 1997).

2.2.3 Spray impact accompanied by boiling

Before discussing the known modeling approaches for different boiling regimes during spray impact on a hot substrate, it is helpful to consider the heat transfer during transient spray cooling in a general sense. In the following cases observed in the literature, the substrate has been uniformly heated to the desired temperature prior to the start of cooling, thus allowing the detection of transient phenomena during the continuous cooling of the substrate.

For simplicity, in the following a one-dimensional heat conduction in a semi-infinite solid substrate is considered. Such an assumption is valid only if the thickness of the thermal boundary layer, $\sqrt{\alpha t}$, is much smaller than the thickness of the target exposed to the cooling process. In addition, the temperature gradients in this boundary layer must be much higher than the gradients associated with the spray distribution in the radial direction.

Tenzer et al. (2019) report a thermal boundary layer with a thickness of about 30 mm for a stainless steel target. The thermal boundary layer in the mentioned case is comparable to half the height of the target used. Therefore, when analyzing the heat conduction in the target, the wall can be considered as a semi-infinite body.

Consider a coordinate system z, t is fixed at the interface $z = 0$ of the observed semi-infinite target, which belongs to the interval $0 < z < \infty$, the temperature field $T(z, t)$ in the target can be calculated by solving the well-known one-dimensional heat conduction equation in the wall (Eq. 2.11) mentioned in previous sections.

According to Duahamel's theorem (Özisik, 1980), the solution that satisfies the boundary condition far from the target interface and the initial condition

$$T = T_{\mathrm{w0}} \text{ at } (t = 0 \ \wedge \ z \to \infty) \ \vee \ (t > 0 \ \wedge \ z \to \infty) \tag{2.29}$$

is

$$T(t) = T = T_{\mathrm{w0}} + \int_0^t A(\tau)\mathrm{erfc}\left[\frac{z}{2\sqrt{\alpha(t-\tau)}}\right] d\tau, \tag{2.30}$$

where $A(\tau)$ is a function determined by the conditions at the target interface $z = 0$, erfc is the complementary error function, and T_{w0} is the initial wall temperature.

The boundary $z \to \infty$ denotes a position at a finite distance much greater than the thickness of the thermal boundary layer in the wall. Eq. (2.30) gives the general solution for the interface temperature $T_i(t)$ and the heat flux $\dot{q}(t)$ as follows:

$$T_i(t) = T_{\mathrm{w0}} + \int_0^t A(\tau)d\tau, \ \dot{q}(t) = \frac{e_{\mathrm{w}}}{\sqrt{\pi}} \int_0^t \frac{T_i^{'}}{\sqrt{t-\tau}} d\tau \tag{2.31}$$

where

$$e_{\mathrm{w}} = \sqrt{\lambda \rho c_p} \tag{2.32}$$

represents the thermal effusivity of the wall material.

Modeling of temperature and heat flux evolution

The theoretical model presented in Section 2.2.2 for heat transfer from a single drop and during spray cooling in the film boiling regime published by Breitenbach et al. (2017b) has already been validated by comparison with experimental results from the literature (Wendelstorf et al., 2008). The total heat transferred during the impact of a single drop Q_{single}, materialized in Eq. (2.28), is determined by integrating the heat flux $\dot{q}(t)$ over the "apparent contact area" during the contact time. Roisman et al. (2018) show that the contact area cannot be based on the drop spreading diameter. Rather, due to

the high temperatures of the substrate wall associated with the film boiling regime, resulting in severe liquid overheating, and the high impact velocities of the impacting drops, the liquid film can rupture, causing the outer parts of the lamella to levitate. For this reason, Tenzer et al. (2019) propose the values of D^2 and D/U as scales for the contact area and for the contact duration, where U and D are the impact velocity and the drop diameter, respectively.

Finally, the work of Breitenbach et al. (2017b) followed by Tenzer et al. (2019) allows to predict the heat flux during spray impact in the film boiling regime

$$\dot{q} = Se_{\mathrm{w}}(T_i - T_{\mathrm{sat}}), \tag{2.33}$$

$$S = 8.85\chi \frac{\dot{m}}{\rho_{\mathrm{f}} D_{10}^{1/2} U^{1/2} \left[1 - b + \sqrt{(1-b^2) + w}\right]}, \tag{2.34}$$

$$w = \frac{8(T_{\mathrm{i}} - T_{\mathrm{sat}})e_{\mathrm{w}}^2}{\pi \lambda_{\mathrm{v}} \rho_{\mathrm{f}} L}, \; b = \frac{2\sqrt{5} e_{\mathrm{w}} e_{\mathrm{f}} (T_{\mathrm{sat}} - T_{\mathrm{f0}})}{\pi \rho_{\mathrm{f}} \lambda_{\mathrm{v}} L}, \tag{2.35}$$

where L is the latent heat of evaporation, χ is a dimensionless fitting parameter that depends on the wetting properties and roughness of the substrate (but is of the order of unity), T_{sat} is the saturation temperature of the liquid, and T_{f0} is the initial temperature of the spray liquid. The subscript "f" corresponds to the liquid (fluid) component, "w" to the wall, and "v" to the vapor. All terms were originally taken from Tenzer et al. (2019) for consistency in the analysis of spray effects with boiling. Most sprays in experimental studies as well as in actual applications are polydisperse, with different distributions of drop diameter and velocity in the spray. Hence, the average (mean) drop diameter and velocity, D_{10} and U, are used in the model. The χ parameter inherently accounts for the influence of the drop size and velocity distributions.

Consistently, Tenzer et al. (2019) used the model predictions of Breitenbach et al. (2017b) with certain mentioned adaptations for spray effects. The model used to predict the time evolution of the wall temperature during the film boiling regime of the spray process is briefly summarized in Eqs. (2.33) - (2.35).

Tenzer et al. (2019) then compared the model predictions in non-dimensional form with their experimental data. The comparison is made for different target materials (stainless steel, hot-work tool steel, and nickel), with a reasonably good agreement between their experiments and the presented theory. Although they observed some scatter with respect to their experimental data, they considered it acceptable due to the numerous sources of uncertainty of the measuring devices. On the other hand, the application of the model in dimensional form with experimental results obtained on a stainless steel target from Tenzer (2020) showed an apparently excellent agreement between experiments and model. In particular, the heat flux is predicted very well by the model. The spray parameters used for the the aforementioned validation case are: mean drop diameter $D_{10} = 43\,\mu\text{m}$, mean velocity $U = 10$ m/s, and mass flux $\dot{m} = 0.90$ kg/m^{2}s.

At some time t_L the surface conditions correspond to the Leidenfrost point. If the surface temperature at the Leidenfrost point is denoted as T_iL, the corresponding heat flux can be estimated using the equation (2.33). When considering a boiling curve of an experimentally measured data during spray cooling, the Leidenfrost point is determined as the point where the heat flux reaches its minimum in the film boiling regime (Tenzer et al., 2019; Gajevic Joksimovic et al., 2023a), as mentioned in Section 2.2 with respect to Fig. 2.3.

The value of the surface temperature corresponding to the Leidenfrost point is not a fixed value but depends on various quantities. For example, Tenzer et al. (2019) showed that it is highly dependant on the substrate material. A significant influence of nanostructures, surface morphology or wettability of the substrate on the Leidenfrost temperature is shown by Kim et al. (2012); Kruse et al. (2013); Takata et al. (2005). There are quite few correlations for the Leidenfrost temperature, indicating that the Leidenfrost temperature depends on the spray Weber number (Yao & Cox, 2002; Bernardin et al., 1997). Al-Ahmadi & Yao (2008) assume an influence of the mass flux on the Leidenfrost temperature. On the other hand, Tenzer et al. (2019) report a higher Leidenfrost temperature for stainless steel than for nickel, suggesting that the Leidenfrost point is dependent on the target material. However, Tenzer et al. (2019) assume that this temperature depends on the impact parameters of the drops, the mass flux density, but also on the rate of wall cooling in the film boiling regime.

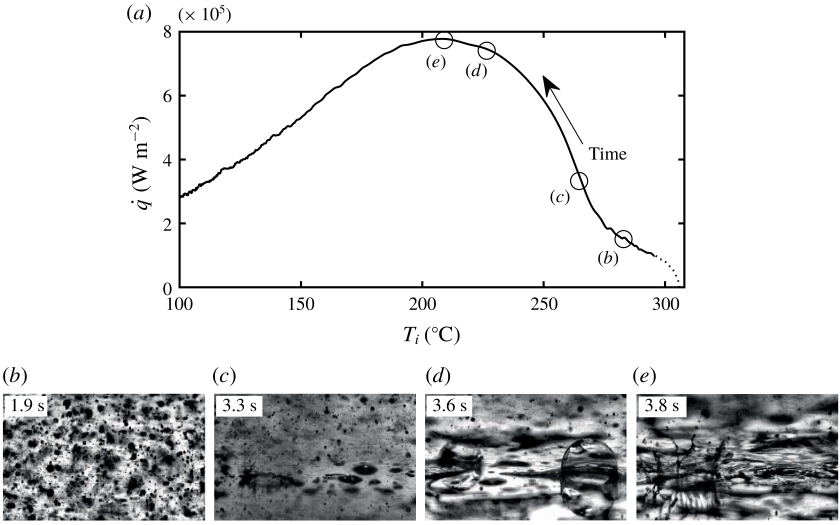

Figure 2.9: Phenomena of spray impact regimes at different surface temperatures: (a) Measured heat flux as a function of surface temperature; (b) image of the substrate exposed to spray impact in the film boiling regime; (c) inception of the transition regime at the Leidenfrost point; (d) image corresponding to the fast expansion of the wetted area; (e) apparently completely wetted surface at the instant corresponding to the critical heat flux. (Reprinted from Tenzer et al. (2019), with permission of the Cambridge University Press. © 2019 Cambridge University Press.)

When the Leidenfrost point is reached, further cooling leads to a rapid increase in heat flux caused by partial wetting of the surface. The change in surface temperature as a function of heat flux is shown in Fig. 2.9, with the phenomena occurring on the substrate shown. The spray parameters for the mentioned case were: mean drop diameter $D_{10} = 43\,\mu\text{m}$, mean velocity $U = 10$ m/s, and mass flux $\dot{m} = 0.90$ kg/m^{2}s.

Namely, after the film boiling regime (exemplarily shown in Fig. 2.9b) and reaching the Leidenfrost point, the area of wetted spots on the substrate grows rapidly, favored by the decreasing surface temperature. The duration of this transitional spray cooling regime is rather short. During this period, two different drop impact scenarios can be observed: drop impact on dry

regions in the film boiling regime and drop impact on wetted patches. For the spray cooling case in Tenzer et al. (2019), a very short time of slightly more than one second is reported between Leidenfrost point and CHF, making it almost impossible to predict the surface temperature and heat flux in the transition boiling regime or at the critical heat flux. This short time in the transition boiling regime is very small compared to the overall cooling process and therefore does not play a significant role in the cooling process. Keeping this short time in mind, Tenzer et al. (2019) propose replacing the transition boiling regime by a jump of the heat flux towards a very high value, starting at the Leidenfrost point. The physics of the transition from film boiling to nucleate boiling after reaching the Leidenfrost point is not yet fully understood, resulting in the inability to reliably predict the Leidenfrost temperature and heat flux values in the transition boiling regime. This topic still requires a lot of attention and a modeling development is expected in the coming years. Furthermore, the acquisition of an accurate and complete set of Leidenfrost temperatures as a function of different fluids and substrates could further enhance the state of research in this area.

After reaching the CHF, the nucleate boiling regime is established, as illustrated exemplarily in Fig. 2.9(e). Tenzer et al. (2019) proposed a modeling approach as a remote asymptotic solution for the heat flux in nucleate boiling, initially developed for the stainless steel target; however, other target materials are also considered. The assumptions underlying the model are presented below, followed by the formulation.

For longer times $t > t_\mathrm{L}$, during the nucleate boiling regime of spray cooling, the heat flux can be estimated from Eq. (2.31), taking into account the very short duration of the transient boiling regime and the very high time derivation of the temperature during this regime. Let ΔT_L be the temperature jump during the transition boiling. In this case Eq. (2.31) yields

$$\dot{q}(t) = \frac{e_\mathrm{w}}{\sqrt{\pi}} \int_0^{t_\mathrm{L}} \frac{T'_{\mathrm{i,film}}(\tau)}{\sqrt{t-\tau}} d\tau + \frac{e_\mathrm{w}}{\sqrt{\pi}} \frac{\Delta T_\mathrm{L}}{\sqrt{t-t_\mathrm{L}}} - \frac{e_\mathrm{w}}{\sqrt{\pi}} \int_{t_\mathrm{L}}^{t} \frac{T'_{\mathrm{i,nucleate}}(\tau)}{\sqrt{t-\tau}} d\tau. \quad (2.36)$$

On the right-hand side of Eq. (2.36), the first term is associated with the thermal evolution during the film boiling regime, the second term is associated with the temperature jump ΔT_L during the transitional regime at $\tau = t_\mathrm{L}$, and the last term is based on the temperature evolution during nucleate boiling at times $t_\mathrm{L} < \tau < t$. To model the heat flux in the nucleate boiling regime,

the values of ΔT_L and the evolution of the surface temperature $T_\mathrm{i}(\tau)$ (which is needed to calculate the time derivative $T_\mathrm{i}^{'}(\tau)$) are required.

When estimating an upper bound for the heat flux during the nucleate boiling regime of single drop impact, the temperature at the wetted part of the wall interface is approximated by the saturation temperature T_sat (Breitenbach et al., 2017a). As mentioned in Section 2.2.1, the nucleate boiling regime is characterized by intense nucleation and expansion of vapor bubbles. The temperature near the contact line of each expanding bubble is close to the saturation temperature. However, some overheating of the surrounding liquid is required for bubble growth. The heat transfer in the liquid phase during nucleate boiling is governed by convection in the liquid flow between the bubbles. The heat mainly goes into vaporization at the bubble interfaces where $T = T_\mathrm{sat}$. Therefore, the upper bound for the heat flux during nucleate boiling can be estimated by assuming that the temperature at the wetted wall interface is T_sat.

In the described study (Tenzer et al., 2019), the upper bound for the heat flux $\dot{q}$ during spray cooling is also estimated, as in the case of a single drop impact, under the assumption that the substrate temperature is equal to the saturation temperature at $t > t_\mathrm{L}$. The third term on the right-hand side of the Eq. (2.36), associated with the time gradient of the surface temperature at $t > t_\mathrm{L}$, can be neglected compared to the effect of the temperature jump at the Leidenfrost point. The temperature jump during the transition boiling regime can be estimated as $\Delta T_\mathrm{L} = T_\mathrm{iL} - T_\mathrm{sat}$. The heat flux can be obtained from Eq. (2.36), neglecting the value of the last term, in the form:

$$\dot{q}(t) = \frac{e_\mathrm{w}}{\sqrt{\pi}} \frac{T_\mathrm{w0} - T_\mathrm{sat}}{\sqrt{t - t_\mathrm{L}}} - S e_\mathrm{w} \frac{T_\mathrm{w0} - T_\mathrm{sat}}{2} \sum_{i=1}^{\infty} a_i i B^* \left[\frac{\xi_\mathrm{L}}{\xi}, \frac{i}{2}, \frac{1}{2} \xi^{\frac{i-1}{2}} \right], \quad (2.37)$$

where $B^* \left[\cdot; \cdot, \cdot \right]$ is the incomplete beta function, used to compute the probability for a range of values in a beta distribution and $\xi = t \pi S^2$. The Eq. (2.37) is only valid for very fast substrate cooling, when the time interval between the Leidenfrost point and the point corresponding to the critical heat flux is very short. With further modification and at large times, $t >> t_\mathrm{L}$, the

remote asymptotic solution is approached, leading to:

$$\mathcal{T} \equiv k \frac{e_{\mathrm{w}}^2 \Delta T^2}{\pi \dot{q}(t)} \approx t - t_{\mathrm{L}}, \tag{2.38}$$

where k is a constant that can be determined from experiments and ΔT represents the difference between the initial wall temperature T_{w0} and the saturation temperature of the liquid T_{sat}. The model sublimed in (2.38) has been validated for different spray parameters and different substrate initial temperatures, with the term $\mathcal{T}$ very close to the time step $t - t_{\mathrm{L}}$ in all experiments (Tenzer et al., 2019). Excellent agreement between the theoretical prediction and the experimental data was found over a wide range of spray parameters for stainless steel. Good agreement was also found for nickel and hot work steel. Note, however, that the measured values for $\mathcal{T}$ deviated significantly from the theoretical predictions at small times associated with the film boiling and transition regimes, for which the scaling Eq. (2.38) is not applicable.

Experiments performed by Tenzer et al. (2019) show that the heat flux in the fully developed nucleate boiling regime depends significantly on time. This heat flux is estimated as

$$\dot{q}(t) \approx \frac{e_{\mathrm{w}}}{\sqrt{\pi}} \frac{T_{\mathrm{w0}} - T_{\mathrm{sat}}}{\sqrt{t - t_{\mathrm{L}}}}. \tag{2.39}$$

Lastly, it is important to note that the remote asymptotic solution is only valid for a semi-infinite hot substrate and a uniform spray. In practical terms, this means that the thickness and width of the substrate are larger than the thickness of the thermal boundary layer in the substrate.

2.3 Drop and spray impact of rheologically complex liquids

Besides pure water as a medium, this thesis considers complex liquids. Therefore, an brief introduction in the characteristics of such liquids is given. The broad field of rheology studies the flow properties of complex liquids, including polymer solutions and melts, as well as colloidal dispersions and various other

suspensions. Such liquids are generally non-Newtonian, *i.e.* the relation between stress and strain rate is non-linear. In particular, Bingham fluids flow only at a threshold level of applied stress, which is referred to as yield stress. Suspensions often exhibit thixotropy, *i.e.* a decrease in viscosity at higher flow rates, also referred to as "shear thinning" (Barrat & Hansen, 2003). A well-known practical example is the reduction in viscosity of paints by brushing. Despite its obvious technological importance, the rheological behavior of complex liquids is not discussed further in this work, except for a review of the state of the art for the liquids used in the present thesis - suspensions and solutions.

In principle, **suspensions** are highly heterogeneous two-phase (or multi-phase) systems. When referring to suspensions, one speaks of a dispersed phase, which can vary in size, and a continuous medium in which the dispersed phase is distributed. There are a few different definitions in the literature (Barrat & Hansen, 2003; Rahman & Asiri, 2016), but most of them conclude that suspensions are a subcategory of disperse systems with particles larger than 1 µm. However, Ness et al. (2022) state that for dense suspensions the particles can be rigid solids of any shape with crystalline or amorphous structure, such as graphite, with sizes between 100 nm and 1 mm. Suspensions are referred to as flocculated suspensions when they exhibit a pronounced aggregation tendency. For flocculated suspensions, shear thinning has been observed at high stirring rates (Mills, 1985; Goodwin & Reynolds, 1998). For smaller particles typically in the range of nanometers, mixtures of solid and continous phase are usually termed as collodial dispersions or collodial suspensions, according to Barrat & Hansen (2003). It is important to note that particles in both suspensions and colloidal dispersions usually have a size distribution, *i.e.* they are polydisperse (Barrat & Hansen, 2003). Early work by Mewis (1996) dealt with the flow behavior of concentrated suspensions, predicting the behavior of large particles as well as fine, colloidal particles. In the aforementioned work, the various parameters that influence the flow behavior are systematically reviewed. More recently, the flow behavior of different dispersions of nanometer-sized functionalized graphene in different mixtures has been studied, with Newtonian behavior observed over the over the range of concentration, temperature and shear rate analyzed (Vallejo et al., 2018). Although there is not a very strict size limit for the distinction, it is important to be consistent in the use of the term "suspension" or "dispersion".

Solutions, on the other hand, are defined as a mixture of two or more miscible substances that can dissolve in each other (these two components of the solution can be in any of the most common states of matter: solid, liquid, and gas), as mentioned in the foundational works of Kirkwood (1935, 1936). As such, a liquid solution is a homogeneous mixture consisting of a solute dissolved in a solvent, in most cases water.

2.3.1 Isothermal cases

Most of the research related to the study of complex liquid dynamics considered the drop and spray impacts on a heated substrate, as this is an industrially relevant topic to investigate. Recently, however, there have also been many studies that have investigated drop/spray impacts on dry, non-heated, substrates with complex liquids. For example, particle transport in an evaporating binary droplet on a cleaned glass substrate was studied by Thayyil Raju et al. (2022). The aforementioned study showed that the accumulation of particles occurs not only at the contact line (due to the coffee-ring effect) or at the solid substrate (due to sedimentation), but also at a specific radial position near the liquid-air interface, forming a ”ring” referred to as the Marangoni ring. However, the formation of this ring is mainly attributed to the solutal Marangoni flow induced by the evaporation dynamics of the water-glycerol droplet used in the study. On the other hand, the mechanism by which the particles in a drying film come into close proximity during solvent (liquid) evaporation plays an important role in the morphology of the resulting film on the surface. This has been investigated numerically by Trueman et al. (2012a). The study has also been carried out experimentally by analyzing the distribution of particles normal to the substrate, where particle concentrations at different positions in the film are determined by atomic force microscopy (Trueman et al., 2012b).

When discussing particle distribution and accumulation, it should be pointed out that the process of particle accumulation can be influenced by particle diffusion. In case of a drop on a heated substrate, the process of particle accumulation is also influenced by the propagation of the bubble interface in the liquid region due to evaporation (Gajevic Joksimovic et al., 2023c). Two main values characterize the dynamics of the particles suspended in the liquid.

One is the Stokes number, defined as

$$\mathrm{Stk} = \frac{\rho_\mathrm{p} d_\mathrm{p}^2 U_0}{18 \mu d_0}. \tag{2.40}$$

A small Stokes number, $\mathrm{Stk} \ll 1$ indicates that the particles in the suspension mainly follow the streamlines of the liquid flow. The next dimensionless number that indicates the importance of particle diffusion is the Péclet number

$$\mathrm{Pe} = \frac{d_0 U_0}{D_s}, \quad D_s \sim \frac{k_B T}{3\pi \mu d_\mathrm{p}}, \tag{2.41}$$

where D_s is the diffusion coefficient of the suspension, k_B is the Boltzmann constant, T is the temperature. The subscript "p" corresponds to the particles. In Eq. (2.41), the Einstein equation is used for the estimation of the diffusion coefficient (Einstein, 1908; Kholodenko & Douglas, 1995). Large Péclet numbers correspond to suspension flows in which the effect of diffusion is negligibly small.

Correspondingly, in the cases $\mathrm{Stk} \ll 1$ and $\mathrm{Pe} \gg 1$, particle accumulation leads to the formation of a crust. Such crusts are often observed after drying a suspension drop (Maenosono et al., 1999; Yarin et al., 2002; Mezhericher et al., 2010; Fu et al., 2012). Recently, Mondal et al. (2023) provided a comprehensive review of the physics of drying of complex liquid drops with emphasis on flow field and pattern formation as well as the description of physical processes. Specific considerations include the drying induced effects observed during sessile drop drying such as the diffusion of liquid molecules into the surrounding atmosphere and the movement of dispersed phase by evaporation driven flow.

2.3.2 Influence of additives on heat transfer regimes

In some cases, the presence of an additional phase in a liquid drop can lead to a significant change in the drop outcome. As shown in Sijia et al. (2019); Lyu et al. (2021), the presence of small impurities or gasification of the liquid can lead to micro-explosions in the drop as the drop spreads on a hot substrate.

In general, the mechanisms of boiling in a suspension/solution drop are completely different, which will be considered in detail in this thesis. In order

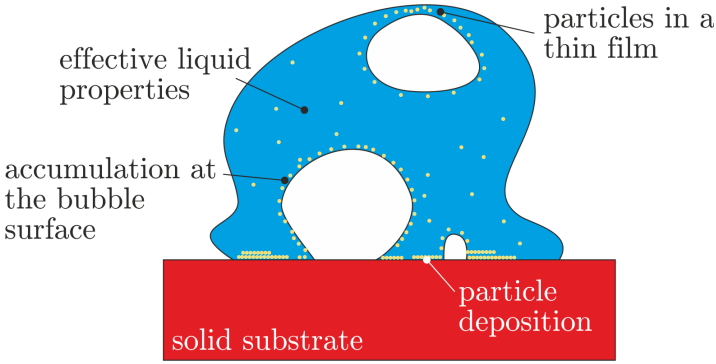

Figure 2.10: Sketch of the assumed phenomena associated with the particulate phase in a suspension drop on a hot substrate, which potentially influence the thermodynamic and hydrodynamic phenomena in the drop.

to study the drop and spray impact of suspensions/solutions on a hot substrate, it is important to determine possible mechanisms and factors influencing the thermodynamic and hydrodynamic phenomena accompanying the impact of such a complex drop on a heated substrate. Among these factors are:

- change of the effective thermodynamic and mechanical properties of the liquid;
- the formation of a deposited layer of dispersed/dissolved phase;

In the case of suspensions, the following mechanisms are also involved:

- accumulation of particles at the surface of the expanding bubble;
- dynamic effects of particles influencing bubble stability, accumulation in thin films and their breakup.

These phenomena, for the rather complex case of **a suspension drop**, are shown schematically in Fig. 2.10 (Gajevic Joksimovic et al., 2023c). The effects of the effective thermal and material properties of the complex liquids do not explicitly lead to new physical phenomena. However, depending on the volume concentration, the presence of particles can lead to a significant changes in liquid viscosity, surface tension, thermal diffusivity and conductivity, as well as other relevant thermal properties. Consequently, the liquid properties need

to be measured for different suspensions, *i.e.* different concentrations of the solid phase. While the dependence of the suspension behavior on particle volume concentration was found to be significant in this study, the addition of lubricants containing a dispersed/dissolved phase to pure water, resulting in lubricant suspensions and solutions, did not significantly alter these properties in the cases considered in this study.

As illustrated in Fig. 2.10, a deposited solid layer is formed on the wetted part of the substrate due to local liquid evaporation leading to accretion of the particulate phase from the suspension. At wall temperatures not exceeding the drop boiling limit, deposition occurs mainly near the receding contact line as the drop slowly evaporates, leading to the formation of *coffee-stain* patterns (Deegan et al., 1997; Marin et al., 2011; Eral et al., 2011). At higher temperatures, corresponding to the nucleate boiling regime, the contact lines are formed by each of the multiple vapor bubbles and the particles, which are also deposited randomly on the substrate (see Fig. 2.10). The deposited layer can potentially affect the heat transfer, as analyzed in Section 5.1.2. Particles can also accumulate on the surfaces of expanding vapor bubbles. When the bubble height is comparable to the drop height, particles are collected in a thin liquid film that becomes thinner as the bubble continues to expand. The breakup of these films leads to a splash characterized by the formation of small secondary drops, which is discussed in detail in Sections 5.1.1 and 5.1.2. Moreover, the presence of the particles can significantly affect the dynamics of the thin liquid films, especially when the film thickness is similar to the particle size. In many cases, the presence of the particles initiates early film breakup, resulting in larger drops but less intense splash. These well-known phenomena govern the principle of the antifoam properties of some suspensions (Frye & Berg, 1989; Aveyard & Clint, 1995; Garrett, 2016).

On the other hand, the mechanism of formation of a deposited solid layer during the impact of **a solution drop** is quite similar to the one described above. Here it leads to the accretion of the dissolved phase from the solution, resulting in the formation of coffee-stain patterns, introduced previosly in this section. The influence of this deposited layer on the heat transfer is addressed in Section 8.2. In the case considered in this thesis, the dissolved phase refers to organic salts that are completely dissolved in water. Properties of the used liquids are given in Section 3.2. There are quite a few studies that examined the influence of the dissolution of different types of organic salts in the bulk

liquid on the heat transfer (Abdalrahman et al., 2014; Cheng et al., 2013). For example, Mohapatra et al. (2014) have found that the heat flux at the surface of the hot metal substrates at 900 °C is significantly increased by the addition of the dissolved salts in the water used for cooling. The use of salt water for spray cooling produces a higher heat removal rate due to the dominance of the salt deposition phenomenon (Pati et al., 2017). Even at relatively low temperatures for spray cooling, at 240 °C, the addition of salts reduced the cooling time by an order of magnitude, as discussed in Cui et al. (2003). In addition, salt solutions were found to increase the known Leidenfrost point (Kumar et al., 2020; Huang & Carey, 2007).

For stabilization of suspensions and solutions, organic and inorganic components (surfactants and binders) are often also present in the liquids. The exact composition of the liquids used in this study is given in Section 3.2. There are a number of studies that examine the exact influence of surfactants added to water drops/spray in means of heat transfer. Namely, in study of Singh & Kukreja (2021), an optimal concentration of surfactants has been experimentally determined for sprays at temperatures below the boiling point. It is known that at higher wall temperatures the addition of surfactants can significantly influence the boiling phenomena, causing foaming in the near-wall region and thus enhancing spray cooling performance (Qiao & Chandra, 1998; Zhang et al., 2018; Ravikumar et al., 2014a; Bandaru et al., 2013; Liu et al., 2021; Chakraborty et al., 2019). In addition, surfactants can potentially cause the delay of the Leidenfrost point as already reported by several authors (Cai et al., 2022; V V S Vara Prasad et al., 2022).

The heat flux can be also increased by adding a certain amount of a polymer (Ravikumar et al., 2014b; Sarkar et al., 2016). An optimum polymer concentration for maximum heat flux can be determined experimentally. Emulsions can also be useful for metal quenching when the formation of a solid deposited layer is undesirable. Experiments show that the use of emulsions as cooling liquids can potentially affect the heat flux. In Pati et al. (2018) it was shown that the heat flux provided by an oil-in-water emulsion is lower than that of pure water at the same temperatures, while the use of kerosene-based emulsions improves cooling during the quenching process. It is interesting to note that the use of oil-in-water emulsion for jet cooling results in a significant cooling enhancement compared to pure water jet (Gradeck et al., 2011).

Among the other fluids that can potentially improve spray cooling are nanofluids, which are colloidal suspensions containing nanometer-sized particles (Duursma et al., 2009; Sanches et al., 2021; Aksoy et al., 2020).

3 Experimental approach of this study

This chapter provides a brief overview of the experimental methods used throughout the experimental campaign, as well as the preparation and properties of the lubricant suspensions and solutions, used in the experiments. However, a more comprehensive analysis of the experimental methods is presented in Sections 4.1 and 7.1. Certain parts of the following sections have been published in Gajevic Joksimovic et al. (2023a,c).

3.1 Experimental systems for drops and sprays

Two configurations of the experimental setup are used in this study, as shown schematically in Fig. 3.1. The first configuration, shown in Fig. 3.1a, is used for a single drop impact study, aimed at the identification of the main thermodynamic and hydrodynamic phenomena of a single drop impacting onto a heated surface using high-speed imaging. The setup was later on adapted for both side-view and bottom-view imaging, as discussed in Section 4.1. The second configuration, shown in Fig. 3.1b, is designed for the high-resolution measurements of the interface temperature and distribution of the heat flux. It is used for spray impact and spray cooling measurements.

A simplified, schematic representation of the single drop setup, for observing and characterizing of a single drop impact is shown in Fig. 3.1a:, comprising a *heating system* with a temperature controller and a replaceable impact surface; the *drop generation system*; an *observation system* with a high-speed camera with LED illumination and diffuser plate; and a *computer unit* for data acquisition and control of the experimental flow.

Fig. 3.1b illustrates a simplified scheme of an experimental setup for observing and characterizing heat transfer by spray impact on a heated substrate. It consists of four main systems, comprising a *spray generation system* connected to a fluid supply, a *heating system* with temperature measurement and control, an *observation system* consisting of a high-speed camera and

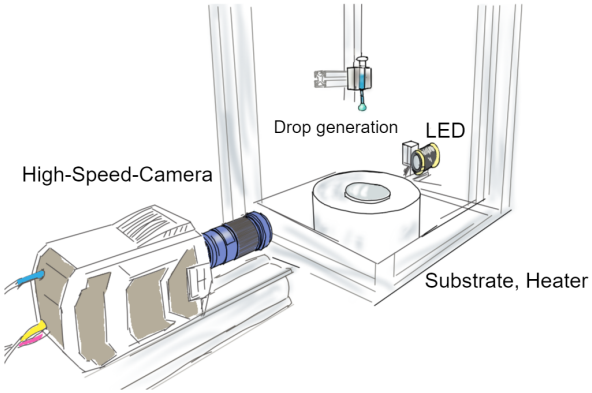

(a) Single drop setup.

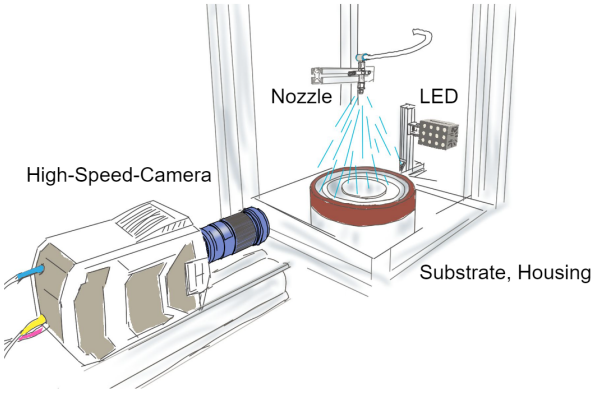

(b) Spray cooling setup.

Figure 3.1: Schematic representation of experimental facilities.

backlight illumination, and a *computer control unit* for data acquisition and control of the experimental flow in LabVIEW software.

3.2 Preparations of the suspensions and solutions and their properties

As a base for the preparation of the **lubricant suspensions**, the industrial lubricant LUBRODAL F105 (Lubritech, 2022a) is used, produced by the company **Fuchs Lubritech GmbH**. This lubricant is a water-miscible, water-based graphite dispersion, supplied as a concentrate. In the industry, it is mainly used for cooling and lubrication during hot forging and various forming operations. It contains solid particles of layered graphite with sizes ranging from 5 µm to 20 µm in diameter. The graphite particles have a lubricating role due to layered structure, which allows lubrication by interchange of particle layers. Additional components, organic and inorganic additives (with the role of surfactants and binders) in the lubricant concentrate stabilize the lubricant, preventing agglomeration of particles and aiding the spreading and formation of adherent lubricant films on the die surfaces. The exact composition of the aforementioned additives is proprietary. However, the organic components present in the lubricant concentrate and publicly listed in the data sheet are: silicic acid, sodium salt 1.00 % - <5.00 %, morpholin derivative 0.10 % - <0.60 %, and pyrithione, sodium salt 0.001 % - <1.00 %; all concentrations are in percent by weight (Lubritech, 2022a). The concentration of all additives does not exceed 5 %. Although the lubricant itself can be described as a non-Newtonian fluid that would exhibit shear thinning at high stirring rates (Mills, 1985; Goodwin & Reynolds, 1998), when the lubricant is mixed with water, the relationship between stress and strain rate is very close to the linear one for water, which allows the suspensions used in this study to be considered as Newtonian fluids. This information has been confirmed by the lubricant manufacturer.

After diluting the lubricant with water, the concentration of additives decreases further along with the binding agents, leaving the solid graphite particles as a dominant influencing factor. Suspensions of different volumetric particle concentrations are prepared by mixing the lubricant concentrate with distilled water. In this study, the volumetric concentrations of the suspensions

range from $\varphi = 1.43\,\%$ to $\varphi = 4.3\,\%$. In most industrial applications, the maximum solid particle concentration of $\varphi = 4.3\,\%$ is the upper limit. The lower limit $\varphi = 1.43\,\%$ in this study corresponds to the smallest ratio of the solid particles at which some effects of the particles on the drop impact dynamics have been identified. Since the concentration of the solid particles is small, it is expected that most of the thermal properties are similar to that of water. The boiling temperature of the suspensions is measured, yielding $T_{\mathrm{sat}} = 100\,^{\circ}\mathrm{C}$. The viscosity of a dilute suspension can be estimated using the approximation of Batchelor & Green (1972), which generalizes the well known Einstein formula (Einstein, 1906)

$$\frac{\mu}{\mu_{\mathrm{water}}} = 1 + \frac{5}{2}\varphi + 5.2\varphi^2. \tag{3.1}$$

This estimation yields a maximum increase of the effective viscosity of approximately 12% for the suspensions with the highest concentrations considered in this study. The surface tension of the different suspensions was measured at room temperature using a tensiometer, resulting in $\sigma = 71.19$ mN/m for $\varphi = 1.43\,\%$, $\sigma = 70.48$ mN/m for $\varphi = 2.57\,\%$, and $\sigma = 68.88$ mN/m for $\varphi = 4.3\,\%$. It was found that the surface tension depends slightly on the suspension concentration.

The effect of the solid particles on the viscosity of the suspension can also be represented in terms of the Ohnesorge number:

$$\mathrm{Oh} = \frac{\mu}{\sqrt{\rho\sigma d_0}}. \tag{3.2}$$

The value of the Ohnesorge number for the suspension with the highest concentration is 2.84×10^{-3}, which is approximately 12% higher than the value for distilled water. Nevertheless, this value is much smaller than unity.

In the case of **lubricant solutions**, the industrial lubricant LUBRODAL F327 (Lubritech, 2022b) is used as a base for the preparation. The lubricant LUBRODAL F327 represents a water-based, water-miscible die lubricant with excellent separation effects for hot and warm forging of steel. It is widely used for different forging operations in the industry due to the quick formation of a visible and touch-resistant lubrication film after spraying onto the hot tool surfaces, thus achieving good wetting and reducing the friction between tools and working parts.

The lubricant is supplied as a concentrate, containing a specific amount of organic salts that provide lubrication when utilized. These salts are completely dissolved in water. Similar to the graphite lubricant mentioned above, this lubricant concentrate also contains additional components, organic and inorganic additives (with the role of surfactants and binders) to stabilize the concentrate and promote the spreading and formation of adherent lubricant films on the die surfaces. The exact composition of the above mentioned additives is proprietary, as is the chemical composition of the organic salts. The data sheet (Lubritech, 2022b) publicly lists the organic components present in the lubricant concentrate as: isothiazolone derivative 0.002 % - < 0.01 %. Concentration is given in percent by weight. The concentration of all additives does not exceed 5 %.

Prior to the experiments in the spraying setup, the lubricant is diluted with distilled water to the desired ratio, further lowering the concentration of additives to a maximum concentration of 2.5 %, leaving dissolved organic salts as the primary influencing factor. Standard values for the dilution ratio of LUBRODAL F327 with water range from 1:1 for very difficult forging operations to 1:40 for simpler forging operations. The 1:1 dilution ratio was not applied in the present experimental campaign due to the spraying difficulties of such a dense solution. Depending on the specific operating conditions and intended outcome, dilution ratios from 1:2 to 1:20 are the most common in the forging industry today. For this reason, dilution ratios from 1:2 to 1:16 were used in the spray experimental campaign, while ratios from 1:4 to 1:10 were tested in the single drop campaign. Solutions of different salt volume concentrations are prepared by mixing the lubricant concentrate with distilled water. In this study, the volumetric concentrations of the solutions range from $\varphi = 0.97\,\%$ to $\varphi = 5.47\,\%$. Spray experiments were conducted with 8 different lubricant-water mixture ratios to achieve different volumetric concentrations. In most industrial applications, the maximum volumetric concentration of $\varphi = 8.2\,\%$ is typically the upper limit, which is rarely achieved due to spraying difficulties. Since the concentration of organic salts is low, most of the thermal properties are expected to be similar to water. The boiling temperature of the lubricant solution is measured for a few mixture ratios, resulting in a boiling temperature of $T_{\mathrm{sat}} = 100\,°\mathrm{C}$. The surface tension of the different solutions was measured with a tensiometer, resulting in $\sigma = 58.95$ mN/m for $\varphi = 5.47\,\%$, $\sigma = 61.63$ mN/m for $\varphi = 2.34\,\%$ and $\sigma = 64.28$ mN/m for

$\varphi = 1.49\,\%$.

Given that the effects of the additives on the main thermal properties of the solutions and suspensions in these experiments are small, one might expect that the outcome of the single drop and spray impact would also be similar to that of pure water. However, in this study it is demonstrated that the presence of solid graphite particles in the case of suspensions, and salts and surfactants in the case of solutions, can cause significant changes in the dynamics of single drop/spray impact, boiling and therefore the values of heat flux, as shown in Part I and Part II.

Part I

Single drop impact of a suspension/solution drop

4 Experimental methods for investigating single drop impact

This chapter outlines the experimental methods utilized for studying drop impact. In Section 4.1 different configurations of the experimental setup are described in detail. Section 4.2 concentrates specifically on the measurement techniques employed for drop characterization. Certain parts of the subsequent sections, including text and figures, have been previously published in Gajevic Joksimovic et al. (2023c).

4.1 Configurations of the experimental setup

Two experimental setups have been developed to study and analyze the impact of single drops on a hot surface. The first configuration, used for the main experiments involving the impact of suspension/solution drops onto a hot metal substrate, employs a side camera position that observes and captures all drop impact-related phenomena. In order to visualize bubble formation as well as the formation of a solid deposit after a drop impact, a second configuration of the initial setup was designed with transparent heated substrate, enabling a bottom view of the aforementioned phenomena.

Figure 4.1 depicts a schematic representation of two configurations of the single drop experimental setup - side and bottom-view. Both configurations are composed of four primary subsystems: an observation system equipped with LED back-side illumination, a heating system with temperature control, a drop generation system, and a computer unit responsible for controlling the experimental flow and data acquisition.

The two setup configurations differ in the central part of the construction. In the side-view setup, a high-speed camera provides a lateral perspective of the falling drop (denoted as 4 in Fig. 4.1). The heating system in this setup configuration consists of a metal target and a heater, ensuring a temperature

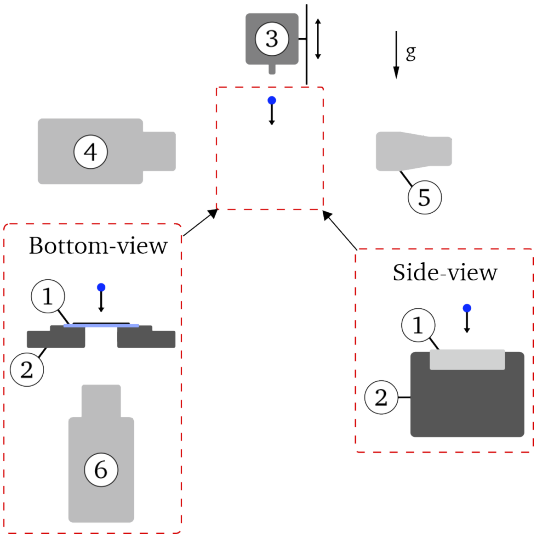

Figure 4.1: The schematic representation of the two configurations of single drop experimental setup with highlighted differences in the central part of the construction for side-view and bottom-view setup, respectively.

control during the experiment. On the other hand, the bottom-view setup includes a transparent sapphire target and a corresponding heating system. The use of a transparent target allows the bottom view camera (marked as 6 in Fig. 4.1) to capture relevant phenomena from beneath. These two setup configurations provide complementary views and enable comprehensive analysis of the drop impact dynamics from different angles. The following sections provide a more comprehensive explanation of each subsystem.

4.1.1 Side-view system

The side-view experimental setup is designed to observe and characterize the impact of a single drop onto a heated surface. A schematic representation of the setup is shown in Fig. 4.2a, comprising a *heating system* with a temperature controller (2) and a replaceable impact surface (1); the *drop generation system* (3); an *observation system* (4) with a high-speed camera with LED illumination and diffuser plate; and a *computer unit* (5) for data acquisition and control of

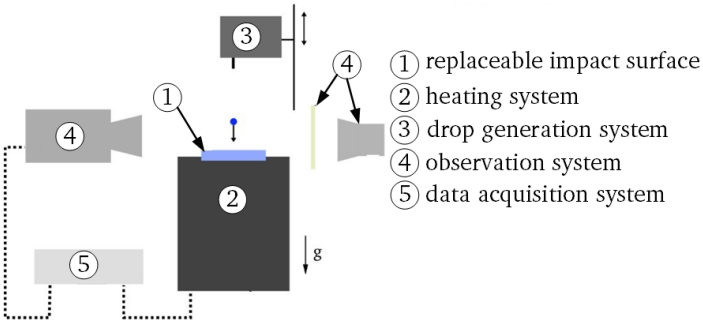

(a) Schematic representation of the experimental installation.

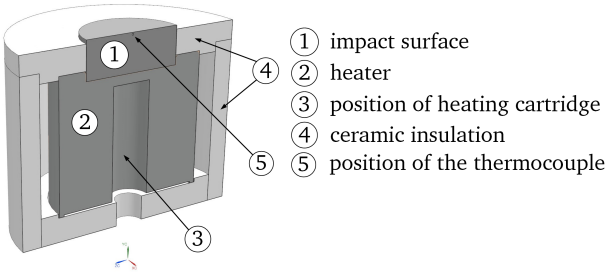

(b) Sectional view of the heating system.

Figure 4.2: Schematic representation of the side-view experimental setup configuration.

the experimental flow.

The heating system consists of a replaceable impact target and a heated aluminum cylinder, as indicated in Fig. 4.2b. The impact target is a stainless steel (type 1.4841) cylinder with a diameter of 50.8 mm and height of 20 mm. The impact surface of the target is mirror polished, with an average roughness of 0.05 µm. The impact target is embedded in a heated coaxial aluminum cylinder, equipped with a 315 W cartridge heater (*hotset hotrod HHP*) to achieve the desired temperature of the impact surface. Additionally, ceramic insulation material (*CC Ceramic Components C610*) is used to insulate the side walls.

The temperature of the stainless steel impact surface is controlled by a PID thermo-controller (*HOTSET c448*), in conjunction with with a type-J thermocouple (*TMH class 1*) placed 0.5 mm below the upper surface. A more detailed sectional view of the heating system can be seen in Fig. 4.2b. During experiments, the surface was repeatedly heated up to 420 °C. Given the high thermal conductivity of the target material, the temperature difference between the thermocouple and the impact surface can be neglected and the surface temperature can be approximated to be equal to the substrate temperature measured by the thermocouple.

Drops are generated with a syringe pump (*World Precision Instruments*) and a blunt hypodermic needle (*Braun Sterican, gauge 27*). The position of the needle can be changed above the impact surface using a linear stage (*Isel c142 - 4*), thus achieving different impact velocities of the falling drops. In the experiments, impact velocities $U_0 = 0.5 - 1.7$ m/s are realized. Impact velocity deviated by a maximum of ± 0.05 m/s under identical experimental conditions for repeated experiments. The syringe pump was chosen for drop generation because it offers quick replacement of pipes and syringes, which is often necessary due to the complexity of the liquids used. The desired diameter of the drop can be selected by the displacement of the syringe, resulting in drops ranging from 2.1 mm to 2.3 mm in diameter (d_0). Under identical experimental conditions for repeated experiments, the initial drop diameter deviated by a maximum of ± 0.05 mm.

A CMOS high-speed camera (*Vision Research Phantom V12.1*), with a maximum resolution of 1280×800 pixels at 6242 fps, is used to record side-view images and videos of the drop impact. Alternatively, a second high-speed camera is used in the experimental setup (*Vision Research Phantom v2012*). The high-speed camera is additionally equipped with a 60 mm macro lens (*Nikon AF NIKKOR 1:2.8 D*) and spacer rings (*Nikon PK*).

An LED spotlight (*Veritas miniConstellation 120C28*) with a power of 120 W is used for illumination. The illumination is placed behind the drop and directed co-linear with the high-speed camera, resulting in shadowgraphy imaging. A diffuser plate with a diffusion angle of 30° is placed between the LED illumination and the impact zone of the drop in order to achieve more uniform illumination of the falling drop.

Experimental procedure

Experimental procedure for each experiment is briefly described below.

First, the impact target is heated to the desired temperature, with the temperature of the stainless steel impact surface controlled by a PID thermo controller. Subsequently, the needle is positioned above the impact surface through the use of a linear stage, thereby achieving the desired impact velocity of the falling drop. Next, the syringe pump is set to a flow rate of 1 ml/min, pumping a volume of 5.5 µl to 5.7 µl in one displacement of the syringe. The start of the experiment is indicated by the detachment of the droplet from the needle due to gravity. When a droplet approaches the target, the camera's image-based auto-trigger activates, recording and capturing video from the moment the drop collides with the hot substrate until it fully evaporates, disintegrates, or rebounds, based on the thermodynamic regime of the event.

After the experiment, in the case of suspension/solution drops, a solid layer of dispersed/dissolved phase is deposited after each drop impact. Therefore, in order to investigate a drop impact onto a clean substrate, the deposited layer was removed prior to each individual single drop impact experiment thus achieving a good repeatability of the experiments. Removal of the deposited layer was achieved using the following steps. Firstly, the surface was cleaned with distilled water. Afterwards, it was polished with a mirror polishing paste to achieve the desired average roughness of 0.05 µm for the impact surface, determined by atomic force microscopy. Subsequently, the target was cleaned with isopropanol alcohol to remove polish residue.

4.1.2 Bottom-view system

The bottom-view system is intended to provide a more comprehensive understanding of the phenomena that occur during the boiling of the suspension/solution drop onto the hot substrate. The decision to adopt this design was driven by the inability of observing all the associated phenomena solely from a side-view perspective. These phenomena include, for example, the movement of contact lines during boiling and the formation of a solid deposit. As mentioned earlier in the current section, both setups exhibit variations in the central part of the construction, encompassing different heating systems and, in the case of a bottom-view configuration, the addition of an extra

observation system. Consequently, the details of the other systems will not be elaborated upon, considering that they are identical to those of the side-view setup. Fig. 4.3 shows a schematic of all the components in the bottom-view setup.

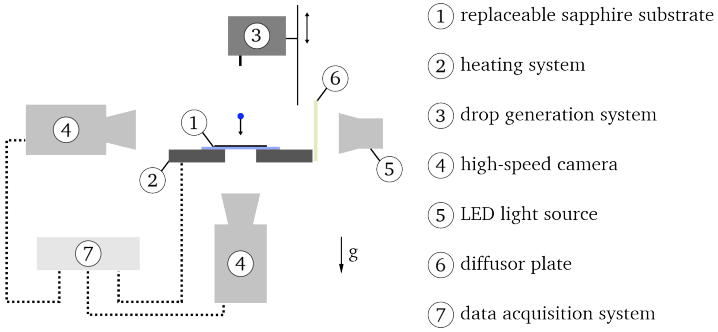

Figure 4.3: The schematic representation of the bottom-view setup configuration.

In order to obtain a bottom view of the impact process, the heating system employed consists of a 3 mm thick transparent sapphire substrate with a diameter of 70 mm (*Situs Techicals Sapphire*). The surface of the sapphire glass has an average roughness of ≤ 0.5 nm, as stated by the manufacturer. The procedure for cleaning the substrate after each experiment described in Section 4.1.1 also applies to the sapphire substrate, with the exception of the polishing paste (used only on metal substrates).

The substrate is heated by an aluminum ring. Within the aluminum ring, there are a total of eight 120W cartridge heaters (*Hotset Hotrod HHP*) placed circumferentially. Cartridge heaters are placed inside holes with a diameter of 6.5 mm and a depth of 40 mm. The holes are designed as an interference fit in order to achieve a high heat transfer and to protect the cartridges from overheating. A CAD model of the aluminum ring heater is shown in Fig. 4.4. To insulate the lateral surface of the heaters, the aluminum ring is encapsulated in a low conductive ceramic material (*CC Ceramic Components C100*). Furthermore, to ensure the safety of the bottom camera, the entire heater structure was mounted on a plate (*Kelux Kelutherm 800 M*), with a low thermal conductivity value of 0.26 W/mK.

The temperature of the aluminum ring is controlled by a PID thermo-

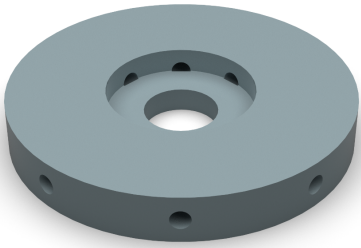

Figure 4.4: CAD model of aluminum ring heater used in bottom-view construction with visible holes representing cartridge heater locations.

controller (*HOTSET c448*), in conjunction with a type-J thermocouple (*TMH class 1*) placed 0.5 mm below the upper surface, immediately underneath the sapphire glass substrate. This heating system allows for the adjustment of the initial surface temperature of the sapphire glass substrate, which can be varied within the range of 50 °C to 350 °C. To ensure the elimination of potential long-term instabilities, the surface temperature of the sapphire glass is repeatedly checked before each measurement using a thermocouple placed on top of the sapphire glass surface.

The bottom-view system, in comparison to the side-view system, is equipped with one more additional observation system containing high-speed camera (*Vision Research Phantom v2012*) which can achieve a maximum resolution of 1280×800 pixels at 22000 fps. It is utilized to capture images and videos of the drop impact from the bottom perspective. The high-speed camera is additionally equipped with a *Sigma* 150 mm macro optical lens. Exemplary images of a boiling drop captured by each camera are compared in Fig. 4.5.

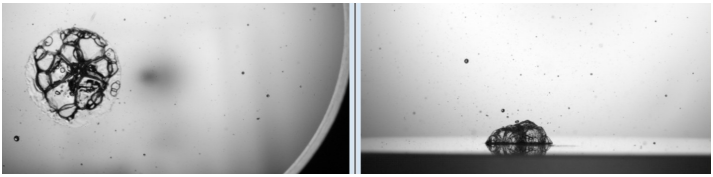

Figure 4.5: Simultaneous bottom and side view of the droplet boiling on a substrate, captured using both cameras in the bottom-view setup. Pure water was used for demonstration with the initial substrate temperature set to 160 °C.

The darker shade adjacent to the drop in the bottom view camera (see Fig. 4.5, left image) indicates the presence of the needle. Consequently, all bottom view images are cropped appropriately to provide a clear visual representation while excluding the needle shadow. Two cameras are synchronized and triggered simultaneously, resulting in videos that capture the impact of a falling drop with precise timing. Parallel with the bottom view camera, the LED illumination with a power of 120W (*Veritas Constellation 120E*) positioned above the falling drop to yield shadowgraphy imaging. To ensure a more uniform illumination, a diffuser plate with a diffusion angle of 30° is placed between the LED spotlight and the point of impact where the drop falls.

Videos captured on a sapphire glass substrate using the bottom-view setup configuration were solely used for qualitative analysis, aimed at observing the phenomena during the drop impact on a hot sapphire glass substrate. On the other hand, videos of the drop impact on a stainless steel substrate using a side-view setup were employed for quantitative analysis and the assessment of heat transfer. This distinction arises from the possibility of different temperature thresholds for various boiling regimes between the sapphire glass and stainless steel substrate. Note that in the later sections, the term "heated substrate" will always refer to the stainless steel substrate in the side-view configuration, while the term "transparent sapphire substrate" will be used when discussing any aspect related to the transparent substrate in the bottom-view configuration.

4.2 Image-based drop characterization

When utilizing a high-speed video system to capture falling droplets, valuable information about drop impact parameters can be obtained through direct imaging. Shadowgraphy imaging, a well-known and straightforward measurement technique (Tropea, 2011), is commonly employed for this purpose and therefore also used in this study. Governing principle of shadowgraphy imaging is in the positioning of the uniform light source in the background, illuminating the object of interest from behind (in present case, a falling droplet) and creating a shadow on the image. If the camera then focuses on the droplet, the boundary between the bright background and the droplet's

shadow appears distinct, enabling precise detection of the droplet's shape and size. Consequently, the droplet's characteristics can be extracted from the acquired images using an image processing algorithm.

Captured images of a falling droplet were used to calculate the drop diameter and drop impact velocity, which represent two governing impact parameters. In order to obtain reliable data and information on mentioned drop impact parameters, the calibration of the used high-speed camera is required. A calibration target is positioned at the original drop impingement location, and a snapshot of the target is taken. The calibration target contains various calibration fields as a chessboard pattern designed to measure the conversion factor and lens distortion. Constructed from Soda-Lime glass by *Edmund Optics*, the target featurs a structure created through laser lithography, with a maximum error of $\pm 0.3\,\mu m$. Additionally, a linear gauge is employed to establish the conversion factor, enabling precise calculations of the drop impact parameters. The recorded raw gray-scale videos are processed in a numerical computing environment using MathWorks MATLAB. For this purpose, gray-scale images capturing the falling droplet are selected for analysis and exported from the camera's native .cine format to .jpeg format. The unprocessed image is shown exemplary in Fig. 4.6. Next, the selected grayscale image is processed by an image processing algorithm implemented in the MathWorks MATLAB environment, which will be described below.

The algorithm automatically detects the drop during impact by background subtraction and subsequent conversion of the grayscale image into a binary image based on an adaptive grayscale method (Otsu, 1979). After loading the raw images into MathWorks MATLAB, contrast is enhanced to facilitate a more accurate conversion. Afterwards, the binarization process takes place, converting the image to black and white. Next, an automatic detection and elimination procedure was implemented to address processing errors and remove small artifacts in the converted image, such as secondary droplets, small impurities on the image originating from the dust on the camera sensors, and reflection in the drop itself. In the case of the suspension drops, with graphite particles, there is almost no reflection in the drop.

The shape of the drop is determined from the filtered binarized image by counting the white pixels, and the area equivalent drop diameter d_0 is computed directly from the image cross-section due to the highly spherical shape of the drop. To compute the impact velocity, the position of the centroid

of the drop needs to be determined on a frame-by-frame basis. In the following step, the velocity is calculated by analyzing the change in position of the centroid in each video frame, or the distance (in pixels) covered by the drop in each frame. Fig. 4.7 shows the crucial steps in determining the drop impact parameters according to the aforementioned image processing algorithm. Fig. 4.7b illustrates the detected drop shape in red and the centroid marked in blue.

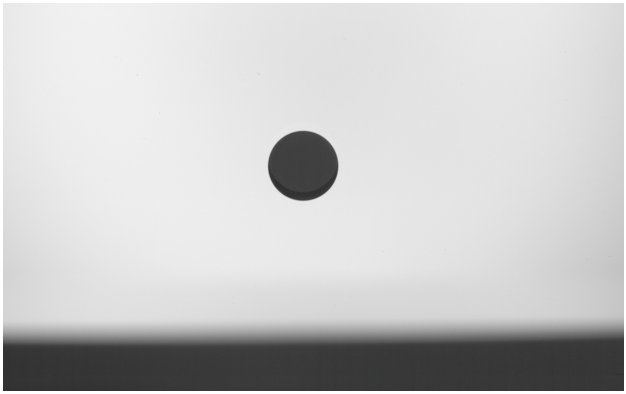

Figure 4.6: Unprocessed raw image of a falling suspension droplet.

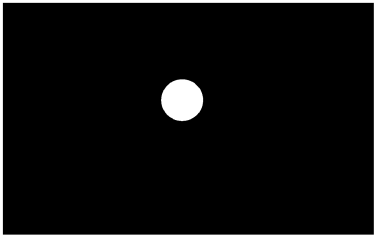

(a) Binarized image without impurities and reflection in the drop.

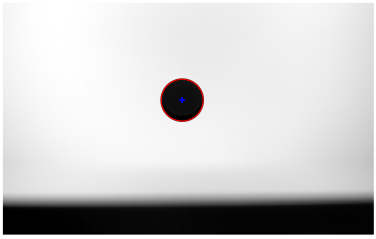

(b) Determining the centroid and droplet shape from the processed gray-scale image.

Figure 4.7: Exemplary steps of an image processing alghoritm for determining drop diameter d_0 and impact velocity U_0 of a suspension drop impacting a metal substrate.

5 Single drop impact of a suspension drop onto a hot substrate

In this chapter, different regimes of suspension drop impact under various substrate temperatures and impact conditions are presented. Section 5.1 focuses on observations related to the heat transfer in the nucleate boiling regime. It includes a qualitative description of the observed microscopic thermodynamic and hydrodynamic phenomena, along with measurements of the drop residence time. A self-proposed model describing the heat transfer in the nucleate boiling regime, as well as the particle deposition, is also discussed. In addition, the determination of the thickness of the solid deposit remaining on the substrate after the evaporation process is discussed. Finally, in Section 5.2 observations of the phenomena associated with the higher wall temperatures related to the thermal atomization and the film boiling regime are presented. Parts of the following sections, including text and figures, have been published in Gajevic Joksimovic et al. (2023c).

5.1 Nucleate boiling regime

At surface temperatures above the saturation point, the evaporation of a drop occurs due to nucleate boiling. During nucleate boiling of a water drop impacting on a wall, vapor bubbles frequently form at the surface of the drop or the surrounding wall, grow larger and possibly coalesence. These bubbles rise through the drop and eventually detach from the surface/liquid interface during the evaporation process (Breitenbach et al., 2017a). Nucleate boiling of suspension drops (along with the physics involved) in some means looks qualitatively similar, but is quantitatively completely different. Therefore, the influence of the particle volume concentration (also referred to as "suspension concentration" for convenience), both in terms of drop hydrodynamics and heat transfer during boiling, will be discussed below.

5.1.1 Observations

The observed hydrodynamic regimes of suspension drop impact onto a hot substrate are qualitatively similar to the regimes of drop impact of pure, one-component liquids, shown exemplary in Fig. 5.1(a)-(d), with some different effects attributed to the dispersed solid phase.

In Fig. 5.1 examples of a drop impact of pure water as well as suspensions of $\varphi = 1.43\,\%$ and $\varphi = 4.3\,\%$ onto a substrate with an initial temperature of $T_{w0} = 150\,°C$ are shown. In all three cases, the impact is governed by nucleate boiling. However, the phenomenon is significantly different in each case. Drop impact of pure water is accompanied by an intensive generation of fine secondary drops, appearing after 81 ms (see Fig. 5.1b), and several bubbles whose sizes exceed the height of the drop. Addition of a very small amount of solid particles leads to a significant time delay of splash inception. For the suspension of $\varphi = 1.43\,\%$, shown in Fig. 5.1(g), the splash has been observed after 300 ms and the size of the secondary drops is much larger compared to the case with distilled water. For higher suspension concentration, $\varphi = 4.3\,\%$, the splash is almost completely suppressed. Only a few relatively large secondary drops have been observed in the case presented in Fig. 5.1(i)-(l). After the complete evaporation of liquid from the suspension drop, a solid layer of the dispersed phase is left on the substrate, as shown in Fig. 5.1(h) or (l). Thus, it is essential to adequately clean the substrate before beginning a new experiment and reheating the substrate, as described in Section 4.1.1.

In order to better understand the main mechanisms that lead to splashing in the presented cases, the boiling of the distilled water drop shown in Fig. 5.2 is compared with the observations of the boiling in the suspension drop in Fig. 5.3.

Splashing of a liquid drop during the nucleate boiling regime occurs due to the breakup of thin film domes formed by an expanding vapor bubble when the bubble size is much larger than the thickness of the liquid layer at the substrate. The breakup process of the dome (Lhuissier & Villermaux, 2012; Opfer et al., 2014) shown in Fig. 5.2, includes the dome growth and spontaneous perforation by a hole, (Fig. 5.2b). The hole is confined by a Taylor rim (Taylor, 1959) which propagates along the liquid film. The rapid hole expansion is caused by rim propagation. Moreover, the rim itself is unstable, as can be seen in Fig. 5.2(c). The rim instability leads to the

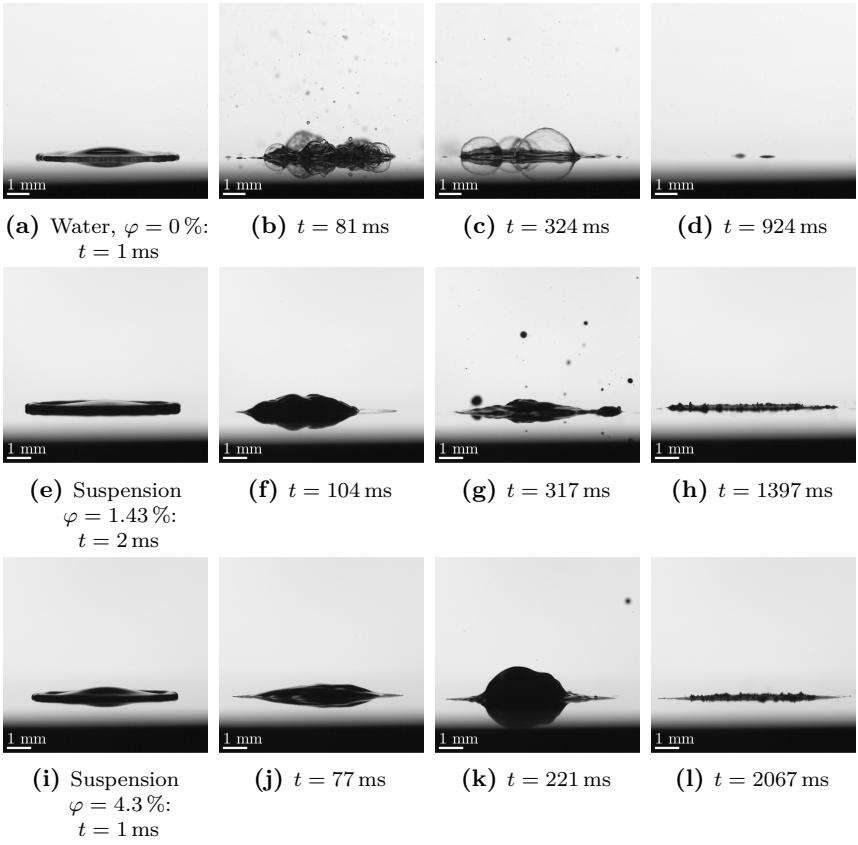

(a) Water, $\varphi = 0\,\%$: $t = 1\,\mathrm{ms}$ **(b)** $t = 81\,\mathrm{ms}$ **(c)** $t = 324\,\mathrm{ms}$ **(d)** $t = 924\,\mathrm{ms}$

(e) Suspension $\varphi = 1.43\,\%$: $t = 2\,\mathrm{ms}$ **(f)** $t = 104\,\mathrm{ms}$ **(g)** $t = 317\,\mathrm{ms}$ **(h)** $t = 1397\,\mathrm{ms}$

(i) Suspension $\varphi = 4.3\,\%$: $t = 1\,\mathrm{ms}$ **(j)** $t = 77\,\mathrm{ms}$ **(k)** $t = 221\,\mathrm{ms}$ **(l)** $t = 2067\,\mathrm{ms}$

Figure 5.1: Drop impact in the nucleate boiling regime. Effect of the suspension concentration, $\varphi = 0\,\%$ (distilled water) (a)-(d), $\varphi = 1.43\,\%$ (e)-(h) and $\varphi = 4.3\,\%$ (i)-(l) on the drop splash and evaporation. The initial substrate temperature $T_{w0} = 150\,°\mathrm{C}$, drop diameter $d_0 = 2.3$ mm and impact velocity $U_0 = 1.7$ m/s are the same for all the cases.

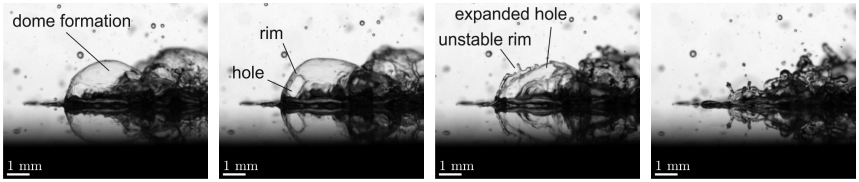

(a) $t = 86.1\,\mathrm{ms}$ **(b)** $t = 86.3\,\mathrm{ms}$ **(c)** $t = 86.4\,\mathrm{ms}$ **(d)** $t = 87.3\,\mathrm{ms}$

Figure 5.2: Impact and splash of a distilled water drop in the nucleate boiling regime. A typical behavior of a single dome formed from a growing vapor bubble. Its expansion (a), spontaneous hole formation (b), bounded by an unstable rim (c), breakup and collapse (d). The impact parameters correspond to the case shown in Fig.5.1(a)-(d).

formation of multiple finger-like jets, which break up into a number of fine secondary drops of the size comparable with the film thickness of the dome in the case presented. A typical example of dome growth and breakup during the impact of a suspension drop in the nucleate boiling regime is shown in Fig. 5.3.

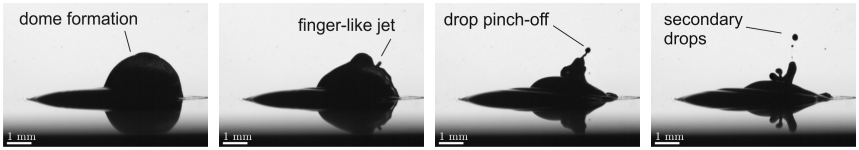

(a) $t = 224.8\,\mathrm{ms}$ **(b)** $t = 225.3\,\mathrm{ms}$ **(c)** $t = 225.6\,\mathrm{ms}$ **(d)** $t = 225.9\,\mathrm{ms}$

Figure 5.3: Impact and splash of a suspension drop in the nucleate boiling regime, $\varphi = 1.43\,\%$. A typical behavior of a single dome leading to the pinch-off of the secondary drops: dome formation and growth (a), unstable dome receding, leading to the formation of a finger-like jet (b), jet propagation and emergence of the jet instabilities (c), leading to the pinch-off of the secondary drops (d). The impact parameters correspond to the case shown in Fig.5.1(e)-(h).

The dome grows due to the evaporation of water from the suspension. Consequently, the concentration of the particles also grows, leading to a significant increase of the viscosity of the liquid film forming the dome. At some instant, the dome perforates and a Taylor rim propagates along the dome perimeter.

This stage is unstable and leads to the emergence of a jet. Finally, the dome collapses while several secondary drops appear after the jet breakup. In the case of suspensions, the diameter of largest secondary drops observed is about 200 µm, whereas in the case of distilled water, the diameter of largest secondary drops observed is around 100 µm. These observations are based on image analysis of a variety of different experiments.

5.1.2 Evaluation of heat transfer during drop evaporation

Stages of drop impact and boiling

To provide a framework for a one-dimensional model for heat transfer and particle deposition developed later in this section, the main phenomena accompanying the suspension drop impact, including spreading and boiling in the nucleate boiling regime, are schematically shown in Fig. 5.4. Drop impact leads to a generation of a thin radially spreading flow in a liquid lamella, as shown in Fig. 5.4(a). The drop spreading radius is determined by the propagation of a rim (Taylor, 1959) formed by capillary forces and viscous stresses at the wall (Roisman et al., 2002). If the Reynolds and Weber numbers are much higher than unity, the flow is described well by an inviscid flow. The solution for the flow in the lamella given by Yarin & Weiss (1995) satisfies the mass and the momentum balance equations for such an inviscid flow. The predicted scaling (Yarin & Weiss, 1995) for the lamella thickness $h_{\mathrm{lamella}} \sim t^{-2}$ is confirmed by numerous numerical simulations of drop impact and by experimental data (Roisman et al., 2009; Bakshi et al., 2007). The inviscid solution is valid only for the stage when the lamella is much thicker than the thickness of the viscous boundary layer formed at the substrate immediately after impact. The exact similarity solutions of the Navier-Stokes equations for viscous flow in the spreading drop are obtained for axisymmetric drop spreading (Roisman, 2009), as well as for a three-dimensional case associated with the oblique drop impact (Roisman, 2010b). The evolution of a uniform thickness of the viscous boundary layer is predicted in the form $h_\nu \sim \sqrt{\nu t}$. The predictions for the flow in the viscous boundary layer over the duration of the spreading phase and for the residual lamella thickness (Roisman, 2009) agree well with direct numerical simulations and with the experimental data (Eggers et al., 2010; Bakshi et al., 2007).

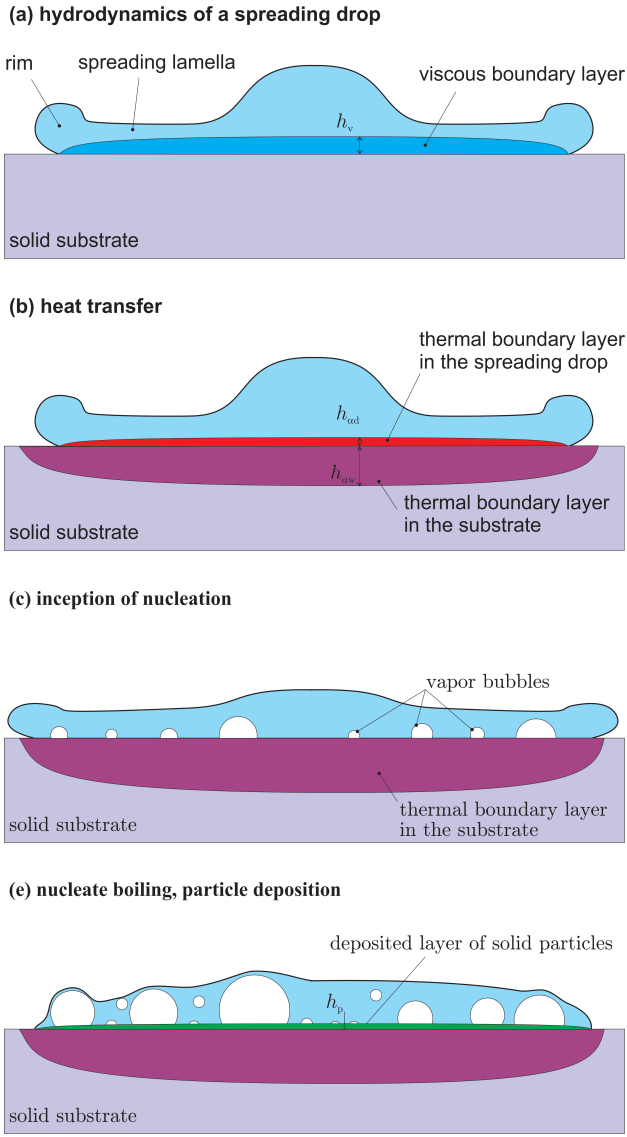

Figure 5.4: Sketch of the main phenomena accompanying the impact of a suspension drop onto a hot substrate in the nucleate boiling regime.

If the initial temperatures of the drop and the substrate differ, the heat transfer is governed by heat conduction in a thin thermal boundary layer in the substrate and by convection and conduction in a thermal boundary layer in the spreading lamella. The exact similarity solution (Roisman, 2010b) for this heat transfer problem satisfies the condition of the continuity of the temperature and of the heat flux at the substrate interface. The predicted thicknesses of the thermal boundary layers in the drop and in the substrate are respectively $h_{\alpha \mathrm{d}} \sim \sqrt{\alpha_{\mathrm{d}} t}$ and $h_{\alpha \mathrm{w}} \sim \sqrt{\alpha_{\mathrm{w}} t}$, where α denotes the thermal diffusivity of the corresponding material. The thickness of the thermal boundary layer is much smaller than the spreading diameter of the drop (see Fig. 5.4b). The ratio of the total heat flux in the substrate in the radial direction and the heat flux at the wetted interface in the axial direction is of the same order as the ratio of the corresponding lengths, $\sim h_{\alpha \mathrm{w}}/D_{\mathrm{spreading}} \ll 1$. The latter can be demonstrated for the suspension drops, where the measured spreading diameter is approximately $D_{\mathrm{spreading}} \approx 5$ mm. Next, the thermal diffusivity of the used metal substrate is $\alpha_{\mathrm{w}} \sim 10^{-5}$ m^2/s. Thus, for all cases where the drop residence time is less than one second, the heat transfer is dominated by conduction in a thin thermal boundary layer (*i.e.*, the heat flux in the axial direction is dominant), since for these cases $\sim h_{\alpha \mathrm{s}}/D_{\mathrm{spreading}} \ll 1$. Most of the experiments in this study satisfy this condition.

The theoretical predictions based on the similarity solution for the heat flux (Roisman, 2010b) agree very well with direct numerical computations of heat transfer in a spreading drop (Berberović et al., 2011; Schremb et al., 2017; Batzdorf et al., 2017).

This result is very important for the current study, which indicates that the heat transfer problem in the substrate and in the liquid drop can be solved using a simplified one-dimensional approach. Moreover, a similar one-dimensional approach is used to treat the problems influenced by phase change theoretically, for example to predict the thickness of an ice layer (Schremb et al., 2018) after impact of a supercooled drop onto an ice substrate, or to estimate the heat transfer associated with drop or spray impact onto a hot substrate in the nucleate boiling and film boiling regimes (Breitenbach et al., 2017b,a; Tenzer et al., 2019). During drop spreading, superheating of the liquid occurs before the vapor bubbles appear. Once the time after impact exceeds the bubble waiting (delay) time (Carey, 2020), numerous vapor bubbles appear at the wetted substrate interface. This phenomenon

is shown schematically in Fig. 5.4(c). The temperature at the interface of an evaporation bubble is equal to the saturation temperature of the liquid. Preceding studies (Breitenbach et al., 2017a; Tenzer et al., 2019) have shown that the temperature of the liquid/solid interface quickly approaches the saturation temperature. This determines the thermal boundary conditions for the heat transfer problem in the substrate and significantly simplifies the problem modeling.

Particle deposition near the wall region

In the nucleate boiling regime, the presence of the particulate phase combined with the intensive liquid evaporation at the surface leads to two phenomena that significantly affect the process. These phenomena are the formation and growth of vapor bubbles and the deposition of particles on the substrate.

Formation and growth of vapor bubbles, observed during nucleate boiling, indicates that the surrounding liquid in the vicinity of the substrate is slightly superheated. Bubble evaporation occurs at the interface, where the temperature is close to the saturation temperature. Liquid evaporation at the bubble surface leads to the continuous reduction of the liquid content in the suspension, and correspondingly to the increase of the concentration of the solid phase. Therefore, the bulk viscosity of the suspension increases. This is the main reason for the reduction of the rate of splashing for suspension drops in comparison with the splash of distilled water drops.

The second phenomenon is associated with the nucleation of a vapor bubble and its rapid expansion, leading to the dewetting motion of the contact line formed on the substrate by each bubble. Particle deposition consequently occurs in the vicinity of the moving contact line. This effect is known in the literature as the coffee-ring effect (Deegan et al., 1997; Denkov et al., 1993; Yunker et al., 2011), which is already scrutinized in Section 2.3. The evaporation of multiple vapor bubbles at the substrate thus leads to the formation of a porous particulate layer, as shown schematically in Fig. 5.4(e).

It is important to clarify whether the scaling for the drop residence time, required for its complete evaporation at the substrate, developed for pure liquids (Breitenbach et al., 2017a) is still applicable for the modeling of heat transfer and evaporation of multiphase drops.

In the next section, a one-dimensional model for heat transfer in the

substrate and for the particle deposition is developed, which is based on the above-mentioned simplified theoretical approach.

Model for heat flux and particle deposition

Consider the impact of a liquid drop onto a solid dry, semi-infinite substrate, initially heated to the uniform temperature T_{w0}. Impact leads to the disturbance of the temperature field $T_w(x,t)$ in a thin expanding thermal boundary layer in a solid target, as shown schematically in Fig. 5.5.

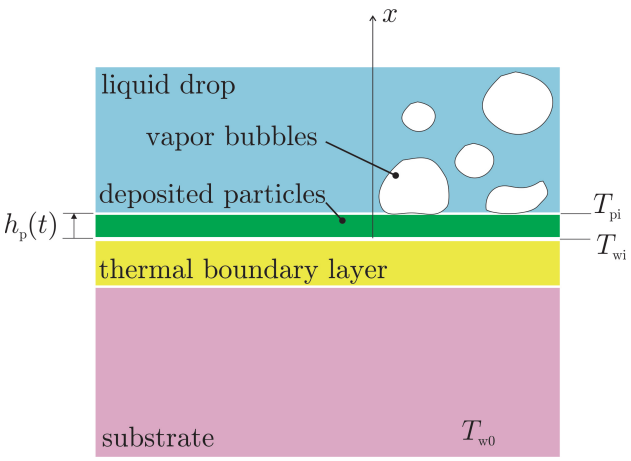

Figure 5.5: Heat transfer in a substrate, liquid drop and in a deposited layer of the particles from the suspension.

Moreover, during drop evaporation, a particulate layer is formed at the substrate. The thickness of this layer is denoted $h_p(t)$. All the terms with the subscript p in this analysis correspond to this layer. In the experiments, the value of the Stokes number, estimated with the help of Eq. (2.40), is $\mathrm{Stk} \sim 10^{-2}$. This value is much smaller than unity, indicating that the effect of convection of the particles in the suspension can be neglected. Moreover, the diffusion of the particles is neglected as well, since the value of the Péclet number, estimated using Eq. (2.41), is $\mathrm{Pe} \sim 10^{10} \gg 1$.

In order to evaluate the influence of the deposited particles on the heat transfer during drop evaporation and on the scale for the characteristic

residence time of this drop in the nucleate boiling regime, a one-dimensional model is developed in this study. The model is valid when the thickness of the deposited layer h_p and the thickness of the thermal boundary layer in the substrate are both much smaller than the spreading diameter of the drop.

The ratio of the thickness of thermal boundary layer to the spreading diameter and its relevance to the validity of the simplified one-dimensional approach to the thermal problem have been discussed in Section 5.1.2.

For the suspensions drops considered in this study, the thickness of the deposited layer is significantly smaller than the drop spreading diameter. This is ensured by the small values of the volumetric concentrations of the particulate phase $\ll 1$. The measured residual thickness of the deposited layer is $\sim 10^{-4}$ m, as shown later in Fig. 5.6, while the spreading diameter is $\sim 10^{-2}$ m. Moreover, the average thickness of the deposited layer in Fig. 5.6 is almost independent on the radial coordinate, except in close vicinity to the spot edge. This result supports the simplified assumption of the mainly one-dimensional heat transfer at the substrate.

The one-dimensional heat equation in the wall and solid layer region is given as

$$\frac{\partial T_\mathrm{w}}{\partial t} = \alpha_\mathrm{w} \frac{\partial^2 T_\mathrm{w}}{\partial x^2}, \quad \frac{\partial T_\mathrm{p}}{\partial t} = \alpha_\mathrm{p} \frac{\partial^2 T_\mathrm{p}}{\partial x^2} \tag{5.1}$$

where α_w and α_p are the thermal diffusivities of the wall and the particulate layer, respectively, x is the axial coordinate and t is the time after impact.

The heat equations have to be solved using the boundary conditions

$$T_\mathrm{w} = T_{\mathrm{w}0} \quad \text{and} \quad \lambda_\mathrm{w} \frac{\partial T_\mathrm{w}}{\partial x} = 0 \quad \text{at} \quad x \to -\infty, \tag{5.2}$$

$$T_\mathrm{w} = T_\mathrm{p} = T_\mathrm{wi} \quad \text{and} \quad \lambda_\mathrm{w} \frac{\partial T_\mathrm{w}}{\partial x} = \lambda_\mathrm{p} \frac{\partial T_\mathrm{p}}{\partial x} \quad \text{at} \quad x = 0, \tag{5.3}$$

$$T_\mathrm{p} = T_\mathrm{pi} \quad \text{at} \quad x = h_\mathrm{p}(t), \tag{5.4}$$

where λ_w and λ_p are the thermal conductivities of the wall and deposited layer regions respectively, T_wi is the unknown temperature of the substrate interface and T_pi is the temperature of the wetted interface of the solid deposited layer. These boundary conditions are based on the continuity of the temperature and the heat flux at the interfaces. The surface of the deposited layer experiences nucleation and expansion of the vapor bubbles, as shown schematically in the sketch in Fig. 5.5. It has been shown already in the analysis of the nucleate

boiling of pure, one-component liquids (Breitenbach et al., 2017a) that the temperature T_{pi} of the wetted interface of the solid deposited layer lies rather close to the saturation temperature T_{sat}

$$T_{\mathrm{pi}} \approx T_{\mathrm{sat}}. \tag{5.5}$$

This assumption is based on the fact that the liquid evaporates at the contact lines of bubbles, where the temperature is close to T_{sat}. This assumption allows to accurately estimate the evaporation time of a liquid drop in the nucleate boiling regime as shown in Roisman (2010a) and Breitenbach et al. (2017a).

Next, the deposition rate of the particles is governed by the evaporation rate of the liquid $\dot{m}_{\mathrm{ev}}$

$$\dot{m}_{\mathrm{ev}} = -\frac{\lambda_{\mathrm{p}}}{L}\frac{\partial T_{\mathrm{p}}}{\partial x} \quad \text{at} \quad x = h_{\mathrm{p}}(t). \tag{5.6}$$

Then, the mass balance at the interface of the deposited layer yields

$$\frac{\mathrm{d}h_{\mathrm{p}}}{\mathrm{d}t} = -\chi\frac{\varphi}{1-\varphi}\frac{\lambda_{\mathrm{p}}}{\rho_{\mathrm{l}}L}\frac{\partial T_{\mathrm{p}}}{\partial x} \quad \text{at} \quad x = h_{\mathrm{p}}(t), \tag{5.7}$$

where φ is the volumetric concentration of the dispersed, particulate phase in the suspension, ρ_{p} and ρ_{l} are the densities of the particles and of the liquid phase, L is the latent heat of vaporization. This equation is formulated for relatively large particles of size larger than 1 µm, for which the effects of the diffusion or Brownian motion are small, and the evaporation occurs exclusively at the interface of the deposited layer. This assumption is not always precise, since the mass balance can be influenced by the motion of the particles caused by the liquid flow and by the mass loss due to splash. Therefore, an empirical coefficient χ is introduced in Eq. (5.7) to account for these effects. In addition, the porosity of the layer of randomly deposited solid particles must be taken into account a priori by the aforementioned coefficient.

The similarity solution of system of Eqs. (5.1) is found in the form

$$T_{\mathrm{w}} = T_{\mathrm{wi}} - (T_{\mathrm{w0}} - T_{\mathrm{wi}})\mathrm{erf}\left[\frac{x}{2\sqrt{\alpha_{\mathrm{w}}t}}\right], \tag{5.8}$$

$$T_{\mathrm{p}} = T_{\mathrm{wi}} - \frac{e_{\mathrm{w}}(T_{\mathrm{w0}} - T_{\mathrm{wi}})}{e_{\mathrm{p}}}\mathrm{erf}\left[\frac{x}{2\sqrt{\alpha_{\mathrm{p}}t}}\right], \tag{5.9}$$

where e_p and e_w are the particle and wall thermal effusivities and

$$h_\mathrm{p} = H\sqrt{\alpha_\mathrm{p} t}, \tag{5.10}$$

$$T_\mathrm{wi} = \frac{T_\mathrm{sat} e_\mathrm{p} + T_\mathrm{w0} e_\mathrm{w} \mathrm{erf}\frac{H}{2}}{e_\mathrm{p} + e_\mathrm{w}\mathrm{erf}\frac{H}{2}}. \tag{5.11}$$

The dimensionless thickness of the deposited layer H is the root of a transcendental equation

$$H = 2\chi \frac{\rho_\mathrm{p}}{\rho_\mathrm{l}} \frac{\varphi}{1-\varphi} \frac{e_\mathrm{w} \exp\left[-\frac{H^2}{4}\right]}{\sqrt{\pi}\left(e_\mathrm{p} + e_\mathrm{w}\mathrm{erf}\left[\frac{H}{2}\right]\right)}\mathrm{Ja}, \tag{5.12}$$

where the dimensionless Jakob number is defined in the form

$$\mathrm{Ja} = \frac{c_\mathrm{p}(T_\mathrm{w0} - T_\mathrm{sat})}{L}, \tag{5.13}$$

with c_p being the heat capacity of the particles. The heat flux $\dot{q}_\mathrm{p}$ at the interface of the deposited particle layer is expressed as

$$\dot{q}_\mathrm{p} = -\lambda_\mathrm{p} \frac{\partial T_\mathrm{p}}{\partial x}_{|x=h_\mathrm{p}} = \frac{\exp\left[-\frac{H^2}{4}\right] e_\mathrm{p} e_\mathrm{w} (T_\mathrm{w0} - T_\mathrm{sat})}{\sqrt{\pi t}\left(e_\mathrm{p} + e_\mathrm{w}\mathrm{erf}\left[\frac{H}{2}\right]\right)}. \tag{5.14}$$

In the experiments, the estimated values of the dimensionless layer thickness correspond to $H \ll 1$. Thus, the expression for H can be reduced to

$$H \approx 2\chi \frac{\rho_\mathrm{p}}{\rho_\mathrm{l}} \frac{\varphi}{1-\varphi} \frac{e_\mathrm{w}}{\sqrt{\pi} e_\mathrm{p}}\mathrm{Ja}. \tag{5.15}$$

For the present case, the density of graphite (Pavlov et al., 2017) is $\rho_\mathrm{p} = 2260$ kg/m^3, thermal diffusivity $\alpha_\mathrm{p} = 3.5 \times 10^{-5}$ m^2 s^{-1}, thermal conductivity $\lambda_\mathrm{p} = 80$ W m^{-1} K^{-1}, and the thermal effusivity of stainless steel $e_\mathrm{w} = 8.9 \times 10^3$ J K^{-1} m^{-2} s$^{-1/2}$, latent heat of water vaporization $L = 2.26 \times 10^6$ J/kg, and water density $\rho_\mathrm{l} = 10^3$ kg m^{-3} with $T_\mathrm{w0} - T_\mathrm{sat} = 10^2$ K. Correspondingly, $H \sim 10^{-2}$ is obtained. Therefore, the dimensionless layer thickness H, defined in Eq. (5.10) is indeed much smaller than unity. The estimated layer thickness obtained from the model is compared with the confocal microscope thickness measurements below.

Porous deposited layer of solid particles

For comparison, the experimental parameters corresponding to the measurement case shown in Fig. 5.6 are used in the following. For the initial substrate temperature $T_{w0} = 150\,°C$ and the suspension concentration $\varphi = 4.3\%$ the measured residence time of a 2.3 mm drop is $t = 2$ seconds. The estimated value of the deposited layer thickness corresponding to this case, approximated by the expressions (5.10) and (5.15), is $h_p \sim 13.5\chi$ µm.

On the other hand, h_p can also be estimated from the total mass conservation of the drop and the particles, $h_p \approx 2d_0^3\varphi/3D_{\text{spreading}}^2 \approx 25.2\,\mu\text{m}$. This value corresponds to the maximum volume-averaged thickness of the deposited layer, where the spreading diameter of the drop $D_{\text{spreading}} \approx 5$ mm. Comparing this value with the one estimated with the expressions (5.10) and (5.15) ($h_p \sim 13.5\chi$ µm) gives the value of the empirical fitting coefficient $\chi = 1.86$, introduced in Eq. (5.7). Note that the value of χ is of the order of unity, meaning that most of the physical phenomena are taken into account in the model. The introduction of the factor χ is however necessary, since the exact values of the thermodynamic properties of the porous deposited layer are not known.

A 3D surface scan of a particulate layer is shown in Fig. 5.6, obtained after the impact of a suspension drop and complete evaporation of the drop. A confocal microscope (*Mahr MarSurf CM*) is used for the measurements. The deposited layer is highly porous with varying height. The circular, particle-free dark regions in the upper graph in Fig. 5.6 correspond to the positions where bubbles were located before complete evaporation. Therefore, the relative area of the particle-free surface is measured, yielding a value of $\epsilon_0 = 0.42$. Finally, the apparent area averaged layer thickness is determined to be $h_{\text{exp}} = 50.80\,\mu\text{m}$. This thickness is significantly larger than the theoretically predicted volume averaged thickness h_{p} of the layer. The difference is explained by the porosity of the layer, which can be roughly approximated by the $\varphi_{\text{spheres}} \approx 0.6$ of randomly close packing of hard spheres (Scott & Kilgour, 1969; Berryman, 1983; Coelho et al., 1997). The theoretically predicted average thickness of the porous deposited layer is therefore $h_{\text{p}}/\varphi_{\text{spheres}} \approx 42.0\,\mu\text{m}$. This value is of the same order as the measured value h_{exp}. An attentive reader may wonder why the apparent layer shown in Fig. 5.6 looks much thicker. This impression is caused by the presence of $\sim 200\,\mu\text{m}$ high coffee-rings around the particle

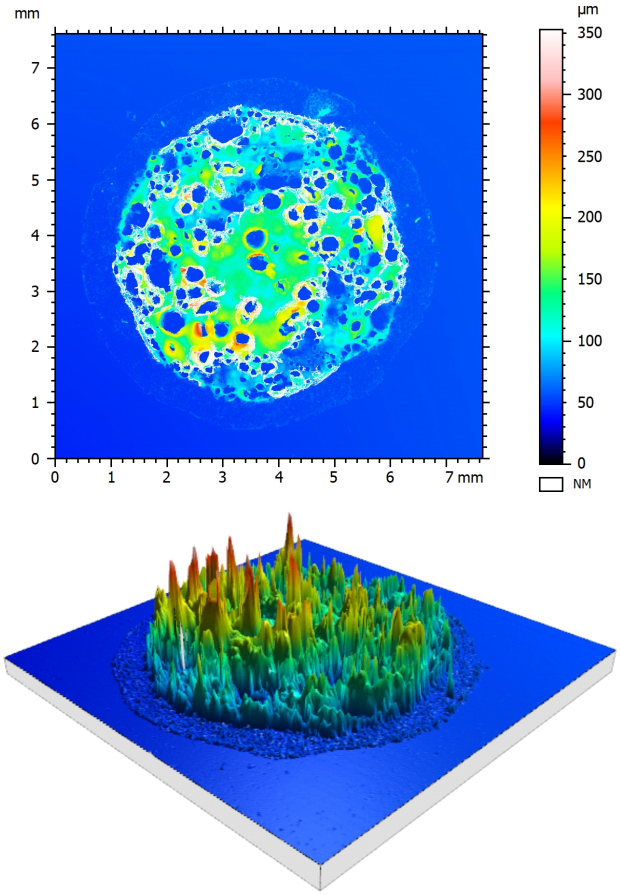

Figure 5.6: Confocal microscope images of the deposited layer after suspension drop ($\varphi = 4.3\,\%$) impact onto a hot substrate. The parameters of impact correspond to the case shown in Fig. 5.1(i)-(l).

free holes produced by the vapor bubbles.

Note that the 3D contour of the residue shows 2 distinct zones (Figure 5.6, bottom graph) with an outer ring of lower thickness and a central zone of increased residue thickness. This is due to the spreading zone during the initial drop spreading on the substrate. This spreading diameter corresponds

to the maximum spreading diameter as shown in Roisman (2009); Lagubeau et al. (2012) and Cheng (1977). However, boiling of the drop occurs on the contact diameter, in the "inner" zone, as shown in Fig. 5.6.

5.1.3 Residence time of an impacting suspension drop

The expression (5.14) for $\dot{q}_\mathrm{p}$ can be linearized using the value of the dimensionless thickness of the deposited layer H as a small parameter

$$\dot{q}_\mathrm{p} = \frac{e_\mathrm{p} e_\mathrm{w} \left(T_\mathrm{w0} - T_\mathrm{sat}\right)}{\sqrt{\pi t}\left(e_\mathrm{p} + e_\mathrm{w}\frac{H}{\sqrt{\pi}}\right)} \tag{5.16}$$

$$\Delta T_\mathrm{w} = T_\mathrm{w0} - T_\mathrm{sat} \tag{5.17}$$

which in the limit $H = 0$ yields the well-known expression (Roisman, 2010a; Breitenbach et al., 2017a)

$$\dot{q}_\mathrm{p} \approx \frac{e_\mathrm{w}\Delta T_\mathrm{w}}{\sqrt{\pi t}}. \tag{5.18}$$

The total heat Q_single transferred from the wall during complete drop evaporation can be estimated by integration of expression (5.16) over time. The residence time is then evaluated from the total energy balance, by equating Q_single with total energy required for complete drop evaporation (Roisman, 2010a; Breitenbach et al., 2017a). The resulting expression is

$$t_\mathrm{r} \sim \pi \left[\frac{\rho L^* d_0 \left(e_\mathrm{p} + e_\mathrm{w}\frac{H}{\sqrt{\pi}}\right)}{12 e_\mathrm{p} e_\mathrm{w} \Delta T_\mathrm{w}}\right]^2, \tag{5.19}$$

where $L^* = L + \Delta H_0$ denotes the sum of the latent heat of vaporization L, and the enthalpy change between the initial state and the saturated state of the drop liquid, ΔH_0. This equation can be reduced to the following form $t_\mathrm{r} = \pi \left[\frac{\rho L^* d_0}{12 k_\mathrm{w} e_\mathrm{w} \Delta T_\mathrm{w}}\right]^2$, which is the same as the form for simple one-component liquids, already introduced in Section 2.2.2 as Eq. (2.15). The theoretical predictions based on expression (2.15) agree very well with numerous experimental data (Abu-Zaid, 2004; Buchmüller, 2014; Itaru & Kunihide, 1978; Tartarini et al., 1999) for one-component liquids.

Therefore, Eq. (2.15) can be applied to suspension drops, showing that the scaling obtained for one-component liquids also holds for suspensions, despite the influence of the particulate phase and the consequent formation of the deposited layer. An empirical constant k_w is introduced into Eq. (2.15), which accounts for effects caused by the surface roughness or wettability of the substrate material used, as well as the formation of the deposited layer. The value $k_w = 1.9$ has been obtained for distilled water drops (Roisman, 2010a; Breitenbach et al., 2017a). The theoretical curve resulting from Eq. (2.15) for distilled water drops is plotted as a dashed line in Fig. 5.7.

In order to characterize the influence of the dispersed solid phase on the suspension drop impact, the residence time is measured from the initial collision of the drop with the hot substrate to the complete rebound, disintegration, or evaporation, depending on the thermodynamic regime of the event. The residence time can also be referred to as "contact time" in the literature (see Sections 2.2.2 and 2.2.3). However, in the discussion in this work, the term "residence time" is found to be better suited as in the film boiling regime, there is no actual contact due to a thin vapor layer. The residence times of suspension drops were measured for various particle volume concentrations over a wide range of wall overheat temperatures. The resulting residence times are also plotted in Fig. 5.7. Additionally, the measured residence time of the distilled water drops is shown for comparison.

Values of corresponding Reynolds numbers for the obtained data vary from 2814 to 3059 where $\mathrm{Re} = 2814$ corresponds to the largest suspension concentration $\varphi = 4.3\,\%$, while $\mathrm{Re} = 3059$ corresponds to the distilled water case. The range of Weber numbers is, $\mathrm{We} = 60 - 56$, accordingly.

For the presented suspension cases, nucleate boiling with pronounced foaming was observed in the range of the wall temperatures, corresponding to $\Delta T_w = T_{w0} - T_{sat}$ from 50 °C to 100 °C. As can be seen, the data for water and for suspensions follow the predicted values from Eq. (2.15) scaling $t_r \sim \Delta T_w^{-2}$.

To demonstrate the negligible contribution of the effect of the deposited particles on the heat transfer in the nucleate boiling regime, the validity of the residence time Eq. (2.15) was examined by measuring the residence time of a distilled water drop impacting on a solid deposited layer formed by a preceding suspension drop impact in the nucleate boiling regime. Such deposited layers formed on the substrate after the impact of suspension drop are shown in Fig. 5.1(h) or (l). The difference in measured residence time between a distilled

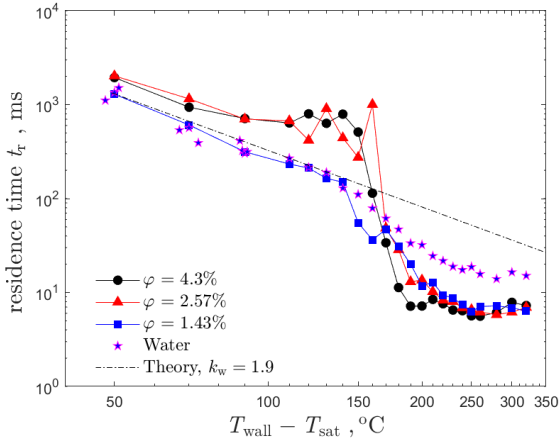

Figure 5.7: The residence time of the impacting drop as a function of the substrate overheat temperature for various suspension concentrations in comparison with the theoretical predictions (Eq. 2.15). Drop diameter $d_0 = 2.3$ mm and impact velocity $U_0 = 1.33$ m/s are the same for all the cases.

water drop impacting a clean substrate and onto a deposited layer is minor. This finding supports the estimation that the presence of deposited particles has a minimal effect on heat transfer in the nucleate boiling regime.

While the decrease in residence times for suspensions of lower concentrations or pure water can be attributed to the higher mass of secondary drops, the residence time values of suspension drops increase for higher suspension concentrations at smaller wall overheats up to 170 °C (refer to Fig. 5.7). Increasing suspension concentration results in a sudden change in the slope of the curves for overheats greater than 170 °C. This abrupt change is related to the onset of rebound after the drop dancing regime, which is associated with the transitional boiling (Schmidt et al., 2023). The change is more pronounced for higher suspension concentrations due to the greater effect of the particle layer as more vapor clusters are trapped along the particle surfaces, promoting boiling. However, in the range of overheat from 100 °C to 170 °C, for higher suspension concentrations, $\varphi = 2.57$ % and $\varphi = 4.3$ %, the change in residence time between them is small. This indicates that the

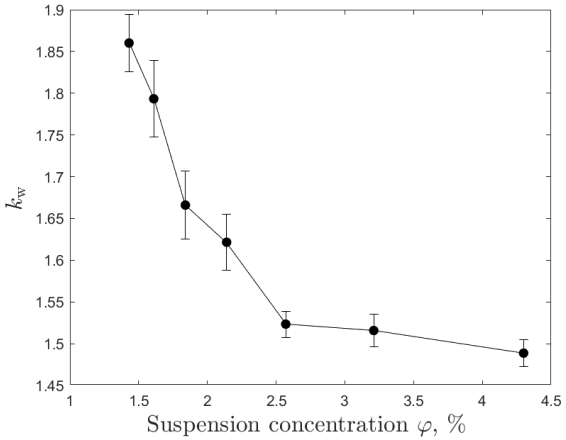

Figure 5.8: Dependence of the dimensionless empirical constant k_w, defined in Eq. (2.15), on the solid phase volume concentration φ in the suspension. The error bars represent one standard deviation.

mass of the secondary drops is negligibly small compared to the initial drop mass. Therefore, the heat from the wall is completely directed towards the evaporation of the drop with minor influence from the splash.

The variation of the residence time in the expression (2.15) can be implemented through adjustment of the dimensionless parameter k_w. The dependence of k_w on the volume concentration of the solid particles in the suspension is shown in Fig. 5.8. For smaller values of φ the constant k_w approaches the value $k_w = 1.9$, determined for water. For larger suspension concentrations, the value of the constant approaches the limiting nearly constant value $k_w \approx 1.5$, corresponding to the case when the splash is almost completely suppressed. With this in mind, and considering that the constant k_w also accounts for effective drop growth due to bubble expansion and mass loss during atomization (Breitenbach et al., 2017a), it becomes apparent that the differences in the value of the constant are related to the reduced splashing rate observed for higher suspension concentrations.

5.2 Higher wall temperatures: film boiling and thermal atomization

The drop residence time on the substrate is determined by the time the drop loses mass due to splashing and evaporation. At higher temperatures, above the Leidenfrost point, drop rebound upon impact can occur. Another possible outcome when the substrate is at a higher temperature is that the liquid film is disrupted by vapor flow during the collision of the drop with the substrate. This thermodynamic outcome is attributed to the thermal atomization regime (Roisman et al., 2018; Emerson et al., 2021; Chen et al., 2022b). In the thermal atomization regime, only the central part of the drop lamella is in contact with the substrate, while the peripheral part of the lamella floats in a

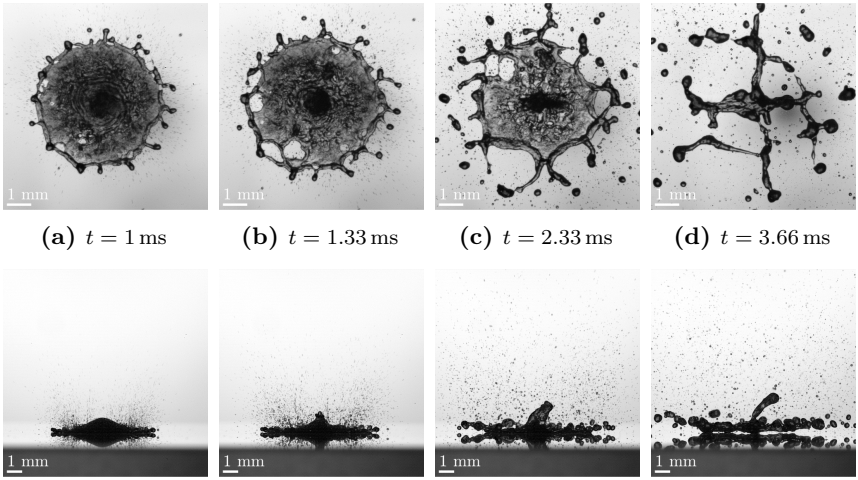

(a) $t = 1\,\mathrm{ms}$ **(b)** $t = 1.33\,\mathrm{ms}$ **(c)** $t = 2.33\,\mathrm{ms}$ **(d)** $t = 3.66\,\mathrm{ms}$

(e) $t = 1\,\mathrm{ms}$ **(f)** $t = 1.33\,\mathrm{ms}$ **(g)** $t = 2.33\,\mathrm{ms}$ **(h)** $t = 3.66\,\mathrm{ms}$

Figure 5.9: Simultaneous view of a suspension drop impact $\varphi = 1.43\,\%$ on a transparent sapphire substrate in the thermal atomization regime. (a)-(d) corresponds to the bottom view through the sapphire glass, while (e)-(h) corresponds to the side view of the same drop. Initial conditions are the same, including the initial substrate temperature $T_{\mathrm{w0}} = 350\,^{\circ}\mathrm{C}$, drop diameter $d_0 = 2.3$ mm and impact velocity $U_0 = 1.7$ m/s.

fast vapor stream ejected near the contact line. As a result, the drop impact in the thermal atomization regime results in complete drop disintegration and the generation of various fine secondary droplets, as shown in Fig. 5.9 for a drop of suspension concentration $\varphi = 1.43\%$.

The rapid vertical production of fine secondary droplets and the final disintegration of the drop are not caused by inertia, but by thermal effects (Breitenbach, 2019; Roisman et al., 2018). Only this form of atomization is considered and is hereafter referred to as thermal atomization.

Interestingly, the impact of suspension drops at higher temperatures, above the Leidenfrost point, almost always leads to thermal atomization, even for a wider range of impact velocities, up to 2 m/s. Moreover, even the impact of a suspension drop with the lowest particle concentration investigated ($\varphi = 1.43\%$) leads to this characteristic behavior, as illustrated in Fig. 5.9.

The observed behavior contrasts with that of distilled water drops, resembling film boiling phenomena with thermal rebound (see Fig. 5.10(a)-(d)). This difference in observed behavior suggests that the presence of particles strongly influences the thermodynamic events taking place. Therefore, in the following sections, a comparative analysis with observations of the phenomena occurring for suspension drop impact as well as for water drop impact will be provided.

5.2.1 Observations

In the range of wall overheat $\Delta T_\mathrm{w} = 100\,^\circ\mathrm{C} - 170\,^\circ\mathrm{C}$, experimental data for the residence time, shown in Fig. 5.7, deviate noticeably from the theoretical model for the nucleate boiling. This deviation can be attributed to the apparent drop foaming and reduction of the wetted contact area with the substrate, associated with the transition boiling regime. In this regime, the residence time of the suspension drops is much longer in comparison with distilled water drops.

Above the wall temperature corresponding to $\Delta T_\mathrm{w} \approx 200\,^\circ\mathrm{C}$, a termination of the transition boiling regime occurs, and all curves fall to a lower plateau. Hence, the behaviour associated with $\Delta T_\mathrm{w} \gg 200\,^\circ\mathrm{C}$ is investigated in more detail. Several examples of a drop impact onto a solid substrate initially heated to the temperature $T_\mathrm{w0} = 420\,^\circ\mathrm{C}$ (corresponding to $\Delta T_\mathrm{w} = 320\,^\circ\mathrm{C}$) are shown in Fig. 5.10 for pure water and two different supension concentrations.

At this temperature, the drop impact of distilled water leads to a total drop rebound, caused by the film boiling phenomenon, corresponding to the case shown in Fig. 5.10(a)-(d).

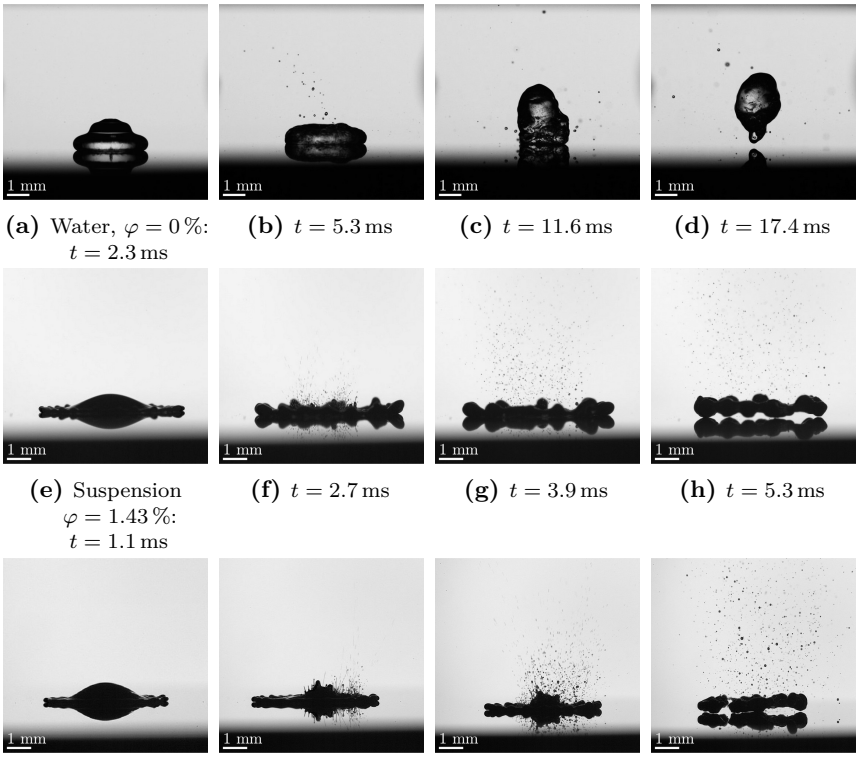

Figure 5.10: Drop impact onto a hot substrate initially heated to the temperature $T_{w0} = 420\,^{\circ}\mathrm{C}$. Effect of the suspension concentration, $\varphi = 0\,\%$ (distilled water) (a)-(d), $\varphi = 1.43\,\%$ (e)-(h) and $\varphi = 4.3\,\%$ (i)-(l) on the regime of drop impact. The initial drop diameter $d_0 = 2.3$ mm and impact velocity $U_0 = 1.7$ m/s are the same for all the cases.

Interestingly, even very small concentrations of solid particles cause a completely different drop behavior, as shown in Fig. 5.10(e)-(h) for the lowest suspension concentration considered $\varphi = 1.43\,\%$. In the following, the mechanisms leading to the mentioned observations, *i.e.*, thermal rebound in the case of distilled water drops and thermal atomization in the case of suspension drops will be explained.

Mechanisms of thermal rebound of a one-component liquid drop

Before starting a discussion on the different behavior of suspension drops, it is necessary to describe the mechanisms of rebound of the distilled water drop as a pure liquid. Rebound of pure liquid drops and accompanying phenomena are described in detail in the recent experimental and theoretical study by Schmidt et al. (2021b).

The duration of the drop spreading is determined by the time required for the expansion of the viscous boundary layer to the thickness of the radially spreading lamella (Roisman, 2009). In the nucleate boiling regime, the spreading is influenced by the generation of multiple vapor bubbles, as already discussed in Section 2.2.1. Clearly, the intensity of evaporation increases with the initial substrate temperature. If the nucleation sites are randomly distributed on the substrate and in time, there is a probability of their coalescence. Under certain conditions, when the percolation threshold is reached, the bubble clusters form continuous vapor channels (Schmidt et al., 2021b). This changes the character of the flow.

A comparison of the drop spreading time and the time required for bubble percolation, leading to the formation of the vapor channels at the substrate surface, allows to estimate the temperature at which the drop rebounds from the substrate after its spreading and receding (Schmidt et al., 2021b). The estimated temperatures for the drop rebound

$$T_{\mathrm{Leidenfrost}} - T_{\mathrm{sat}} \sim T_{\mathrm{rebound}} - T_{\mathrm{sat}} \sim \frac{\rho\sqrt{\nu}L^*}{e_{\mathrm{w}}}, \tag{5.20}$$

correlate well with the Leidenfrost temperature for spray impact. Here ρ, ν and e_{w} are the density, kinematic viscosity of the liquid and the thermal effusivity of the substrate, respectively. L^* is the sum of the latent heat of evaporation L and the enthalpy difference between the initial drop and saturated liquid while T_{sat} is the saturation temperature.

It is important to note that the temperature T_{rebound} is much lower than the temperature associated with the inception of the film boiling regime. The rebound occurs despite the drop contact with the substrate.

5.2.2 Suppression of film boiling by solid phase

The contact of a suspension drop with a hot substrate initiates a very strong local heat flux, violent evaporation and formation of the vapor flow, accelerating the particles. This is analogous to thermal atomization of one-component liquid drops (Roisman et al., 2018), when the impact velocity is so high that it ensures the contact of the liquid and the substrate even at very high temperatures. A key difference in the case of suspension drops, however, is the ejection of multiple jets that are formed in the early stages of drop impact due to the aforementioned vapor flow, as seen in Fig. 5.10(f) or (j). No such jetting phenomenon has been observed for pure, one-component drops.

Moreover, further suspension drop behavior in the case presented in Fig. 5.10 is very similar to the thermal atomization regime of a one-component liquid (Roisman et al., 2018). This regime is characterized by the generation of a dense uprising flow of fine secondary drops and the drop levitation before receding. This phenomenon is associated with the contact of the liquid and the very hot substrate, promoted by the high impact velocity of the drop. However, in the case of suspension drops, the drop rebound is prevented even at relatively low impact velocities, $U_0 \leq 1$ m/s. This behavior can be explained by several factors. First is the pinning of vapor bubbles at the coffee rings, shown in Fig. 5.6. These rings ensure a constant position for the bubble nucleation, since the corresponding spots are particle free. Therefore, the deposited layer prevents bubble coalescence and their percolation, which would allow drop rebound. The mechanism is analogous to the inverse Leidenfrost effect achieved by coating the solid substrate with a porous nano-fiber mat (Weickgenannt et al., 2011).

To examine this hypothesis, experiments have been performed using a drop of destilled water impacting onto a heated substrate coated by a porous layer of solid particles, deposited by a preceding impact of a suspension drop. The presence of the deposited layer on the substrate indeed causes jetting and thermal atomization at $T_{\text{w0}} = 420\,^{\circ}\text{C}$ (corresponding to $\Delta T_{\text{w}} = 320\,^{\circ}\text{C}$) while the impact onto a clean substrate at the same impact conditions leads to

complete drop rebound. An example of the impact of a distilled water droplet on a residue is shown in Fig. 5.11.

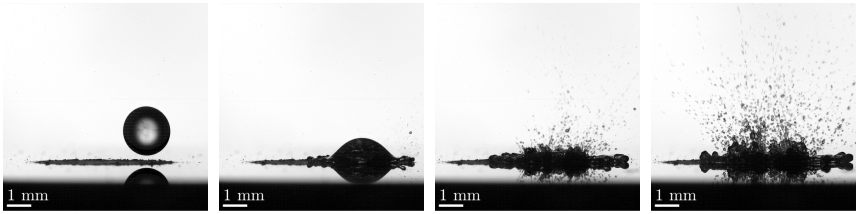

(a) $t = 0\,\mathrm{ms}$ **(b)** $t = 1\,\mathrm{ms}$ **(c)** $t = 1.33\,\mathrm{ms}$ **(d)** $t = 2.33\,\mathrm{ms}$

Figure 5.11: Distilled drop impact onto a heated substrate coated by a porous layer of solid particles, deposited by a preliminary impact of a suspension drop $\varphi = 2.57\,\%$ onto a hot substrate initially heated to the temperature $T_{\mathrm{w0}} = 420\,^{\circ}\mathrm{C}$. Solid residue induces jetting and thermal atomization of a water drop. The initial drop diameter is $d_0 = 2.1$ mm and impact velocity $U_0 = 1.7$ m/s.

In addition, Figure 5.10(a)-(d) shows the complete rebound of a distilled water droplet, impacting onto a clean substrate, under identical impact parameters and initial substrate temperature.

The second reason for the suppression of the drop rebound is the significant increase of the liquid viscosity due to the evaporation of the bulk liquid of the drop. Correspondingly, the critical temperature for drop rebound increases if the drop contains a particulate phase, as predicted by Eq. (5.20).

6 Single drop impact of a solution drop onto a hot substrate

Different regimes of solution drop impact on a hot substrate at a variety of substrate temperatures and impact conditions are presented in this chapter. These results are compared with those of suspension drop impact, presented in Chapter 5. Section 6.1 deals with observations related to the nucleate boiling regime. A brief description of the observed phenomena is presented along with drop residence time measurements. Section 6.2 contains observations related to higher wall temperatures associated with the thermal atomization and film boiling regimes. The influence of salts as a dissolved phase in the solution on the hydrodynamic and thermodynamic outcomes is discussed. Observations in this chapter serve as a basis for better interpretation of heat transfer during spray cooling performed with lubricant solutions in the Chapter 8. Parts of the present chapter, including text and figures, were previously published in Gajevic Joksimovic et al. (2023b).

6.1 Nucleate boiling regime

The process of nucleate boiling for pure, one-component liquids as well as for suspension drops has been described in previous chapters. The impact of solution drops in the nucleate boiling regime morphologically resembles to some extent the impact of suspension drops presented in Chapter 5. However, further analysis combined with residence time measurements also reveals quantitative differences. The impact of a solution drop onto a hot substrate at a temperature associated with the nucleate boiling regime is exemplified in Fig. 6.1. More details about the composition of the solutions and the dissolved phase they contain can be found in Section 3.2. The phenomena observed during boiling gradually approach water-like behavior with decrease in salt volume concentration φ (also referred to as "solution concentration" for

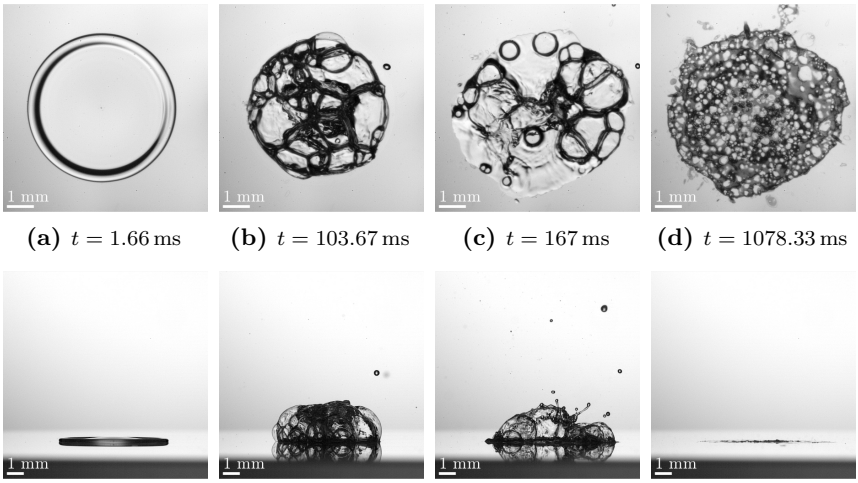

(a) $t = 1.66\,\mathrm{ms}$ **(b)** $t = 103.67\,\mathrm{ms}$ **(c)** $t = 167\,\mathrm{ms}$ **(d)** $t = 1078.33\,\mathrm{ms}$

(e) $t = 1.66\,\mathrm{ms}$ **(f)** $t = 103.67\,\mathrm{ms}$ **(g)** $t = 167\,\mathrm{ms}$ **(h)** $t = 1078.33\,\mathrm{ms}$

Figure 6.1: Simultaneous view of a solution drop impact $\varphi = 1.82\,\%$ on a transparent sapphire substrate in the nucleate boiling regime. (a)-(d) corresponds to the bottom view through the sapphire glass, while (e)-(h) corresponds to the side view of the same drop. Initial conditions are the same, including the initial substrate temperature $T_{\mathrm{w0}} = 150\,^{\circ}\mathrm{C}$, drop diameter $d_0 = 2.2$ mm and impact velocity $U_0 = 1.7$ m/s.

convenience), in particular foaming in the case of nucleate boiling (Breitenbach et al., 2017a; Breitenbach, 2019). As the amount of lubricant in the solution increases, foaming becomes so pronounced that nucleate boiling is referred to as "foaming boiling" in the case of lubricant solutions. For this reason, the effect of the dissolved phase is examined in more detail below.

6.1.1 Observations

Similar to suspension drops, after drop impact and liquid evaporation from the solution, a solid layer of the dissolved phase in the drop remains on the substrate. An example of such a solid deposit is shown in Fig. 6.1(d) and Fig. 6.1(h) from the bottom and side view, captured in the bottom-view setup configuration, introduced in Section 4.1.2. It is therefore necessary to

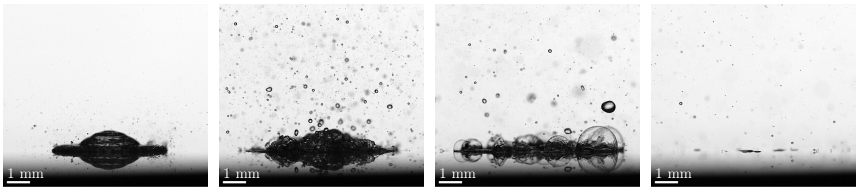

(a) Water, $\varphi = 0\,\%$: $t = 1.6\,\mathrm{ms}$ **(b)** $t = 12.1\,\mathrm{ms}$ **(c)** $t = 54.2\,\mathrm{ms}$ **(d)** $t = 195.3\,\mathrm{ms}$

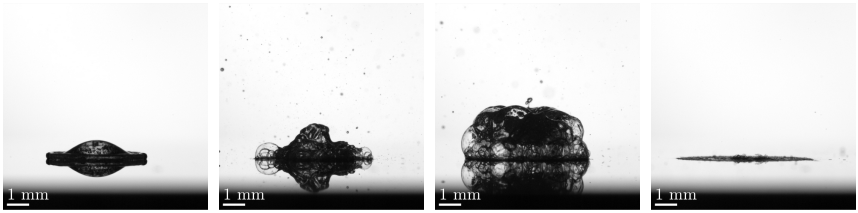

(e) Solution $\varphi = 2.74\,\%$: $t = 1.1\,\mathrm{ms}$ **(f)** $t = 14.3\,\mathrm{ms}$ **(g)** $t = 84.8\,\mathrm{ms}$ **(h)** $t = 893.1\,\mathrm{ms}$

Figure 6.2: Drop impact in the nucleate boiling regime. Effect of the solution concentration, $\varphi = 0\,\%$ (distilled water) (a)-(d), $\varphi = 2.74\,\%$ (e)-(h) on the evaporation and thermodynamic phenomena. The initial substrate temperature $T_{\mathrm{w0}} = 170\,^{\circ}\mathrm{C}$, drop diameter $d_0 = 2.2$ mm and impact velocity $U_0 = 1.33$ m/s are the same for both cases.

thoroughly clean the substrate before starting a new experiment and reheating the substrate. The cleaning procedure has already been described in Section 4.1.1.

In Fig. 6.2 examples of a drop impact of distilled water and a drop impact of a solution drop with a salt volumetric concentration of $\varphi = 2.74\,\%$ onto a substrate with an initial temperature of $T_{\mathrm{w0}} = 170\,^{\circ}\mathrm{C}$ are shown. In both cases, the impact is governed by nucleate boiling.

The separation of bubbles from the interface is suppressed, resulting in longer residence times of the drop on the substrate. The total evaporation time for a solution drop is about four times longer compared to pure water, as shown in Fig. 6.2(d) and Fig. 6.2(h). This effect can be explained by the decrease of the drop splashing rate due to the influence of the dissolved

phase, which is also consistent with the observations made for suspension drops, where the decrease of the splashing rate was described in Section 5.1.1. The boiling of sessile salt solution drops has been investigated by Cui et al. (2001), showing that in the temperature range related to nucleate boiling, the coalescence of bubbles is prevented by the presence of the dissolved phase. Additionally, the merging of rising bubbles is inhibited when the liquid film between the bubbles is stabilized with surfactant additives (Qiao & Chandra, 1997). The described mechanisms lead to an increase of the residual droplet mass evaporating on the substrate and thus to an increase of the residence time, as discussed in the following.

6.1.2 Residence time of an impacting solution drop

In order to characterize the influence of different salt volume concentrations (also referred to as "solution concentration" for convenience) on the impact of the solution drops, the residence time is measured. The complete derivation of the residence time equation (2.15) has already been shown in Section 5.1.3. The results for the range of wall overheat temperatures are shown in Fig. 6.3 in comparison with the residence time measurements for distilled water drops. Values of corresponding Reynolds numbers for obtained data vary from 3138 - 3071 where Re = 3138 corresponds to the largest solution concentration $\varphi = 3.28\,\%$, while Re = 3071 corresponds to the distilled water case. The range of Weber numbers is, accordingly, We = 68 − 57.

Foaming boiling is observed in the range of wall temperatures corresponding to $\Delta T_\mathrm{w} = T_\mathrm{w0} - T_\mathrm{sat}$ from 50 °C to 90 °C (see Fig. 6.3), analogous to the case of suspension drops considered in Section 5.1.3. Note that during foaming, the vapor bubbles grow much larger without coalescing so that the entire drop begins to foam and appears to inflate. This behavior results in longer residence times, especially for higher solution concentrations where this effect is more pronounced. However, the data for water and lower solution concentrations follow the predicted values from Eq. (2.15), scaling $t_\mathrm{r} \sim \Delta T_\mathrm{w}^{-2}$, same as in the case of suspension drops (see Section 5.1.3).

However, for higher ΔT_w, the slopes of the curves for all solution ratios fall to the lower plateau due to the intense rebound observed only for solution droplets in this temperature range. Thereby, the threshold of possible rebound occurrence is shifted to a lower temperature compared to the behavior of

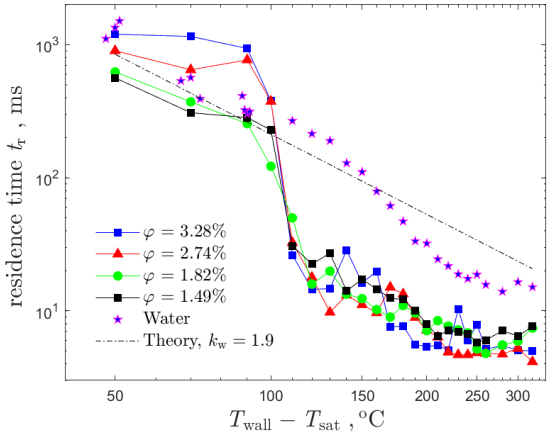

Figure 6.3: The residence time of the impacting drop as a function of the substrate overheat temperature for various solution concentrations in comparison with the theoretical predictions (Eq. 2.15). Drop diameter $d_0 = 2.3$ mm and impact velocity $U_0 = 1.33$ m/s are the same for all the cases.

suspension droplets in the same temperature range. Here, at the temperatures typically associated with the nucleate boiling regime for pure, one-component liquids (corresponding to $\Delta T_w = 90\,°C$), the impact of a solution drop at the same temperature almost always leads to partial rebound, as depicted in Fig. 6.4(h).

The reason for this solution drop behavior is not entirely clear. However, a recent study of Schmidt et al. (2023) on a distilled water drops revealed a similar behavior. Namely, as the surface temperature increases, nucleate boiling becomes more intense, with a higher mass of liquid being ejected in the form of secondary droplets. On the other hand, the emerging vapor bubbles begin to coalesce in the liquid film, resulting in large vapor clusters that separate a large volume of liquid from a thin liquid film on the substrate, as discussed in Section 5.2.1. The separated liquid continuously floats above the liquid film and is only connected to the liquid film by small liquid bridges, similar to the case of the solution drop in Fig. 6.4(g). The phenomenon is similar to a dancing drop on a hot substrate (Roisman et al.,

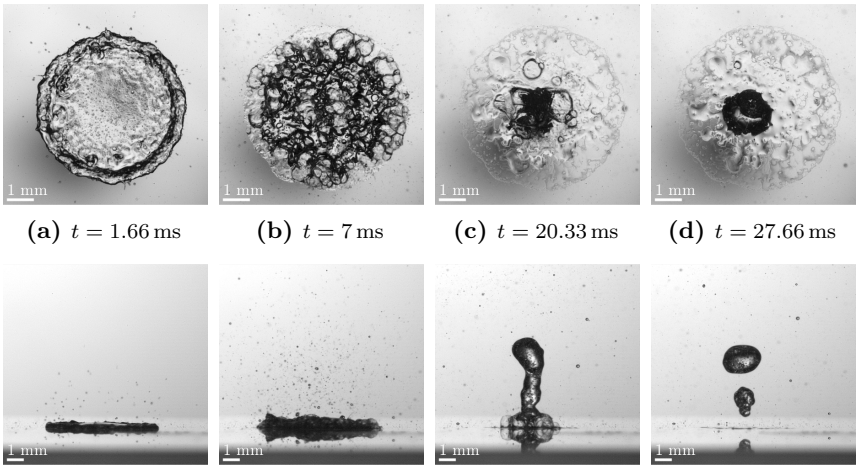

(a) $t = 1.66\,\mathrm{ms}$ **(b)** $t = 7\,\mathrm{ms}$ **(c)** $t = 20.33\,\mathrm{ms}$ **(d)** $t = 27.66\,\mathrm{ms}$

(e) $t = 1.66\,\mathrm{ms}$ **(f)** $t = 7\,\mathrm{ms}$ **(g)** $t = 20.33\,\mathrm{ms}$ **(h)** $t = 27.66\,\mathrm{ms}$

Figure 6.4: Simultaneous view of a solution drop impact $\varphi = 1.82\,\%$ on a transparent sapphire substrate in the transition boiling regime. (a)-(d) corresponds to the bottom view through the sapphire glass, while (e)-(h) corresponds to the side view of the same drop. Initial conditions are the same, including the initial substrate temperature $T_{\mathrm{w0}} = 190\,^{\circ}\mathrm{C}$, drop diameter $d_0 = 2.2$ mm and impact velocity $U_0 = 1.7$ m/s.

2018) and leads to a partial rebound, as shown in Fig. 6.4(h). At low surface temperatures, the separated liquid sometimes rejoins the liquid film and the observed phenomenon is repeated several times (Schmidt et al., 2023). Present observations are supported by Cui et al. (2001), who studied the behavior of salt solution droplets and found that the presence of salts in salt solution droplets induces the presence of a visibly larger number of bubbles whose coalescence is inhibited, leading to bubble bursting and complete droplet disintegration followed by rebound.

The difference in residence times between water droplets and solutions is most apparent in the range of wall temperatures corresponding to $\Delta T_{\mathrm{w}} = T_{\mathrm{w0}} - T_{\mathrm{sat}}$, from 100 °C to 170 °C, shown in Fig. 6.3. In this temperature range, transition boiling is typically observed for water and suspension droplets, as discussed in Section 5.1.3. Transition boiling of water drops can lead to partial

rebound, which is also observed with different solution concentrations over the entire mentioned temperature range. However, in the case of suspension drops, the residence time in the transition boiling regime increases without partial rebound being observed.

The variation of the residence time given by expression (2.15) can be implemented by adjusting the dimensionless parameter k_w, which accounts for effects caused by surface roughness or wettability for the substrate material used. It is assumed that it also accounts for the formation of the deposited layer from the dissolved phase in the droplet.

The dependence of k_w on the solution concentration is shown in Fig. 6.5. For larger solution concentrations, the value of the constant approaches the limiting value $k_w \approx 1.5$. For smaller values of φ, the constant k_w is obviously larger than the value $k_w = 1.9$ determined for water, implying that some of the effects caused by the boiling of the solution drop, are not fully captured by the use of the empirical constant. The exact mechanism leading to foaming and a detailed analysis of the related effects leading to this drop boiling regime are discussed and analyzed in Section 8.2.

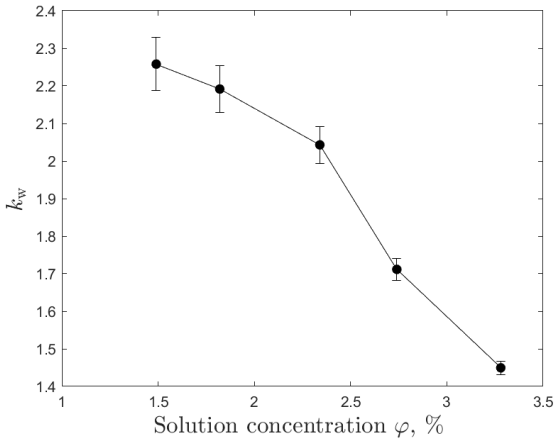

Figure 6.5: Dependence of the dimensionless empirical constant k_w, defined in Eq. (2.15), on the salt volume concentration φ in the solution. The error bars represent one standard deviation.

6.2 Higher wall temperatures: suppression of film boiling by dissolved phase

Above the wall temperature corresponding to $\Delta T_w \approx 170\,°C$ film boiling regime is observed for pure water drops. Examples of a drop impact onto a solid substrate initially heated to the temperature $T_{w0} = 420\,°C$ (corresponding to $\Delta T_w = 320\,°C$) are shown in Fig. 5.10 for distilled water and one solution concentration. Due to the film boiling phenomena, drop of distilled water undergoes a complete drop rebound, as shown in Fig. 6.6(a)-(d), while the solution drop shows completely different behavior, as shown in Fig. 6.6(e)-(h).

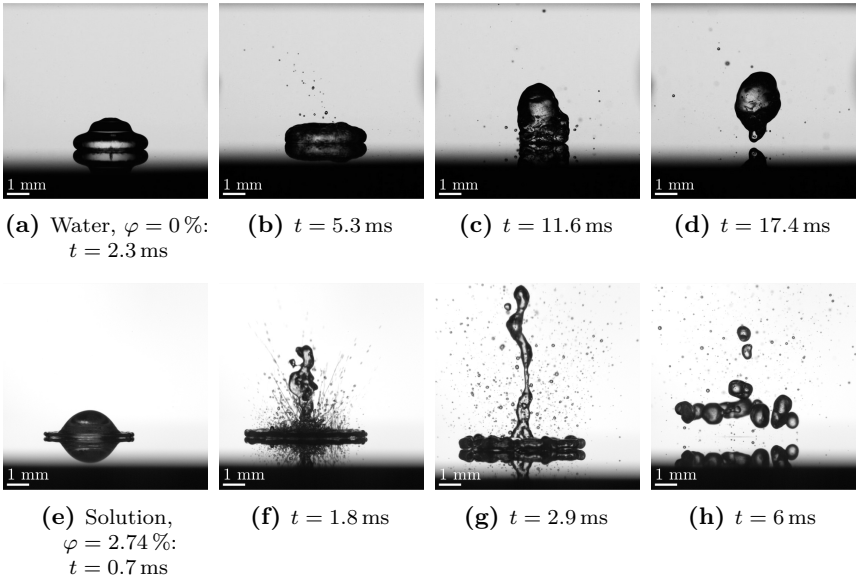

(a) Water, $\varphi = 0\,\%$: $t = 2.3\,\text{ms}$ **(b)** $t = 5.3\,\text{ms}$ **(c)** $t = 11.6\,\text{ms}$ **(d)** $t = 17.4\,\text{ms}$

(e) Solution, $\varphi = 2.74\,\%$: $t = 0.7\,\text{ms}$ **(f)** $t = 1.8\,\text{ms}$ **(g)** $t = 2.9\,\text{ms}$ **(h)** $t = 6\,\text{ms}$

Figure 6.6: Drop impact in the film boiling regime. Effect of the solution concentration, $\varphi = 0\,\%$ (distilled water) (a)-(d), $\varphi = 2.74\,\%$ (e)-(h) on the evident regime of the drop impact. The initial substrate temperature $T_{w0} = 420\,°C$, drop diameter $d_0 = 2.3$ mm and impact velocity $U_0 = 1.7$ m/s are the same for both cases.

In fact, when the solution drop comes into contact with a hot substrate at the exact same temperature, violent evaporation occurs, producing a vapor stream and a very strong local heat flux. This leads to the formation of multiple jets as shown in Fig. 6.6(f) or (g). The behavior is similar to the thermal atomization of pure, one-component liquid drops, where the impact velocity is so high that it ensures contact between the liquid and the substrate, even at very high temperatures, as described in Roisman et al. (2018). The main difference lies in the previously mentioned jetting phenomenon, which is specific to solution and suspension drops.

However, in the case of solution drops, rebound of the drop is prevented even at relatively low impact velocities, $U_0 \leq 1$ m/s. The underlying process is similar to that of suspension drops, described in Section 5.2.2. During the impact of a solution drop onto a hot substrate, intense liquid evaporation occurs mainly in the immediate vicinity of the substrate surface. The volatile component in the solution, which is water in the investigated cases, evaporates first. Water evaporation leads to a rapid local increase in the concentration of salts, which represent the dissolved phase in the solution, and even to salt crystallization. As a result, a solid residue is formed on the substrate.

The formation of such an accreted wet granular layer thus results in the pinning of the impacting drop, preventing it from rebounding. The salt residue effect is comparable to that of a particulate layer in the case of suspension drops (see Section 5.2.2). To test this assumption, additional experiments are performed in which, as a first step, a drop with a salt volume concentration of $\varphi = 2.74\%$ impacts a substrate initially heated to 170 °C. After the impact of a first drop and complete evaporation of the liquid, a solid deposit of the dissolved phase remains on the substrate. In the next step, the substrate was reheated to an indicative temperature associated with the film boiling regime - 420 °C (corresponding to $\Delta T_\mathrm{w} = 320$ °C) and a second pure water drop impact was performed on the deposit at the same impact velocity. The result of the impact is shown in Fig. 6.7.

Almost immediately after the impact, a violent evaporation occurs with an obvious disruption of the water drop lamella, indicating a thermal atomization regime. The deposited layer thus prevents the rebound of the boiling droplet, with the apparent migration of the boiling droplet to the far edge of the residue. The exact behaviour was observed for suspension drops, as mentioned in Section 5.2.2, with respect to Fig. 5.11.

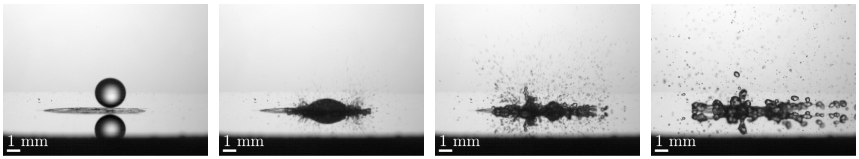

(a) $t = 0$ ms **(b)** $t = 0.66$ ms **(c)** $t = 1.33$ ms **(d)** $t = 3$ ms

Figure 6.7: Prevention of film boiling - different stages of induced thermal atomization regime of a distilled water drop impacting onto a solid deposited layer from the impact of solution $\varphi = 2.74\,\%$. The impact parameters are $d_0 = 2.2$ mm, impact velocity $U_0 = 1.7$ m/s and initial wall temperature 420 °C.

This solution drop behavior can be explained by the hydrophilic nature of the organic salts (Chen et al., 1995) forming the deposited layer, which represent a dissolved phase in the solution. The mechanism of suppression of film boiling is analogous to similar phenomena caused by porous nanofiber coatings (Weickgenannt et al., 2011). The suppression of the film boiling regime in the case of lubricant solutions is thoroughly investigated in Section 8.2.

Part II

Spray cooling by lubricant solution

7 Experimental methods for spray cooling study

This chapter describes the experimental methods used to study spray impact onto a hot substrate. In Section 7.1, the setup configuration is scrutinized in detail. Section 7.1.3 gives an insight into the mechanical construction and design of the heated target, while Section 7.1.4 describes the experimental procedure. The description of the measurement technique employed to acquire temperature values inside the substrate during spray cooling is the main focus of Section 7.2. This section also covers the procedure for calculating the heat flux and surface temperature. Some parts of the subsequent sections, including text and figures, have already been published in Gajevic Joksimovic et al. (2023a).

7.1 Overview of the spray cooling experimental setup

An experimental facility for observation and characterization of heat transfer due to spray impact onto a heated substrate is shown schematically in Fig. 7.1. The setup consists of four main systems, comprising a *spray generation system* connected to a fluid supply, a *heating system* with temperature measurement and control, an *observation system* with a high-speed camera and backlight illumination and a *computer control unit* for data acquisition and control of the experimental flow in LabVIEW software.

7.1.1 Spray generation

In Fig. 7.2 all the components involved in the spray generating process are presented. The mixture of water with industrial lubricant in exact desired ratio, thus achieving desired salt volume (solution) concentration, is stored

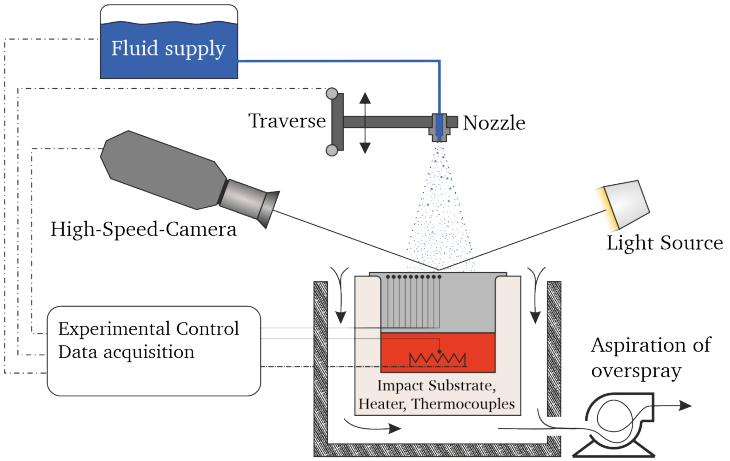

Figure 7.1: Schematic representation of the spray cooling experimental setup.

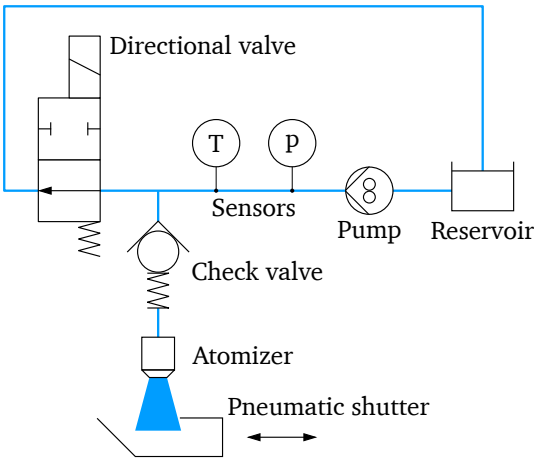

Figure 7.2: Schematic representation of the spray generation system. (Adapted from Tenzer (2020), licensed under CC BY-SA 4.0., © 2020 Fabian Tenzer.)

in a *reservoir*. If an elevated fluid temperature is required, the immersion heater connected to a temperature controller is used. Mostly, in the present experimental campaign, the working fluid remains at ambient temperature, due to the limited need for elevated fluid temperatures in the field of hot forging, introduced in Section 1.1. A one-component *atomizer* is driven by a *gear pump*, while corresponding fluid properties are measured by a *pressure and temperature sensor*. A *check valve* separates the atomizer from the main supply line. *A directional valve* connects the supply line to the recirculating line. Finally, a *movable shutter* is situated immediately beneath the atomizer opening. The shutter can deflect the entire spray coming out of the atomizer. It is driven by a pneumatic cylinder that instantly pushes the shutter into or out of the spray stream, thereby controlling the timing of the start of the experiment. This configuration ensures development of a stable, full cone spray on the substrate surface.

The spray is produced by a liquid driven commercial nozzle (*Lechler 490.403*), a full-cone, pressure swirl and one-component nozzle type. Different impact velocities of the spray droplets are achieved by varying the height of the spray above the hot substrate using a linear traverse, as shown in Fig. 7.1. By adjusting the distance between the nozzle and the heated surface, and by varying the pressure supplied to the nozzle, sprays of different impact properties can be generated. The nozzle has a bore (inner) diameter 1.25 mm,a spray angle 45° and operating pressure of 1.5 to 10 bar. The upper limit of operational pressure is, however, dictated by the maximum differential pressure of the gear pump. The spray has been characterized in terms of the drop size and velocity as a function of the liquid mass flow rate by Tenzer (2020) using the phase Doppler measurement technique. In order to measure a flow rate of the fluid passing through the atomizer, the Coriolis mass flow meter (*Optimass 7400 C*) from *Krohne* was installed.

7.1.2 Observation system

Due to the absence of quantitative outcomes from the visualization, a detailed description of the visualization system is excluded, and only a concise overview of the hardware is provided. The *observation system* consists of a CMOS high-speed camera equipped with two different lenses, either *Tamron* 180 mm macro optical lense or *Sigma* 150 mm macro optical lense, and a strong

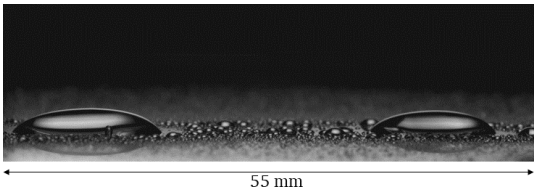

Figure 7.3: Example of a snapshot taken with a Tamron lense configuration. Field of view was 55 mm.

backlight illumination source. The camera *Vision Research Phantom v2012*, which can achieve a maximum resolution of 1280×800 pixels at 22000 fps, is used to record side view images and videos of the spray impact. The backlight illumination consists of a high-power light source (*Imaging Solutions*) and a diffuser plate. The illumination is placed behind the spray (and directed co-linearly with the high-speed camera), resulting in a shadowgraphy imaging.

An example image of the surface with a sprayed liquid, taken with a Tamron 180 mm objective, is shown in Fig. 7.3. The scale for the field of view is indicated below. Two configurations are used, resulting in a field of view of either 55 mm or 35 mm.

7.1.3 Design of a heated target

Two primary objectives related to the design of the heated target and surrounding housing are effective thermal insulation and watertight construction. Both are critical to allow complete flooding of the target and housing during spray experiments without damaging the internal components contained within. Damage to the components would cause the entire system to shut down. This would be unacceptable in the long run, considering that at least 300 experiments were performed, not counting cleaning experiments. In addition, as the target heats up, it undergoes thermal expansion, which means that the components in the housing must be able to withstand temperature up to 500 °C without breaking due to the force of thermal expansion. These challenges are overcome by a rather complicated design, which is described in more detail below. Additional information on the mechanical design can be found in Tenzer (2020). Before proceeding with the description of the construction and design, it should be noted that the terms ”impact target,”

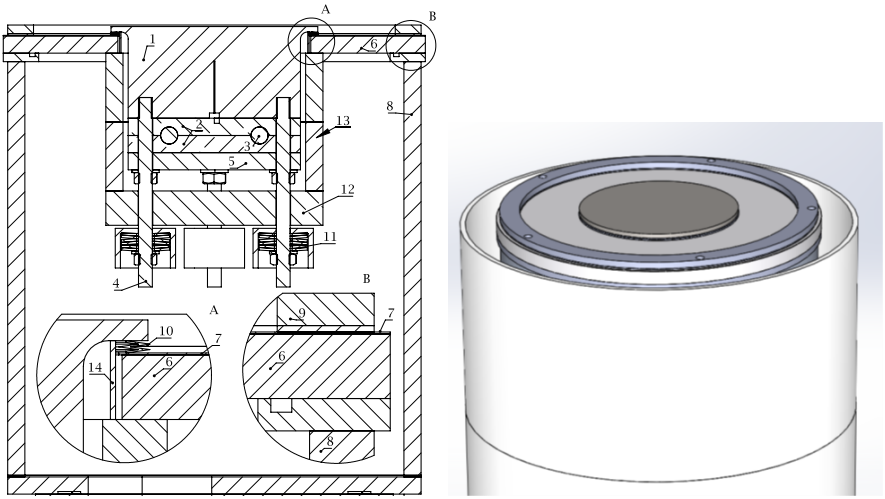

(a) Mechanical construction. **(b)** Housing with stainless steel target.

Figure 7.4: Heated substrate with all components numbered along with a 3-D representation of the housing. White outer cylinder represents ventilation slot. (Reprinted from Tenzer (2020), licensed under CC BY-SA 4.0., © 2020 Fabian Tenzer.)

"heated substrate," or "heated target" all refer to the same entity, the substrate exposed to the spray. Different terms are used depending on the context of the narrative, whether it is the "impact" of the spray or the spray cooling of a "heated" substrate. The setup is designed for surface temperatures up to a maximum of 500 °C.

The design of the heated target, which is a component of the *heating system* and its surrounding housing, is shown in Fig. 7.4. The heated target (1) is the top end of a circular cylinder (diameter $d_\mathrm{t} = 100$ mm and height $h_\mathrm{t} = 53.2$ mm). The material of the target is stainless steel with a mirror polished upper surface made by lapping and polishing. The average roughness of the polished surface is $< 0.03\,\mu$m. During the preliminary phase of the experimental campaign, stainless steel was found to exhibit a good resistance to both corrosion and oxidation, which resulted in it being selected for use. The target is heated by four cartridge heaters (3) (*hotset hotrod HHP*) with

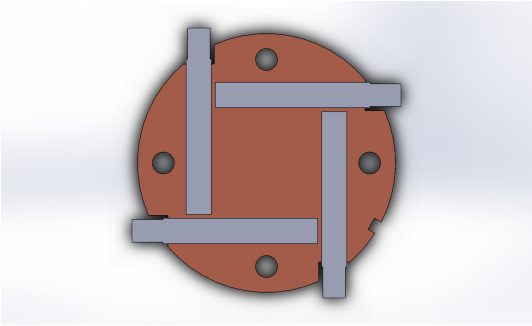

Figure 7.5: Copper heated cylinder with 4 cartridge heaters arranged in a rectangular pattern.

an overall power of 2 kW, placed inside the copper cylinder (2), as shown in Fig. 7.5. In addition, a thermocouple is placed inside the copper cylinder and its temperature reading is used as an input value for adjusting the heating power in the controller in the LabVIEW environment. To ensure good contact between the cartridge heaters and the target over the entire copper cylinder surface, four threaded rods (4) are used to attach the bottom of the heated target to the copper cylinder. Since copper is known to be a rather soft metal, a stainless steel plate (5) is placed underneath to evenly distribute the force and secure the copper cylinder. The target is also enclosed by a fiber cement plate (6), made of fiber cement (*Kelux Kelutherm 700*) with a low thermal conductivity of 0.38 W/mK, to maximally reduce thermal energy loss from the housing. In addition, the plate is covered with a 0.3 mm thick stainless steel sheet (7), which is neatly fastened to prevent penetration of the sprayed liquid into the cement plate. On the outside, the fiber cement plate and the stainless steel plate are bolted to the aluminum outer cylinder (8). The free space inside the aluminum cylinder (8) is filled with *Insulfrax S* insulation material. In addition, argon gas from *Air Liquide* is pumped inside the aluminum cylinder to protect the heater (copper cylinder (2)) from oxidation, thus prolonging its operating time. Next, an aluminum ring (9) is installed at the top of the aluminum outer cylinder to evenly distribute the pressure of the screws (note the blue ring in Fig. 7.4b). A metal seal (10) is installed between the target and the stainless steel cover to make this

interface watertight. The seal is a high temperature metallic "E-Ring" type duct seal. It has the advantage of not requiring high sealing forces. Installed beneath the heated target are high temperature disc springs (11) supplied by *Vinsco Spring Limited*. These springs provide a constant sealing force regardless of thermal expansion by acting as an intermediary between the threaded rods (4) and a compression structure. The compression structure consists of a plate (12) made of *Kelutherm 800 M* and two hollow cylinders (13) made of *Kelutherm 700*. A spacer (14) is used to limit the compression of the seal within its operating range. This design allows the insulation material to be subjected to pressure only, leaving the heated components to freely expand and contract.

7.1.4 Experimental procedure

Experimental procedure for each experiment is briefly described below.

First, the target is heated until a uniform initial temperature of 445 °C is reached. Heating is stopped immediately after the start of spraying. For the specific nozzle used in this experimental campaign (described in Section 7.1.1), the produced spray is unstable during the first 10 seconds, with large liquid ligaments present. In order to deflect the spray liquid during this time, a pneumatic shutter receives a signal to move into the stream and collect the liquid coming out of the nozzle. Fig. 7.2 illustrates the operation principle of the shutter. After 10 seconds, the shutter is moved out of the stream by a pneumatic cylinder.

Only once the spray is fully developed and the target is uniformly heated does the experiment begin. Visualization and heat flux measurements are temporally matched, allowing visual observations to be directly related to instantaneous local heat flux and target surface temperature.

After each spray experiment is completed, a solid residue forms on the substrate, due to the presence of organic salts and surfactants in the lubricant liquid. For high substrate wall temperatures, after water evaporation, deposition of the mentioned components occurs. In order to start the next experiment with the same experimental conditions as the previous one, the substrate surface needs to be thoroughly cleaned. For that purpose, an additional reservoir with a mixture of water and isopropanol is connected with mini-ball valves to a supply line (not presented in Fig. 7.2). Given that

organic salts, which are the main component of the lubricant (as described in Section 3.2), are completely dissolved in water, the aforementioned mixture was chosen as the cleaning liquid. During the cleaning process, the mini-ball valves downstream of the cleaning tank are opened in order to supply only the cleaning liquid to the whole system. After thoroughly cleaning the substrate, the visual appearance was checked to identify possible stains or damage to the surface. After completing all experiments for the day and cooling to room temperature, the surface was cleaned once again using distilled water. Next, the impact surface was polished with a mirror polishing paste to attain an average roughness of 0.03 µm. Finally, isopropanol alcohol was employed to remove polish residues. Cleaning the surface ensured good repeatability, which was confirmed by repeating the experiments with the same parameters.

7.2 Measurement technique for heat flux and surface temperature

In order to evaluate both temperature and heat flux on the surface of the target, the inverse heat conduction problem (IHCP) (Monde et al., 2003) needs to be solved by using the temperature readings from inside the substrate as input data. The temperature readings are acquired from thermocouples embedded into the target. In Fig. 7.6 the position of the thermocouples is shown. The thermocouples are arranged in two rows. The first row is located 0.5 mm below the surface to achieve a quick response time. The holes, inside which the thermocouples are placed, are produced using the spark erosion technique. The resulting hole diameter is 0.6 mm. The thermocouples are bonded inside the holes using a highly thermally conductive adhesive (*Aremco Ceramabond 569 VFG*) to ensure good thermal contact. Temperatures are sampled at a sample rate of 95 Hz using *National Instruments NI 9212* thermocouple input modules attached to a *National Instruments cRio 9074*.

The radial distance between each sensor in the first row is 3.5 mm to account for radial distribution of the heat flux. The second row, consisting of two thermocouples, is positioned 20 mm below the surface to make the IHCP procedure independent of the boundary condition at the bottom of the target. The heat flux problem is assumed to be two-dimensional, axisymmetric and having adiabatic boundary conditions at the curved surface. It is, therefore,

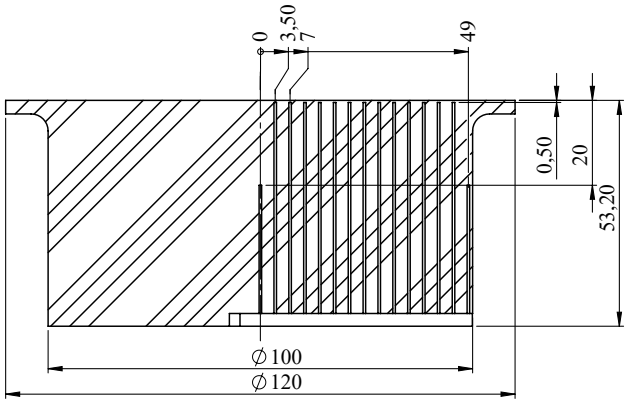

Figure 7.6: Sectional view of the heated target showing the thermocouple positions. Dimensions are in mm.

assumed, that the heat transfer occurs only through the top surface exposed to spray.

The thermocouples are type K, class 1, with 0.5 mm shield diameter. The measuring tip is open and aligned with the shield. This configuration ensures the shortest possible response time for this type of thermocouples. The response time of the thermocouples was measured, yielding 0.7 seconds. Such response time makes it problematic to accurately follow the sharp jumps of the temperature and to measure the precise values of heat flux near sharp peaks, for example in the region of critical heat flux. Therefore, the measurements can be considered reliable over the entire measurement range, except for this region. This was confirmed by comparing the measured heat flux of the present study with the predicted value from direct numerical simulations of heat conduction in the wall using a commercial code. The code has been recently developed by the project partner **TRANSVALOR S.A** and will be available only to companies in the forging industry.

In the present work, an existing algorithm (Monde et al., 2003; Woodfield et al., 2006), developed into an inverse heat conduction analysis tool "Invers2D", is used to calculate the heat flux and the target temperature at the wall surface from the temperature readings of the thermocouples. This tool has been developed and made available from Monde and co-workers at

Saga University. Initially, the two-dimensional heat conduction problem is transformed from polar-cylindrical coordinate system to the Laplace space. Measured temperature inside the target is approximated as a series of half power polynomials in time, and as Fourier-Bessel series in space. After solving the problem in Laplace space, an inverse Laplace transform leads to the solution. The procedure is described in detail in Woodfield et al. (2006).

From the analysis of the uncertainty in the inverse heat transfer estimations, the inverse heat transfer solution from Woodfield et al. (2006) can be interpreted as a spatio-temporal average of the actual heat transfer variation with a time resolution of approximately 0.1 seconds, which is the smallest time interval over which changes in the system can be reliably detected and resolved in the analysis (Karwa, 2012). In addition, the thermal properties of the target material are assumed to be constant and therefore unaffected by temperature changes. This greatly simplifies the mathematical modeling and computational effort required to solve the problem. However, the assumption of constant thermal properties at different temperatures leads to the prediction error of up to $\pm 20\%$ over a surface temperature range of $300\,^{\circ}\mathrm{C} - 900\,^{\circ}\mathrm{C}$ in comparison with the case with variable thermal properties (Karwa, 2012). This error is within the range of variation of the thermal effusivity over the same temperature range. Furthermore, a detailed analysis of the uncertainty in the estimation of the surface heat transfer by the method published in Monde et al. (2003) and Woodfield et al. (2006) and used in this work is discussed in detail and given in Karwa (2012).

8 Heat transfer by spray impact

This chapter presents the experimental results of the study on spray cooling using lubricant solutions. First, Section 8.1 illustrates the evolution of heat flux and substrate wall temperature during the spray cooling process. These results are then correlated with visualizations of the hydrodynamics observed during the spray impact of a lubricant solution on a hot substrate. In addition, Section 8.2 examines the influence of additives on heat transfer, specifically their influence on the Leidenfrost point and the suppression of film boiling. Certain parts of this chapter, including text and figures, have already been published in Gajevic Joksimovic et al. (2023a).

8.1 Influence of additives on the heat transfer

Experiments in this study were performed with different lubricant-to-water mixture ratios, thus achieving various lubricant solution concentrations (also referred to as "salt volumetric concentrations"), as already emphasized in Section 3.2. Additional experiments with the same operational parameters were carried out with a distilled water spray, for comparison purposes. To evaluate the boiling curve in many heat transfer studies, setup configurations are usually designed to keep the substrate temperature constant. However, in the present case, in order to evaluate effects of transient phenomena during spray cooling and simultaneous lubrication of the contact surfaces, the heated target temperature is kept constant only until the beginning of spraying. The entire experimental procedure is discussed in Section 7.1.4.

The spray parameters at the spray axis are the same for all the experiments in this study: mean drop diameter $D_{10} = 78.7\,\mu\text{m}$, mean impact velocity $U = 14.05$ m/s and mass flux $\dot{m} = 2.50$ kg/m^{2}s. The mass flow of the nozzle is $\dot{M} = 62.1$ kg/h. Experiments were conducted at a supply pressure of 2 bars and with an nozzle-to-target distance of 300 mm. To maintain the same spray parameters, the distance and supply pressure were kept constant

throughout the whole campaign. After each experiment, a cleaning liquid is used to remove the solid residue on the substrate, ensuring consistent surface conditions for subsequent experiments, as already described in Section 7.1.4.

8.1.1 Evolution of the heat flux and the wall temperature during spray cooling

In Fig. 8.1, the results of the measurements of the heat flux $\dot{q}$ and the substrate interface temperature T during water spray impact onto a hot substrate, initially heated to 445 °C, are shown as a function of time t. Uncertainty discussion for heat flux and surface temperature calculations is already covered in Section 7.2 and is therefore not addressed here. The temporal evolution of $\dot{q}$ and T are determined by the instantaneous local thermodynamic regime. In these experiments the film boiling regime switches to the transition boiling regime at the time instant t_{L} corresponding to the Leidenfrost point $T_{\mathrm{Leidenfrost}}$ at which the heat flux $\dot{q}$ is minimum. In the transition boiling regime the heat flux quickly rises and reaches the critical heat flux. Next, the evolution of the heat flux is governed by the heat transfer in the nucleate boiling regime. The results shown in Fig. 8.1 are in agreement to existing measurements for distilled water (Tenzer et al., 2019).

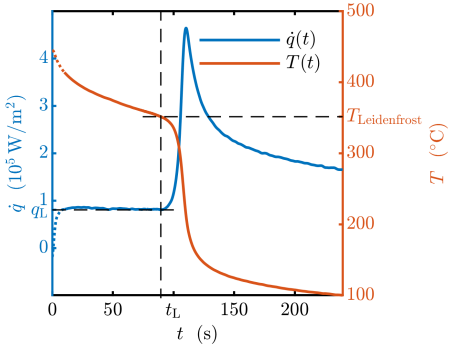

Figure 8.1: Heat flux and temperature at the spray and target axis at the wall surface as a function of time for spray cooling by distilled water. Initial substrate temperature was $T_{\mathrm{w0}} = 445°$ C. The spray parameters are: mean drop diameter $D_{10} = 78.7\,\mu$m, mean impact velocity $U = 14.05$ m/s and mass flux $\dot{m} = 2.50$ kg/m^{2}s.

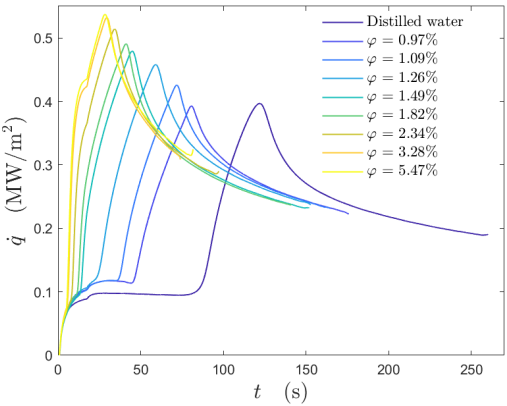

(a) Temporal evolution of the heat flux for different volume concentrations.

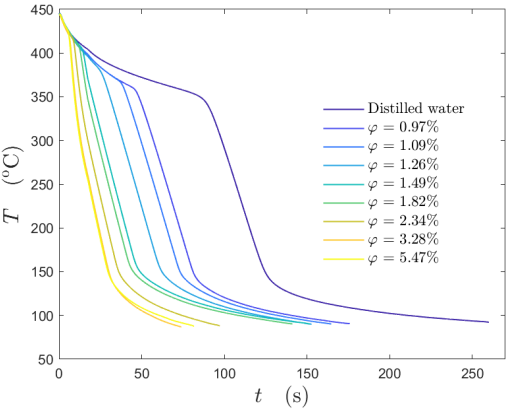

(b) Temporal evolution of the substrate interface temperature for different volume concentrations.

Figure 8.2: Temperature and heat flux at the spray and target axis at the wall surface as a function of time during spray cooling for different volume concentrations of lubricant solutions. Initial wall temperature was $T_{w0} = 445\,°C$. The spray parameters are: mean drop diameter $D_{10} = 78.7\,\mu m$, mean impact velocity $U = 14.05$ m/s and mass flux $\dot{m} = 2.50$ kg/m^{2}s.

The effect of lubricant addition on the evolution of heat flux and substrate surface temperature is shown in Fig. 8.2 for various solution concentrations. The addition of even a small amount of lubricant results in significant quantitative changes. As the solution concentration increases, the local heat flux, the value of critical heat flux and the Leidenfrost point $T_{\text{Leidenfrost}}$ increase. In Fig. 8.3, the dependence of the boiling curves of a lubricant solution $\varphi = 1.49\,\%$ is shown for different initial wall temperatures. With the increase of wall overheat temperature, different physical mechanisms act on the surface, leading to a substantial increase in heat flux, as will be described in the subsequent section.

The significant changes in the values of heat flux shown in Figs. 8.2 and 8.3 cannot be explained only by the variations of the thermal properties of the liquids. It seems that the addition of the lubricants leads to the emergence of the new physical processes, which will be investigated below.

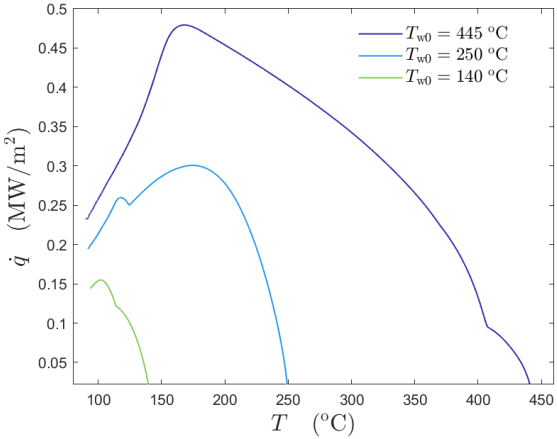

Figure 8.3: Comparison of the boiling curves of a lubricant solution $\varphi = 1.49\,\%$ for different initial substrate temperatures: $T_{w0} = 140\,°C$, $T_{w0} = 250\,°C$ and $T_{w0} = 445\,°C$. The spray parameters are: mean drop diameter $D_{10} = 78.7\,\mu m$, mean impact velocity $U = 14.05$ m/s and mass flux $\dot{m} = 2.50$ kg/m^{2}s.

8.1.2 Phenomena of spray impact onto a hot substrate

To better understand the physical reasons for the strong effect of the additives on the heat flux and on the thermodynamic regimes of spray impact, the phenomena have been observed using a high-speed visualization system, described in Section 7.1.2. The results of observations of pure water spray and lubricant solutions are shown in Fig. 8.4. Exemplary snapshots were taken at the surface temperature 280 °C. The observations in Fig. 8.4a for the impact of a distilled water spray correspond to the typical fully developed nucleate boiling regime. The same phenomena have been observed also in the recent experiments on spray cooling by distilled water (Tenzer et al., 2019). On the contrary, the observations for the lubricant solutions in Figs. 8.4b and 8.4c are completely different. The impact is accompanied by an intensive formation and expansion of a relatively thick foam layer. This phenomenon is most probably the main reason for the increase of the heat flux by addition of the lubricants to the sprayed liquid, as already shown in Fig. 8.2 for different solution concentrations.

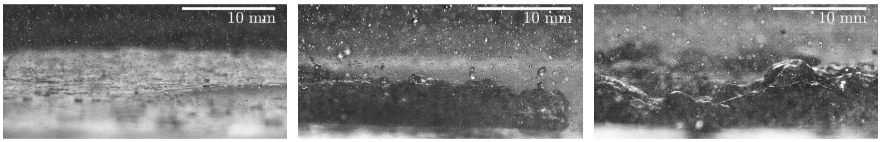

(a) $\varphi = 0\,\%$ **(b)** $\varphi = 1.09\,\%$ **(c)** $\varphi = 3.28\,\%$

Figure 8.4: Shadowgraphy visualizations of observed phenomena for $\varphi = 0\,\%$ (distilled water), $\varphi = 1.09\,\%$ and $\varphi = 3.28\,\%$. The spray parameters are: mean drop diameter $D_{10} = 78.7\,\mu\text{m}$, mean impact velocity $U = 14.05$ m/s and mass flux $\dot{m} = 2.50$ kg/m^{2}s. Initial wall temperature was $T_{w0} = 445$ °C. Snapshots were taken at surface temperature $T = 280$ °C.

The appearance and formation of the foam layer at different initial wall temperatures is shown in Fig. 8.5. In all cases, the first stable bubbles are created by initial drop impacts and their nucleate boiling at the surface. Over time, the number of bubbles increase. As the bubbles coalesce, they form a stable cellular structure consisting of pockets of vapor trapped within a thin film of liquid. This structure will be referred to as a foam. The observations (correlated with different initial wall temperatures) in Fig. 8.5 correspond to

the boiling curves shown in Fig. 8.3.

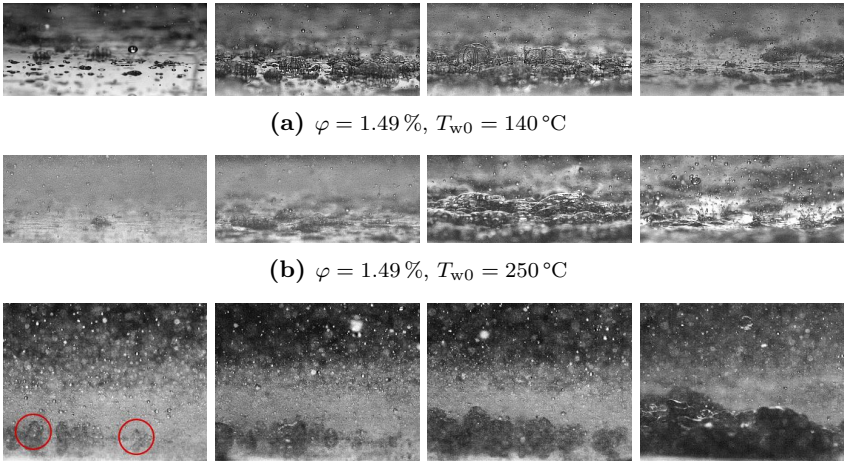

(a) $\varphi = 1.49\,\%$, $T_{w0} = 140\,°C$

(b) $\varphi = 1.49\,\%$, $T_{w0} = 250\,°C$

(c) $\varphi = 2.34\,\%$, $T_{w0} = 445\,°C$

Figure 8.5: Observations of the phenomena associated with spray cooling using lubricant solutions $\varphi = 1.49\,\%$ and $\varphi = 2.34\,\%$ for different initial wall temperatures through time. The development of a foam layer can be clearly seen at all the initial temperatures. Red circles indicate the appearance of the first foam bubbles on the substrate. The spray parameters are: mean drop diameter $D_{10} = 78.7\,\mu m$, mean impact velocity $U = 14.05$ m/s and mass flux $\dot{m} = 2.50$ kg/m^{2}s.

Now, evolution of the heat flux associated with spray cooling can be explained by comparing boiling curves for distilled water and for lubricant solution, as shown in Fig. 8.6. This comparison highlights the strong differences between the different regions of the boiling curves of the two liquids. These differences are primarily associated with the intensive liquid foaming of the lubricant solutions (as indicated in Fig. 8.6).

The expansion of the foam in the liquid film on the target results in an increase in heat transfer due to the increase in effective surface area. This leads to a significant improvement in cooling efficiency and an increase in the heat flux (refer to the orange curve in Fig. 8.6), ultimately reaching the critical heat flux point. After reaching CHF and with still continuous spray deposition, breakage of a foaming layer occurs. However, even at low

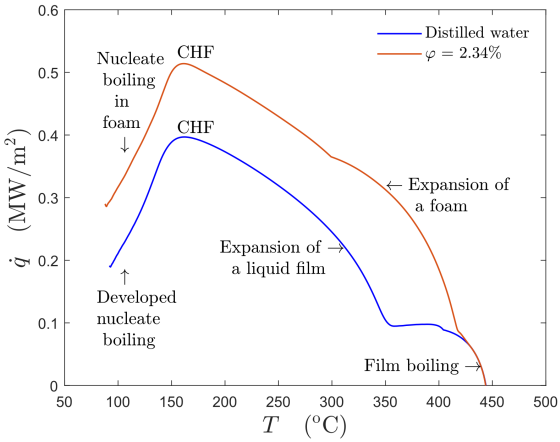

Figure 8.6: Comparison of boiling curves for distilled water and a lubricant solution $\varphi = 2.34\,\%$ for the same initial substrate temperature $T_{w0} = 445\,°C$. The spray parameters are: mean drop diameter $D_{10} = 78.7\,\mu m$, mean impact velocity $U = 14.05$ m/s and mass flux $\dot{m} = 2.50$ kg/m^{2}s.

temperatures near saturation temperature, foam is still present as the part of a liquid layer.

8.2 Film boiling suppression by lubricant addition

In the experiments, shown in Fig. 8.2b, the values of the Leidenfrost point increase from approximately 340 °C for distilled water to 420 °C for the lubricant solution $\varphi = 5.47\,\%$. The effect of salt and surfactant additives on the heat transfer during spray cooling has also been observed in the literature (Qiao & Chandra, 1998; Zhang et al., 2018; Ravikumar et al., 2014a; Liu et al., 2021; Abdalrahman et al., 2014). However, it is interesting to understand the mechanism leading to the shift of the Leidenfrost point. The following will be discussed below, with a single drop impact as the starting point.

Upon impact of a single drop on a hot substrate, the temperature exceeding the saturation temperature of the liquid, a number of vapor bubbles are formed

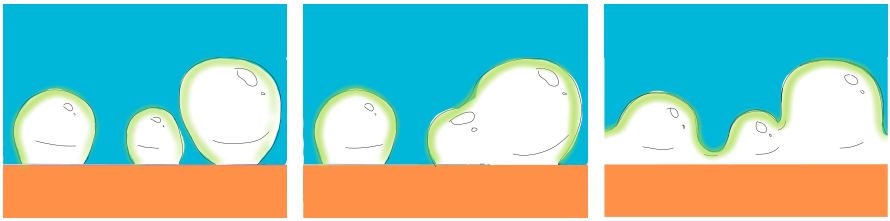

(a) Bubble formation **(b)** Coalescence **(c)** Percolation

Figure 8.7: Sketch of (a) the nucleation of the vapor bubbles, (b) their random coalescence, leading to the formation and expansion of the vapor channels, and (c) subsequent vapor channels percolation. If the time for channels' percolation is smaller than the spreading time t_ν, the consequent drop receding leads to the drop rebound.

at the interface after a certain bubble waiting time (delay time) (Carey, 2020), as already discussed in Section 2.2.1. The intensive formation of the bubbles leads to the prevention of the drop receding. At some instant, the volume concentration of the vapor phase reaches the percolation threshold of the liquid phase, associated with the bubble coalescence leading to the formation of vapor channels, as schematically shown in Fig. 8.7. This instant is estimated in Schmidt et al. (2021b) from the energy balance in the form

$$t_{\text{percolation}} \sim \left[\frac{h_\nu L^* \rho_l}{e_{\text{w}}(T_{\text{w0}} - T_{\text{sat}})}\right]^2, \tag{8.1}$$

where L^* is the sum of the latent heat of evaporation L and the enthalpy difference between the initial drop and saturated liquid, ρ_l is the density of the liquid.

If the percolation time $t_{\text{percolation}}$ is smaller than the spreading time, denoted as t_ν, the drop boiling is influenced by the formation of vapor channels, which do not prevent the drop from receding, unlike what happened in the bubble expansion regime. Drop spreading and the resulting lamella thickness h_ν are discussed in Section 2.1. The condition $t_{\text{percolation}} < t_\nu$ determines therefore the drop rebound temperature (Schmidt et al., 2021b)

$$\Delta T_{\text{rebound}} \sim \frac{\rho_l \sqrt{\nu} L^*}{e_{\text{w}}}, \quad \Delta T_{\text{rebound}} = T_{\text{rebound}} - T_{\text{sat}}, \tag{8.2}$$

which is linearly proportional to the Leidenfrost temperature $T_{\text{Leidenfrost}}$ for spray impact over a wide range of impact parameters and substrate properties. Eq. (8.2) cannot be directly applied to the description of the Leidenfrost point of multicomponent liquids since the viscosity of these changes during the drop evaporation, leading to the increase of the concentration of the dispersed or dissolved phase. At the temperature associated with the drop thermal rebound, the relative volume of the liquid phase reduces to the percolation threshold $\epsilon_c \approx 0.32$. Therefore, the average solution concentration at the instant of vapor percolation can be estimated as:

$$\varphi_{\text{rebound}} \approx \frac{\varphi}{\epsilon_c} \approx 3.12\varphi. \tag{8.3}$$

To examine the effect of lubricant solutions on the value of the Leidenfrost temperature, a dimensionless number is introduced

$$\omega \equiv \frac{\Delta T_{\text{rebound}}}{\Delta T_{\text{rebound,water}}}, \tag{8.4}$$

where $\Delta T_{\text{rebound,water}}$ is based on the Leidenfrost point of distilled water. The measurements of ω are shown in Fig. 8.8 for various concentrations of the lubricant solutions. These results are compared with the experimental data for Leidenfrost point (Huang & Carey, 2007; Kumar et al., 2020) for NaCl solutions obtained using the observations of the boiling of a liquid near the surface of a heated immersed metal ball. These results are rather close to the data from the present study, which indicates the independence of the phenomena associated with the spray impact. Additionally, the data by Abdalrahman et al. (2014) for $MgSO_4$ salt solutions are shown in Fig. 8.8, indicating much stronger effect of $MgSO_4$ on the value of the Leidenfrost temperature. The results for ω are also compared with the theoretical predictions $\omega_{\nu\text{NaCl}}$, which can be estimated for the same substrate with the help of the expression (8.2):

$$\omega_{\nu\text{NaCl}} = \frac{\rho_l \sqrt{\nu_{\text{NaCl}}}}{\rho_{\text{water}} \sqrt{\nu_{\text{water}}}}. \tag{8.5}$$

The viscosity ν_{NaCl} of the mixture is determined from the existing database for NaCl solutions (Kestin et al., 1981) for the solution concentration φ_{rebound} defined in Eq. (8.3). The theoretical predictions agree well with the measurements only for the smallest concentrations $\varphi < 1\%$. For larger salt volume

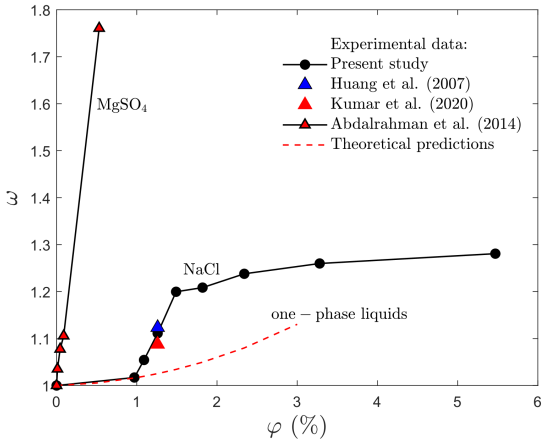

Figure 8.8: Dependence of the dimensionless number ω, defined in Eq. (8.4) on the lubricant solution concentration φ in comparison with the experimental data for NaCl (Huang & Carey, 2007; Kumar et al., 2020), $MgSO_4$ (Abdalrahman et al., 2014) and with the theoretical estimation (Eq. 8.5), developed for one-phase liquids.

concentrations, the deviation of the measurements and the theory, developed for one-phase liquids, becomes significant. This deviation indicates that there are some physical phenomena or processes involved that become dominant only for the multicomponent liquids and are minor for a pure, one-component liquid.

In order to distinguish the exact influence of the salts from the other additives present in the lubricant solution on the overall process and the value of the Leidenfrost point, additional experiments were carried out with the commonly used salts. Prior to spray cooling, the salts were dissolved in distilled water. For comparison, the same volumetric concentrations of salts from the lubricant campaign were used in the salt solution experiments, with volumetric salt concentrations ranging from $\varphi = 0.97\,\%$ to $\varphi = 5.47\,\%$. Salt solutions were prepared by dissolving commercially available powdered sodium chloride NaCl with a purity of $\geq 99.5\%$ in distilled water. After preparation and prior to use in the spray system, the salt solutions were stirred to ensure complete mixing. Experiments with NaCl solutions revealed

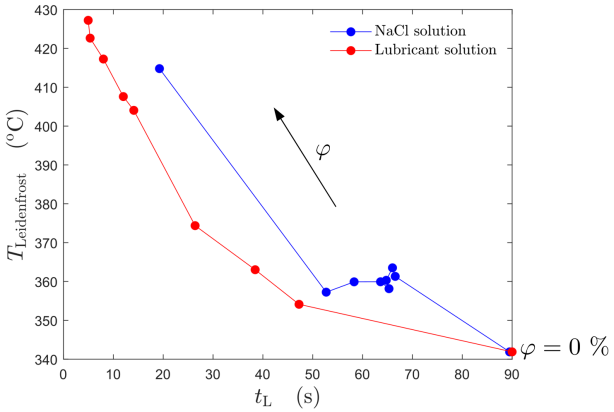

Figure 8.9: The Leidenfrost temperature $T_{\text{Leidenfrost}}$ as a function of the time at which the Leidenfrost point is reached t_{L} for the whole range of lubricant solution concentrations and NaCl concentrations φ. The arrow indicates in which direction φ increases. The initial substrate temperature is $T_{\text{w0}} = 445\,°\text{C}$. The spray parameters are: mean drop diameter $D_{10} = 78.7\,\mu\text{m}$, mean impact velocity $U = 14.05$ m/s and mass flux $\dot{m} = 2.50$ kg/m^{2}s.

interesting behavior. The dependence of the Leidenfrost temperature on the time required to reach the Leidenfrost point for both lubricant and NaCl solutions is shown in Fig. 8.9. The effect of adding salts to pure water (note the blue curve in Fig. 8.9), without any additional additives, causes a delay in the Leidenfrost point compared to the pure water case. The values corresponding to the pure water case are $t_{\text{L}} = 90\,\text{s}$ and $T_{\text{Leidenfrost}} \approx 340\,°\text{C}$, respectively (see the annotation $\varphi = 0\%$ in Fig. 8.9, corresponding to the pure water case). In fact, as can be clearly seen in Fig. 8.9, both salt and lubricant additives influence the whole process and the shift of the Leidenfrost point, although the influence is greater for lubricant solutions due to the presence of additional additives besides salts. Therefore, as the initial volumetric concentration increases, the slope of the curve is steeper for lubricant solutions. Now, the deviation between the measurements and the theory developed for one-phase liquids shown in Fig. 8.8, as well as the differences in the Leidenfrost point values shown in Fig. 8.9, can be attributed to specific phenomena such as foaming and significant changes in substrate wettability. The processes

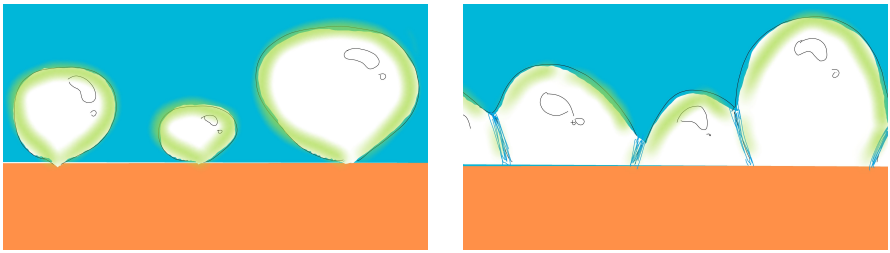

(a) Effect of the substrate wettability **(b)** Prevention of bubbles coalescence

Figure 8.10: Sketch of the two major mechanisms leading to a significant change of the value of the percolation time and therefore of the Leidenfrost point: (a) increase of the wettability of the substrate after evaporation of the previous lubricant drops in the impacting spray; (b) presence of the surfactants and salts in the lubricant solution prevent the bubbles' coalescence by formation a stable separating film between bubbles. The latter not only increases the percolation time, but also leads to the formation of foam.

associated with these phenomena are shown schematically in Fig. 8.10.

The first influencing factor is caused by the formation of a hydrophilic spot after impact and evaporation of the first drops in the spray. The formation of these hydrophilic spots has been observed during a series of consecutive impacts of liquid lubricant solution drops onto a hot substrate. To illustrate this behavior, additional experiments were performed, as described below. Following the impact of a solution drop, a solid deposited layer remains on the substrate. Next, the impact point of the second, pure water drop was shifted from the center of the deposited layer. It impacts onto an edge of the deposit. The outcome of the impact is shown in Fig. 8.11. Almost immediately, the boiling drop migrates from the edges of the layer towards its center, due to the hydrophilic nature of the organic salts forming the deposited layer (Chen et al., 1995).

This leads to the decrease of the projected area of the bubbles on the wall surface, even if the volume of the bubbles remains the same. Correspondingly, the time required to achieve the percolation threshold for the bubbles increases, and thus the Leidenfrost point. The bubbles on the hydrophilic spot are shown schematically in Fig. 8.10a.

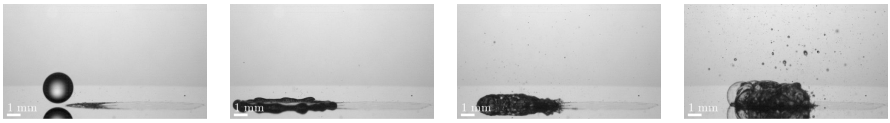

(a) $t = 0$ ms **(b)** $t = 2.9$ ms **(c)** $t = 16.0$ ms **(d)** $t = 75.5$ ms

Figure 8.11: Different stages of the impact of a distilled water drop onto a solid deposited layer from the impact of solution $\varphi = 2.34\,\%$. The impact parameters are $d_0 = 2.2$ mm, impact velocity $U_0 = 1.7$ m/s and initial wall temperature 170 °C.

The second major mechanism for shifting the Leidenfrost point, also identified as the cause of foam formation, is related to the presence of surfactants and salts dissolved in the lubricant. They prevent bubble coalescence, as shown in the sketch in Fig. 8.10b, and thus significantly increase the percolation time. The potential ability of dissolved salts to prevent bubble coalescence has been already studied (Marrucci & Nicodemo, 1967; Zieminski & Whittemore, 1971; Cui et al., 2001). Prevention of bubble coalescence has also been observed with surfactant addition by Qiao & Chandra (1997). They have shown that adding a surfactant to pure water promotes vapor bubble nucleation, causing foaming, while also increasing the contact and heat transfer surface area. Given these considerations, the observed foam formation after spray impact is directly correlated with the prevention of bubble coalescence, suggesting that the physicochemical origin of the foam in the present study can be attributed to the superimposed effects of the salts and surfactants present in the lubricants. The foam formation is shown in Fig. 8.4 and first observed in Section 6.1.

9 Summary and outlook

In the present study, drop and spray impact onto a hot substrate are investigated using industrially relevant multicomponent liquids, *i.e.*, water-based lubricant suspensions and solutions. The phenomena observed in the nucleate boiling, transition boiling, foaming, and film boiling regimes are studied in detail by characterizing the temperature and heat flux evolution in a solid target. The results of the experiments allow a better understanding of the mechanisms involved in the spray impact and the development of theoretical models of the processes involved.

Firstly, the influence of graphite lubricant additives (lubricant suspensions) on the dynamics of a single drop impacting onto a heated substrate is investigated for the nucleate boiling, thermal atomization and film boiling regimes. In the nucleate boiling regime, a reduction and almost complete suppression of drop splash (formation of secondary drops) was observed. The experiments indicate that graphite particles deposit at the interfaces of the expanding bubbles of evaporating liquid, causing a local increase of liquid viscosity and resulting in splash suppression. Reduced splash results in increased residence time of the suspension droplets on the heated substrate. Moreover, a theoretical model for particle deposition and heat transfer in the nucleate boiling regime is developed and experimentally validated. The theoretical predictions for the thickness of the deposited layer agree well with the measurements in the nucleate boiling regime.

At higher temperatures, above the Leidenfrost point, the impact of a pure, one-component liquid can cause drop rebound. However, it has been observed that the presence of the particles in the suspension drop leads to a significant increase of the threshold temperature for drop rebound and the suppression of the splash. Drop impact outcome is also influenced by the deposition of the solid particles during drop spreading. The deposited layer of solid particles causes pinning of both the contact line of the entire drop and the vapor bubbles within the drop. In addition, due to the presence of a particulate

phase, the effective liquid viscosity near free interfaces rises during liquid evaporation, which increases the rebound temperature. The deposited layer also prevents bubble percolation, thereby suppressing thermal drop rebound and film boiling, even at relatively high substrate temperatures where a one-component drop exhibits full rebound. Instead, a thermal atomization regime is observed, even for suspensions with relatively low concentrations of dispersed particulate phase.

Viscosity increase at the evaporation interfaces, local reduction of the surface tension, and pinning of the contact lines on the solid surface lead to the formation of foam-like structures in the drop. Interestingly, the same phenomena, including liquid foaming, were also identified for the lubricant solution drops. This result indicates the significant role of surfactants in foam formation. Furthermore, the crystallization of the solution in the boiling regions leads to the rapid formation of the solid deposited layer, as in the case of suspension drops.

Overall results of the drop impact study can be potentially useful for modeling the formation of the lubricating layer by cooling sprays, which is necessary for predicting the evolution of its thickness and uniformity.

In the spray experiments, the local heat flux and surface temperature were acquired, and visual observations of the hydrodynamics during the spray impact of the lubricant solution (as used in the single drop experiments) were captured by a high-speed observation system. Heat transfer during spray cooling is significantly affected by the presence of dissolved organic salts from the lubricant. It is observed that the presence of very low concentrations of salt-based lubricants dramatically increases the heat flux during spray cooling, especially at high wall temperatures where film boiling is usually observed during spray cooling with distilled water. Three main mechanisms, first identified in the case of single drop impact, that appear to be responsible for the shift of the Leidenfrost point and, in the case of spray impact, could also be the reason for a significant increase of the heat flux: a significant increase in the viscosity of the evaporating lubricant solutions, an increase in the wettability of the substrate as it is coated with the hydrophilic residues of the previous drop impacts of the spray, and the formation of stable liquid sheets between the bubbles, preventing their coalescence and the percolation of the vapor channels. The same mechanism also leads to the formation of

a foam that covers the substrate and provides good wetting even at high temperatures, thus improving spray cooling in terms of shorter cooling times and better cooling performance.

The findings and conclusions from the spray study offer valuable insights for improving cooling and lubrication strategies to meet the die cooling needs in the forging industry. These findings can be adapted to specific cooling applications. The results of this study can be used to derive the minimum duration of the cooling time between two die working cycles for the exact lubricant concentrations used in this study. Additionally, valuable insight is gained regarding the amount of lubricant required to achieve the desired cooling rate under specific operating conditions.

While insights into simultaneous cooling and lubrication have been gained from combined single drop and spray experiments, some mechanisms and observations require further attention in the future. First, the role of additives and salts is manifold and can only be unraveled if their influence on wettability, interface stabilization and viscosity can be studied separately in the future. Also, the mechanisms by which surfactants, salts and solid particles promote foaming on a heated substrate are not entirely clear. Furthermore, the process of foaming that leads to the suppression of film boiling is not yet completely understood. To answer these questions, single drop experiments using simplified "model fluid" systems need to be performed in the future, allowing the effects and contribution of each factor to be observed separately.

Nomenclature

Lowercase Greek Letters

α_i	m^2/s	thermal diffusivity in phase $i \in$ [v, w, l, p]
χ	$-$	empirical coefficient
δ_i	m	thermal boundary layer in phase $i \in$ [v, w, l]
ϵ_0	$-$	relative area of the particle free surface
ϵ_c	$-$	percolation threshold
λ_i	W/mK	thermal conductivity of phase $i \in$ [v, w, l, p]
μ	kg/ms	dynamic viscosity
ν	m^2/s	kinematic viscosity
ω	$-$	dimensionless number
π	$-$	Archimedes constant
ρ_f	kg/m^3	fluid density
ρ_i	kg/m^3	density of phase $i \in$ [v, w, l, p]
σ	N/m	surface tension
θ_c	deg	contact angle
φ	%	volumetric concentration
ϑ	m	ϑ-coordinate
ξ	$-$	dimensionless time

Uppercase Greek Letters

$\Delta T_{\text{rebound}}$	°C	rebound/saturation temperature difference
ΔT_{L}	°C	temperature jump during transition boiling
ΔT_{w}	°C	superheated wall temperature
$\mathcal{T}$	s	predicted parameter

Lowercase Roman Letters

b	–	dimensionless parameter
c_p	J/kgK	specific heat capacity
d_0	m	initial drop diameter
d_{t}	m	spray target diameter
d_{p}	m	particle diameter
e_i	$\text{J/Km}^2\sqrt{\text{s}}$	thermal effusivity of phase $i \in$ [v, w, l, p]
$h(t)$	m	vapor layer thickness
h_{t}	m	spray target height
h_{exp}	m	measured apparent area-averaged layer thickness
h_{lamella}	m	lamella thickness
h_{p}	m	thickness of the particulate layer
h_{res}	m	residual lamella thickness
h_{viscous}	m	viscous boundary layer thickness
k	–	fitting parameter
k_{w}	–	adjustable dimensionless coefficient
k_B	$\text{m}^2\text{kg/s}^2\text{K}$	Boltzmann constant

$\dot{m}$	kg/m^{2}s	local mass flux
$\dot{q}_\mathrm{p}$	W/m^2	local heat flux at the particle layer interface
$\dot{q}$	W/m^2	local heat flux
$\langle\dot{q}\rangle$	W/m^2	time averaged local heat flux
t	s	time
t_L	s	time at Leidenfrost point
$t_\mathrm{percolation}$	s	percolation time
t_c	s	contact time
t_i	s	inital (impact) time
w	–	dimensionless parameter
x	m	axial coordinate
z	m	z-coordinate

Uppercase Roman Letters

$A(\tau)$	°C/s	function
A_c	m^2	contact area
B	–	dimensionless coefficient
B^*	–	incomplete beta function
$\overline{D}_\mathrm{max}$	–	spreading factor
$D_\mathrm{spreading}$	m	spreading diameter
D_max	m	maximum spreading diameter
D_s	m^2/s	diffusion coefficient of the suspension
D_{10}	m	mean drop diameter

G	–	dimensionless coefficient
H	–	dimensionless thickness of the deposited layer
K	–	dimensionless parameter
L	J/kg	latent heat of evaporation
$\dot{M}$	kg/h	mass flow
P	–	dimensionless parameter
Q	J	heat
S	$\mathrm{s}^{1/2}$	parameter
T	°C	interface temperature
T_{d0}	°C	initial drop temperature
T_{f0}	°C	initial fluid temperature
T_{iL}	°C	surface temperature at Leidenfrost point
$T_{\mathrm{Leidenfrost}}$	°C	Leidenfrost temperature
T_{pi}	°C	temperature at solid deposited layer interface
T_{rebound}	°C	rebound temperature
T_{wi}	°C	substrate interface temperature
T_c	°C	contact temperature
T_{sat}	°C	saturation temperature
T_{w0}	°C	initial wall temperature
T_{w}	°C	wall temperature
U	m/s	mean drop velocity
U_0	m/s	initial impact velocity

Dimensionless Numbers

Ca	–	Capillary number
Ja	–	Jakob number
Oh	–	Ohnesorge number
Pe	–	Péclet number
Re	–	Reynolds number
Stk	–	Stokes number
We	–	Weber number

Subscripts

f	fluid
l	liquid
p	solid particles
v	vapor layer
w	solid substrate wall

Bibliography

Abdalrahman, K. H. M., Sabariman, & Specht, E. (2014). Influence of salt mixture on the heat transfer during spray cooling of hot metals. *International Journal of Heat and Mass Transfer*, 78:76–83.

Aboud, D. G. K. & Kietzig, A.-M. (2015). Splashing threshold of oblique droplet impacts on surfaces of various wettability. *Langmuir*, 31 36:10100–11.

Abu-Zaid, M. (2004). An experimental study of the evaporation characteristics of emulsified liquid droplets. *Heat and Mass Transfer*, 40:737–741.

Aksoy, Y. T., Zhu, Y., Eneren, P., Koos, E., & Vetrano, M. R. (2020). The impact of nanofluids on droplet/spray cooling of a heated surface: A critical review. *Energies*, 14(1):80.

Al-Ahmadi, H. & Yao, S. (2008). Spray cooling of high temperature metals using high mass flux industrial nozzles. *Experimental Heat Transfer*, 21:38–54.

Arters, D. C. & Macduff, M. J. (2000). The effect on vehicle performance of injector deposits in a direct injection gasoline engine. *SAE Transactions*, pages 2044–2052.

Aveyard, R. & Clint, J. H. (1995). Liquid droplets and solid particles at surfactant solution interfaces. *Journal of the Chemical Society, Faraday Transactions*, 91(17):2681.

Bakshi, S., Roisman, I. V., & Tropea, C. (2007). Investigations on the impact of a drop onto a small spherical target. *Physics of Fluids*, 19(3):032102.

Bandaru, R., Jha, J., Sarkar, I., Mohapatra, S., Pal, S., & Chakraborty, S. (2013). Achievement of ultrafast cooling rate in a hot steel plate by air-atomized spray with different surfactant additives. *Experimental Thermal and Fluid Science*, 50:79–89.

Barrat, J.-L. & Hansen, J.-P. (2003). *Basic Concepts for Simple and Complex Liquids*. Cambridge University Press, Cambridge, UK.

Batchelor, G. & Green, J. (1972). The determination of the bulk stress in a suspension of spherical particles to order c^2. *Journal of Fluid Mechanics*, 56(3):401–427.

Batzdorf, S., Breitenbach, J., Schlawitschek, C., Roisman, I. V., Tropea, C., Stephan, P., & Gambaryan-Roisman, T. (2017). Heat transfer during simultaneous impact of two drops onto a hot solid substrate. *International Journal of Heat and Mass Transfer*, 113:898–907.

Berberović, E., Roisman, I. V., Jakirlić, S., & Tropea, C. (2011). Inertia dominated flow and heat transfer in liquid drop spreading on a hot substrate. *International Journal of Heat and Fluid Flow*, 32(4):785–795.

Bernardin, J., Stebbins, C., & Mudawar, I. (1997). Mapping of impact and heat transfer regimes of water drops impinging on a polished surface. *International Journal of Heat and Mass Transfer*, 40:247–267.

Berryman, J. G. (1983). Random close packing of hard spheres and disks. *Physical Review A*, 27(2):1053.

Blanken, N., Saleem, M. S., Thoraval, M.-J., & Antonini, C. (2021). Impact of compound drops: a perspective. *Current Opinion in Colloid & Interface Science*, 51:101389.

Breitenbach, J. (2019). *Drop and spray impact onto a hot substrate: Dynamics and heat transfer*. PhD thesis, Technische Universität Darmstadt, Darmstadt, Germany.

Breitenbach, J., Roisman, I. V., & Tropea, C. (2017a). Drop collision with a hot, dry solid substrate: Heat transfer during nucleate boiling. *Physical Review Fluids*, 2:074301.

Breitenbach, J., Roisman, I. V., & Tropea, C. (2017b). Heat transfer in the film boiling regime: Single drop impact and spray cooling. *International Journal of Heat and Mass Transfer*, 110:34–42.

Breitenbach, J., Roisman, I. V., & Tropea, C. (2018). From drop impact physics to spray cooling models: a critical review. *Experiments in Fluids*, 59:1–21.

Buchmüller, I. (2014). *Influence of pressure on Leidenfrost effect*. PhD thesis, Technische Universität Darmstadt, Darmstadt, Germany.

Burzynski, D. A., Roisman, I. V., & Bansmer, S. E. (2020). On the splashing of high-speed drops impacting a dry surface. *Journal of Fluid Mechanics*, 892:A2.

Butt, H.-J., Roisman, I. V., Brinkmann, M., Papadopoulos, P., Vollmer, D., & Semprebon, C. (2014). Characterization of super liquid-repellent surfaces. *Current Opinion in Colloid & Interface Science*, 19(4):343–354.

Cai, Z., Wang, B., Liu, S., Li, H., Luo, S., Dong, Z., & Wang, Y. (2022). Enhancing boiling heat transfer on a superheated surface by surfactant-laden droplets. *Langmuir*, 38(34):10375–10384.

Carey, V. P. (2020). *Liquid-vapor phase-change phenomena: an introduction to the thermophysics of vaporization and condensation processes in heat transfer equipment*. CRC Press, Boca Raton, USA.

Castanet, G., Chaze, W., Caballina, O., Collignon, R., & Lemoine, F. (2018). Transient evolution of the heat transfer and the vapor film thickness at the drop impact in the regime of film boiling. *Physics of Fluids*, 30(12):122109.

Chakraborty, S., Sarkar, I., Roshan, A., Pal, S., & Chakraborty, S. (2019). Spray cooling of hot steel plate using aqueous solution of surfactant and polymer. *Thermal Science and Engineering Progress*, 10.

Chandra, S. & Avedisian, C. T. (1991). On the collision of a droplet with a solid surface. *Proceedings of the Royal Society of London. Series A, Mathematical and Physical Sciences*, 432:13 – 41.

Chantelot, P. & Lohse, D. (2021). Leidenfrost effect as a directed percolation phase transition. *Physical Review Letters*, 127:124502.

Chen, H., Ruan, X.-h., Peng, Y.-h., Wang, Y.-l., & Yu, C.-k. (2022a). Application status and prospect of spray cooling in electronics and energy

conversion industries. *Sustainable Energy Technologies and Assessments*, 52:102181.

Chen, L.-J., Hsu, M.-C., Lin, S.-T., & Yang, S.-Y. (1995). Salt effect on wetting/nonwetting behaviors. *The Journal of Physical Chemistry*, 99(13):4687–4697.

Chen, M., Chen, D., Liu, Y., Liu, H., & Liu, H. (2022b). Experimental study on the secondary droplet formation mechanism when droplet impacting on superheated surface. *International Journal of Heat and Mass Transfer*, 185:122412.

Chen, S.-J. & Tseng, A. A. (1992). Spray and jet cooling in steel rolling. *International Journal of Heat and Fluid Flow*, 13(4):358–369.

Cheng, L. (1977). Dynamic spreading of drops impacting onto a solid surface. *Industrial & Engineering Chemistry Process Design and Development*, 16:192–197.

Cheng, W., Xie, B., Han, F., & Chen, H. (2013). An experimental investigation of heat transfer enhancement by addition of high-alcohol surfactant (HAS) and dissolving salt additive (DSA) in spray cooling. *Experimental Thermal and Fluid Science*, 45:198–202.

Cheng, W.-L., Zhang, W.-W., Chen, H., & Hu, L. (2016). Spray cooling and flash evaporation cooling: The current development and application. *Renewable and Sustainable Energy Reviews*, 55:614–628.

Clanet, C., Béguin, C., Richard, D., & Quéré, D. (2004). Maximal deformation of an impacting drop. *Journal of Fluid Mechanics*, 517:199–208.

Coelho, D., Thovert, J.-F., & Adler, P. M. (1997). Geometrical and transport properties of random packings of spheres and aspherical particles. *Physical Review E*, 55(2):1959.

Collings, E. W., Markworth, A. J., McCoy, J. K., & Saunders, J. H. (1990). Splat-quench solidification of freely falling liquid-metal drops by impact on a planar substrate. *Journal of Materials Science*, 25(8):3677–3682.

Cossali, G., Santini, M., & Marengo, M. (2005). Single-drop empirical models for spray impact on solid walls: A review. *Atomization and Sprays*, 15:699–736.

Cui, Q., Chandra, S., & McCahan, S. (2001). The effect of dissolving gases or solids in water droplets boiling on a hot surface. *Journal of Heat Transfer*, 123(4):719–728.

Cui, Q., Chandra, S., & McCahan, S. (2003). The effect of dissolving salts in water sprays used for quenching a hot surface: Part 2—Spray cooling. *Journal of Heat Transfer*, 125(2):333–338.

Dawi, A. H., Herbert, S., Roisman, I. V., Gambaryan-Roisman, T., Stephan, P., & Tropea, C. (2013). Numerical investigation of drop impact onto hot surfaces. In *Proceedings of 25th European Conference on Liquid Atomization and Spray Systems (ILASS)*, Chania, Crete, Greece.

Deegan, R. D., Bakajin, O., Dupont, T. F., Huber, G., Nagel, S. R., & Witten, T. A. (1997). Capillary flow as the cause of ring stains from dried liquid drops. *Nature*, 389(6653):827–829.

Denkov, N. D., Velev, O. D., Kralchevsky, P., Ivanov, I., Yoshimura, H., & Nagayama, K. (1993). Two-dimensional crystallization. *Nature*, 361(6407):26–26.

Duursma, G., Sefiane, K., & Kennedy, A. (2009). Experimental studies of nanofluid droplets in spray cooling. *Heat Transfer Engineering*, 30(13):1108–1120.

Eggers, J., Fontelos, M. A., Josserand, C., & Zaleski, S. (2010). Drop dynamics after impact on a solid wall: theory and simulations. *Physics of Fluids*, 22(6):062101.

Einstein, A. (1906). Eine neue Bestimmung der Moleküldimensionen. *Annalen der Physik*, 19:230–247.

Einstein, A. (1908). Elementare Theorie der Brownschen Bewegung. *Zeitschrift für Elektrochemie und angewandte physikalische Chemie*, 14(17):235–239.

Emerson, P., Crockett, J., & Maynes, D. (2021). Thermal atomization during droplet impingement on superhydrophobic surfaces: Influence of Weber number and micropost array configuration. *International Journal of Heat and Mass Transfer*, 164:120559.

Eral, H. B., Augustine, D. M., Duits, M. H., & Mugele, F. (2011). Suppressing the coffee stain effect: how to control colloidal self-assembly in evaporating drops using electrowetting. *Soft Matter*, 7(10):4954–4958.

Esmaili, E., Chen, Z.-Y., Pandey, A., Kim, S., Lee, S., & Jung, S. (2021). Corona splashing triggered by a loose monolayer of particles. *Applied Physics Letters*, 119:174103.

Frye, G. C. & Berg, J. C. (1989). Antifoam action by solid particles. *Journal of Colloid and Interface Science*, 127(1):222–238.

Fu, N., Woo, M. W., & Chen, X. D. (2012). Single droplet drying technique to study drying kinetics measurement and particle functionality: A review. *Drying Technology*, 30(15):1771–1785.

Gajevic Joksimovic, M., Hussong, J., Tropea, C., & Roisman, I. V. (2023a). Spray impact onto a hot solid substrate: Film boiling suppression by lubricant addition. *Frontiers in Physics*, 11:1172584.

Gajevic Joksimovic, M., Roisman, I. V., Tropea, C., & Hussong, J. (2023b). Influence of industrial lubricant addition on cooling regimes during single drop impact. In *Proceedings of the 17th International Heat Transfer Conference (IHTC-17)*, Cape Town, South Africa.

Gajevic Joksimovic, M., Schmidt, J. B., Roisman, I. V., Tropea, C., & Hussong, J. (2023c). Impact of a suspension drop onto a hot substrate: diminution of splash and prevention of film boiling. *Soft Matter*, 19:1440–1453.

Garrett, P. R. (2016). *The Science of Defoaming: Theory, Experiment and Applications*. CRC Press, Boca Raton, USA.

Goodwin, J. W. & Reynolds, P. A. (1998). The rheology of flocculated suspensions. *Current Opinion in Colloid & Interface Science*, 3(4):401–407.

Gradeck, M., Ouattara, A., Maillet, D., Gardin, P., & Lebouché, M. (2011). Heat transfer associated to a hot surface quenched by a jet of oil-in-water emulsion. *Experimental Thermal and Fluid Science*, 35(5):841–847.

Hsieh, S. S., Hsu, Y.-F., & Wang, M. (2014). A microspray-based cooling system for high powered leds. *Energy Conversion and Management*, 78:338–346.

Huang, C.-K. & Carey, V. (2007). The effects of dissolved salt on the Leidenfrost transition. *International Journal of Heat and Mass Transfer*, 50:269–282.

Itaru, M. & Kunihide, M. (1978). Heat transfer characteristics of evaporation of a liquid droplet on heated surfaces. *International Journal of Heat and Mass Transfer*, 21(5):605–613.

Josserand, C. & Thoroddsen, S. (2016). Drop impact on a solid surface. *Annual Review of Fluid Mechanics*, 48(1):365–391.

Karwa, N. (2012). *Experimental Study of Water Jet Impingement Cooling of Hot Steel Plates*. PhD thesis, Technische Universität Darmstadt, Darmstadt.

Kestin, J., Khalifa, H. E., & Correia, R. J. (1981). Tables of the dynamic and kinematic viscosity of aqueous NaCl solutions in the temperature range 20–150 °C and the pressure range 0.1–35 MPa. *Journal of Physical and Chemical Reference Data*, 10(1):71–88.

Kholodenko, A. L. & Douglas, J. F. (1995). Generalized Stokes-Einstein equation for spherical particle suspensions. *Physical Review E*, 51(2):1081.

Kim, H., Truong, B., Buongiorno, J., & Hu, L.-W. (2012). Effects of micro/nano-scale surface characteristics on the leidenfrost point temperature of water. *Journal of Thermal Science and Technology*, 7:453–462.

Kim, J. (2007). Spray cooling heat transfer: The state of the art. *International Journal of Heat and Fluid Flow*, 28(4):753–767.

Kirkwood, J. G. (1935). Statistical mechanics of fluid mixtures. *The Journal of Chemical Physics*, 3(5):300–313.

Kirkwood, J. G. (1936). Statistical mechanics of liquid solutions. *Chemical Reviews*, 19(3):275–307.

Kittel, H. M., Roisman, I. V., & Tropea, C. (2018). Splash of a drop impacting onto a solid substrate wetted by a thin film of another liquid. *Physical Review Fluids*, 3(7):073601.

Kruse, C., Anderson, T., Wilson, C., Zuhlke, C., Alexander, D., Gogos, G., & Ndao, S. (2013). Extraordinary shifts of the Leidenfrost temperature from multiscale micro/nanostructured surfaces. *Langmuir*, 29.

Kumar, V., Sinha, K. N. R., & Raj, R. (2020). Leidenfrost phenomenon during quenching in aqueous solutions: effect of evaporation-induced concentration gradients. *Soft Matter*, 16:6145–6154.

Lagubeau, G., Fontelos, M., Josserand, C., Maurel, A., Pagneux, V., & Petitjeans, P. (2012). Spreading dynamics of drop impacts. *Journal of Fluid Mechanics*, 713:50–60.

Lahane, S. & Subramanian, K. (2014). Impact of nozzle holes configuration on fuel spray, wall impingement and NOX emission of a diesel engine for biodiesel–diesel blend (B20). *Applied Thermal Engineering*, 64(1-2):307–314.

Leidenfrost, J. G. (1966). On the fixation of water in diverse fire. *International Journal of Heat and Mass Transfer*, 9(11):1153–1166.

Lhuissier, H. & Villermaux, E. (2012). Bursting bubble aerosols. *Journal of Fluid Mechanics*, 696:5–44.

Liang, G. & Mudawar, I. (2017a). Review of spray cooling – part 1: Single-phase and nucleate boiling regimes, and critical heat flux. *International Journal of Heat and Mass Transfer*, 115:1174–1205.

Liang, G. & Mudawar, I. (2017b). Review of spray cooling – part 2: High temperature boiling regimes and quenching applications. *International Journal of Heat and Mass Transfer*, 115:1206–1222.

Liu, P., Kandasamy, R., Ho, J. Y., Feng, H., & Wong, T. N. (2021). Comparative study on the enhancement of spray cooling heat transfer using conventional and bio-surfactants. *Applied Thermal Engineering*, 194:117047.

Lubritech, F. (2022a). Lubrodal F105. https://www.fuchs.com/lubritech/en/product/product/118075-lubrodal-f-105/.

Lubritech, F. (2022b). Lubrodal F327. https://www.fuchs.com/lubritech/en/product/product/144158-lubrodal-f-327/.

Lyu, S., Tan, H., Wakata, Y., Yang, X., Law, C. K., Lohse, D., & Sun, C. (2021). On explosive boiling of a multicomponent Leidenfrost drop. *Proceedings of the National Academy of Sciences*, 118(2):e2016107118.

Maenosono, S., Dushkin, C., Saita, S., & Yamaguchi, Y. (1999). Growth of a semiconductor nanoparticle ring during the drying of a suspension droplet. *Langmuir*, 15(4):957–965.

Mandre, S. & Brenner, M. P. (2012). The mechanism of a splash on a dry solid surface. *Journal of Fluid Mechanics*, 690:148–172.

Marengo, M., Antonini, C., Roisman, I. V., & Tropea, C. (2011). Drop collisions with simple and complex surfaces. *Current Opinion in Colloid & Interface Science*, 16:292–302.

Marin, A. G., Gelderblom, H., Lohse, D., & Snoeijer, J. H. (2011). Order-to-disorder transition in ring-shaped colloidal stains. *Physical Review Letters*, 107(8):085502.

Marmanis, H. & Thoroddsen, S. T. (1996). Scaling of the fingering pattern of an impacting drop. *Physics of Fluids*, 8(6):1344–1346.

Marrucci, G. & Nicodemo, L. (1967). Coalescence of gas bubbles in aqueous solutions of inorganic electrolytes. *Chemical Engineering Science*, 22(9):1257–1265.

Meingast, U., Staudt, M., Reichelt, L., Renz, U., & Sommerhoff, F.-A. (2000). Analysis of spray/wall interaction under diesel engine conditions. *SAE Transactions*, pages 299–312.

Mewis, J. (1996). Flow behaviour of concentrated suspensions: predictions and measurements. *International Journal of Mineral Processing*, 44-45:17–27.

Mezhericher, M., Levy, A., & Borde, I. (2010). Theoretical models of single droplet drying kinetics: a review. *Drying Technology*, 28(2):278–293.

Mills, P. (1985). Non-Newtonian behaviour of flocculated suspensions. *Journal de Physique Lettres*, 46(7):301–309.

Mohapatra, S. S., Ravikumar, S. V., Jha, J. M., Singh, A. K., Bhattacharya, C., Pal, S. K., & Chakraborty, S. (2014). Ultra fast cooling of hot steel plate by air atomized spray with salt solution. *Heat and Mass Transfer*, 50(5):587–601.

Moita, A. & Moreira, A. (2011). Scaling the effects of surface topography in the secondary atomization resulting from droplet/wall interactions. *Experiments in Fluids*, 52:679–695.

Mondal, R., Lama, H., & Sahu, K. C. (2023). Physics of drying complex fluid drop: Flow field, pattern formation, and desiccation cracks. *Physics of Fluids*, 35(6).

Monde, M., Arima, H., Liu, W., Mitutake, Y., & Hammad, J. (2003). An analytical solution for two-dimensional inverse heat conduction problems using Laplace transform. *International Journal of Heat and Mass Transfer*, 46:2135–2148.

Moreira, A., Moita, A., & Panão, M. (2010). Advances and challenges in explaining fuel spray impingement: How much of single droplet impact research is useful? *Progress in Energy and Combustion Science*, 36(5):554–580.

Ness, C., Seto, R., & Mari, R. (2022). The physics of dense suspensions. *Annual Review of Condensed Matter Physics*, 13(1):97–117.

Nukiyama, S. (1966). The maximum and minimum values of the heat Q transmitted from metal to boiling water under atmospheric pressure. *International Journal of Heat and Mass Transfer*, 9(12):1419–1433.

Opfer, L., Roisman, I. V., Venzmer, J., Klostermann, M., & Tropea, C. (2014). Droplet-air collision dynamics: Evolution of the film thickness. *Physical Review E*, 89(1):013023.

Otsu, N. (1979). A threshold selection method from gray-level histograms. *IEEE Transactions on Systems, Man, and Cybernetics*, 9(1):62–66.

Özisik, M. N. (1980). *Heat conduction*. Wiley, New Jersey, USA.

Pack, M. Y., Hu, H. W., Kim, D. I., Zheng, Z., Stone, H. A., & Sun, Y. (2017). Failure mechanisms of air entrainment in drop impact on lubricated surfaces. *Soft Matter*, 13 12:2402–2409.

Palacios, J., Hernández, J., Gómez, P., Zanzi, C., & López, J. (2013). Experimental study of splashing patterns and the splashing/deposition threshold in drop impacts onto dry smooth solid surfaces. *Experimental Thermal and Fluid Science*, 44:571–582.

Panão, M. R. & Moreira, A. L. (2009). Intermittent spray cooling: a new technology for controlling surface temperature. *International Journal of Heat and Fluid Flow*, 30(1):117–130.

Panão, M. O., Moita, A. S., & Moreira, A. L. (2020). On the statistical characterization of sprays. *Applied Sciences*, 10(17).

Pati, A., Mandal, S., Dash, A., Barik, K., Munshi, B., & Mohapatra, S. (2018). Oil-in-water emulsion spray: A novel methodology for the enhancement of heat transfer rate in film boiling regime. *International Communications in Heat and Mass Transfer*, 98:96–105.

Pati, A. R., Behera, A., Munshi, B., & Mohapatra, S. S. (2017). Enhancement of heat removal rate of high mass flux spray cooling by sea water. *Experimental Thermal and Fluid Science*, 89:19–40.

Pavlov, T., Vlahovic, L., Staicu, D., Konings, R., Wenman, M., Van Uffelen, P., & Grimes, R. (2017). A new numerical method and modified apparatus for the simultaneous evaluation of thermo-physical properties above 1500 K: A case study on isostatically pressed graphite. *Thermochimica Acta*, 652:39–52.

Piskunov, M., Breitenbach, J., Schmidt, J., Strizhak, P., Tropea, C., & Roisman, I. (2021). Secondary atomization of water-in-oil emulsion drops impinging on a heated surface in the film boiling regime. *International Journal of Heat and Mass Transfer*, 165:120672.

Qiao, Y. M. & Chandra, S. (1997). Experiments on adding a surfactant to water drops boiling on a hot surface. *Proceedings of the Royal Society of London. Series A, Mathematical, Physical and Engineering Sciences*, 453:673 – 689.

Qiao, Y. M. & Chandra, S. (1998). Spray cooling enhancement by addition of a surfactant. *Journal of Heat Transfer*, 120(1):92–98.

Rahman, M. M. & Asiri, A. M. (2016). *Advances in Colloid Science*. InteChOpen, Rijeka.

Ravikumar, S. V., Jha, J. M., Sarkar, I., Pal, S. K., & Chakraborty, S. (2014a). Enhancement of heat transfer rate in air-atomized spray cooling of a hot steel plate by using an aqueous solution of non-ionic surfactant and ethanol. *Applied Thermal Engineering*, 64(1-2):64–75.

Ravikumar, S. V., Jha, J. M., Tiara, A., Pal, S. K., & Chakraborty, S. (2014b). Experimental investigation of air-atomized spray with aqueous polymer additive for high heat flux applications. *International Journal of Heat and Mass Transfer*, 72:362–377.

Rein, M. H. (2002). *Drop-Surface Interactions*, volume 456 of *CISM Courses and Lectures*. Springer Wien New York, Vienna, Austria.

Riboux, G. & Gordillo, J. M. (2014). Experiments of drops impacting a smooth solid surface: A model of the critical impact speed for drop splashing. *Physical Review Letters*, 113:024507.

Riboux, G. & Gordillo, J. M. (2015). The diameters and velocities of the droplets ejected after splashing. *Journal of Fluid Mechanics*, 772:630–648.

Rioboo, R., Marengo, M., & Tropea, C. (2001). Outcomes from a drop impact on solid surfaces. *Atomization and Sprays*, 11:155–166.

Rioboo, R., Voué, M., Vaillant, A., & De Coninck, J. (2008). Drop impact on porous superhydrophobic polymer surfaces. *Langmuir*, 24(24):14074–14077.

Roisman, I. (2010a). Fast forced liquid film spreading on a substrate: Flow, heat transfer and phase transition. *Journal of Fluid Mechanics*, 656:189–204.

Roisman, I. V. (2009). Inertia dominated drop collisions. II. An analytical solution of the Navier–Stokes equations for a spreading viscous film. *Physics of Fluids*, 21(5):052104.

Roisman, I. V. (2010b). Fast forced liquid film spreading on a substrate: flow, heat transfer and phase transition. *Journal of Fluid Mechanics*, 656:189–204.

Roisman, I. V., Berberović, E., & Tropea, C. (2009). Inertia dominated drop collisions. I. On the universal flow in the lamella. *Physics of Fluids*, 21(5):052103.

Roisman, I. V., Breitenbach, J., & Tropea, C. (2018). Thermal atomisation of a liquid drop after impact onto a hot substrate. *Journal of Fluid Mechanics*, 842:87–101.

Roisman, I. V., Horvat, K., & Tropea, C. (2006). Spray impact: Rim transverse instability initiating fingering and splash, and description of a secondary spray. *Physics of Fluids*, 18(10):102104.

Roisman, I. V., Lembach, A., & Tropea, C. (2015). Drop splashing induced by target roughness and porosity: The size plays no role. *Advances in Colloid and Interface Science*, 222:615–621. Reinhard Miller, Honorary Issue.

Roisman, I. V., Rioboo, R., & Tropea, C. (2002). Normal impact of a liquid drop on a dry surface: model for spreading and receding. *Proceedings of the Royal Society of London. Series A, Mathematical, Physical and Engineering Sciences*, 458(2022):1411–1430.

Rybicki, J. & Mudawar, I. (2006). Single-phase and two-phase cooling characteristics of upward-facing and downward-facing sprays. *International Journal of Heat and Mass Transfer*, 49:5–16.

Sanches, M., Marseglia, G., Ribeiro, A. P., Moreira, A. L., & Moita, A. S. (2021). Nanofluids characterization for spray cooling applications. *Symmetry*, 13(5):788.

Sarkar, I., Behera, D. K., Jha, J. M., Pal, S. K., & Chakraborty, S. (2016). Effect of polymer additive on the cooling rate of a hot steel plate by using water jet. *Experimental Thermal and Fluid Science*, 70:105–114.

Scheller, B. L. & Bousfield, D. W. (1995). Newtonian drop impact with a solid surface. *Aiche Journal*, 41:1357–1367.

Schmidt, A., Bonarens, M., Roisman, I. V., Nishad, K., Sadiki, A., Dreizler, A., Hussong, J., & Wagner, S. (2021a). Experimental investigation of AdBlue film formation in a generic SCR test bench and numerical analysis using LES. *Applied Sciences*, 11(15):6907.

Schmidt, J., Tenzer, F., Tropea, C., Hussong, J., & Roisman, I. (2023). Modelling of drop and spray impact in the transitional boiling regime. *International Journal of Heat and Mass Transfer*, 217:124586.

Schmidt, J. B., Hofmann, J., Tenzer, F. M., Breitenbach, J., Tropea, C., & Roisman, I. V. (2021b). Thermosuperrepellency of a hot substrate caused by vapour percolation. *Communications Physics*, 4(1):1–8.

Schremb, M., Borchert, S., Berberovic, E., Jakirlic, S., Roisman, I. V., & Tropea, C. (2017). Computational modelling of flow and conjugate heat transfer of a drop impacting onto a cold wall. *International Journal of Heat and Mass Transfer*, 109:971–980.

Schremb, M., Roisman, I. V., & Tropea, C. (2018). Normal impact of supercooled water drops onto a smooth ice surface: experiments and modelling. *Journal of Fluid Mechanics*, 835:1087–1107.

Scott, G. D. & Kilgour, D. M. (1969). The density of random close packing of spheres. *Journal of Physics D: Applied Physics*, 2(6):863.

Sienski, K., Eden, R., & Schaefer, D. (1996). 3-D electronic interconnect packaging. In *1996 IEEE Aerospace Applications Conference. Proceedings*, volume 1, pages 363–373, Aspen, CO, USA.

Sijia, L., Mathai, V., Wang, Y., Sobac, B., Colinet, P., Lohse, D., & Sun, C. (2019). Final fate of a Leidenfrost droplet: Explosion or takeoff. *Science Advances*, 5:eaav8081.

Singh, S. & Kukreja, R. (2021). Experimental study on effects of surfactant and spray inclination on heat transfer performance in nonboiling regime. *Energy Sources, Part A: Recovery, Utilization, and Environmental Effects*, pages 1–15.

Sodtke, C. & Stephan, P. (2007). Spray cooling on micro structured surfaces. *International Journal of Heat and Mass Transfer*, 50(19-20):4089–4097.

Stumpf, B., Hussong, J., & Roisman, I. V. (2022). Drop impact onto a substrate wetted by another liquid: Flow in the wall film. *Colloids and Interfaces*, 6(4).

Takata, Y., Hidaka, S., Cao, J., Nakamura, T., Yamamoto, H., Masuda, M., & Ito, T. (2005). Effect of surface wettability on boiling and evaporation. *Energy*, 30(2):209–220.

Tartarini, P., Lorenzini, G., & Randi, M. (1999). Experimental study of water droplet boiling on hot, non-porous surfaces. *Heat and Mass Transfer*, 34(6):437–447.

Taylor, G. I. (1959). The dynamics of thin sheets of fluid II. waves on fluid sheets. *Proceedings of the Royal Society of London. Series A. Mathematical and Physical Sciences*, 253(1274):296–312.

Tenzer, F., Roisman, I. V., & Tropea, C. (2019). Fast transient spray cooling of a hot thick target. *Journal of Fluid Mechanics*, 881:84–103.

Tenzer, F. M. (2020). *Heat transfer during transient spray cooling: An experimental and analytical study.* Phd thesis, Technische Universität Darmstadt, Darmstadt, Germany.

Thayyil Raju, L., Diddens, C., Li, Y., Marin, A., van der Linden, M. N., Zhang, X., & Lohse, D. (2022). Evaporation of a sessile colloidal water–glycerol droplet: Marangoni ring formation. *Langmuir*, 38(39):12082–12094. PMID: 36094143.

Thoraval, M.-J., Schubert, J., Karpitschka, S., Chanana, M., Boyer, F., Sandoval-Naval, E., Dijksman, J., Snoeijer, J., & Lohse, D. (2021). Nanoscopic interactions of colloidal particles can suppress millimetre drop splashing. *Soft Matter*, 17.

Tran, T., Staat, H. J., Prosperetti, A., Sun, C., & Lohse, D. (2012). Drop impact on superheated surfaces. *Physical Review Letters*, 108(3):036101.

Tropea, C. (2011). Optical particle characterization in flows. *Annual Review of Fluid Mechanics*, 43:399–426.

Tropea, C. & Roisman, I. (2000). Modeling of spray impact on solid surfaces. *Atomization and Sprays*, 10:387–408.

Trueman, R., Lago Domingues, E., Emmett, S., Murray, M., & Routh, A. (2012a). Auto-stratification in drying colloidal dispersions: A diffusive model. *Journal of Colloid and Interface Science*, 377(1):207–212.

Trueman, R. E., Lago Domingues, E., Emmett, S. N., Murray, M. W., Keddie, J. L., & Routh, A. F. (2012b). Autostratification in drying colloidal dispersions: Experimental investigations. *Langmuir*, 28(7):3420–3428.

V V S Vara Prasad, G., Dhar, P., & Samanta, D. (2022). Postponement of dynamic Leidenfrost phenomenon during droplet impact of surfactant solutions. *International Journal of Heat and Mass Transfer*, 189:1–12.

Vallejo, J. P., Gómez-Barreiro, S., Cabaleiro, D., Gracia-Fernández, C., Fernández-Seara, J., & Lugo, L. (2018). Flow behaviour of suspensions of functionalized graphene nanoplatelets in propylene glycol–water mixtures. *International Communications in Heat and Mass Transfer*, 91:150–157.

Weickgenannt, C. M., Zhang, Y., Sinha-Ray, S., Roisman, I. V., Gambaryan-Roisman, T., Tropea, C., & Yarin, A. L. (2011). Inverse-Leidenfrost phenomenon on nanofiber mats on hot surfaces. *Physical Review E*, 84(3):036310.

Wendelstorf, J., Spitzer, K.-H., & Wendelstorf, R. (2008). Spray water cooling heat transfer at high temperatures and liquid mass fluxes. *International Journal of Heat and Mass Transfer*, 51(19):4902–4910.

Wildeman, S., Visser, C. W., Sun, C., & Lohse, D. (2016). On the spreading of impacting drops. *Journal of Fluid Mechanics*, 805:636–655.

Woodfield, P., Monde, M., & Mitsutake, Y. (2006). Improved analytical solution for inverse heat conduction problems on thermally thick and semi-infinite solids. *International Journal of Heat and Mass Transfer*, 49:2864–2876.

Worthington, A. M. & Clifton, R. B. (1877). XXVIII. On the forms assumed by drops of liquids falling vertically on a horizontal plate. *Proceedings of the Royal Society of London*, 25(171-178):261–272.

Worthington, A. M. & Cole, R. S. (1897). V. Impact with a liquid surface, studied by the aid of instantaneous photography. *Philosophical Transactions of the Royal Society of London. Series A, Containing Papers of a Mathematical or Physical Character*, 189:137–148.

Xu, L., Zhang, W. W., & Nagel, S. R. (2005). Drop splashing on a dry smooth surface. *Physical Review Letters*, 94:184505.

Xu, R., Wang, G., & Jiang, P. (2022). Spray cooling on enhanced surfaces: A review of the progress and mechanisms. *Journal of Electronic Packaging*, 144(1).

Yao, S. C. & Cox, T. L. (2002). A general heat transfer correlation for impacting water sprays on high-temperature surfaces. *Experimental Heat Transfer*, 15(4):207–219.

Yarin, A., Brenn, G., Kastner, O., & Tropea, C. (2002). Drying of acoustically levitated droplets of liquid–solid suspensions: Evaporation and crust formation. *Physics of Fluids*, 14(7):2289–2298.

Yarin, A. L. (2005). Drop impact dynamics: Splashing, spreading, receding, bouncing…. *Annual Review of Fluid Mechanics*, 38:159–192.

Yarin, A. L., Roisman, I. V., & Tropea, C. (2017). *Collision Phenomena in Liquids and Solids*. Cambridge University Press, Cambridge, UK.

Yarin, A. L. & Weiss, D. A. (1995). Impact of drops on solid surfaces: self-similar capillary waves, and splashing as a new type of kinematic discontinuity. *Journal of Fluid Mechanics*, 283:141–173.

Yunker, P. J., Still, T., Lohr, M. A., & Yodh, A. (2011). Suppression of the coffee-ring effect by shape-dependent capillary interactions. *Nature*, 476(7360):308–311.

Zhang, W.-W., Li, Y.-Y., Long, W.-J., & Cheng, W.-L. (2018). Enhancement mechanism of high alcohol surfactant on spray cooling: Experimental study. *International Journal of Heat and Mass Transfer*, 126:363–376.

Zhang, Y., Jia, M., Liu, H., & Xie, M. (2016). Development of an improved liquid film model for spray/wall interaction under engine-relevant conditions. *International Journal of Multiphase Flow*, 79:74–87.

Zhang, Z., Li, J., & Jiang, P.-X. (2013). Experimental investigation of spray cooling on flat and enhanced surfaces. *Applied Thermal Engineering*, 51(1-2):102–111.

Zieminski, S. A. & Whittemore, R. C. (1971). Behavior of gas bubbles in aqueous electrolyte solutions. *Chemical Engineering Science*, 26(4):509–520.

List of Figures